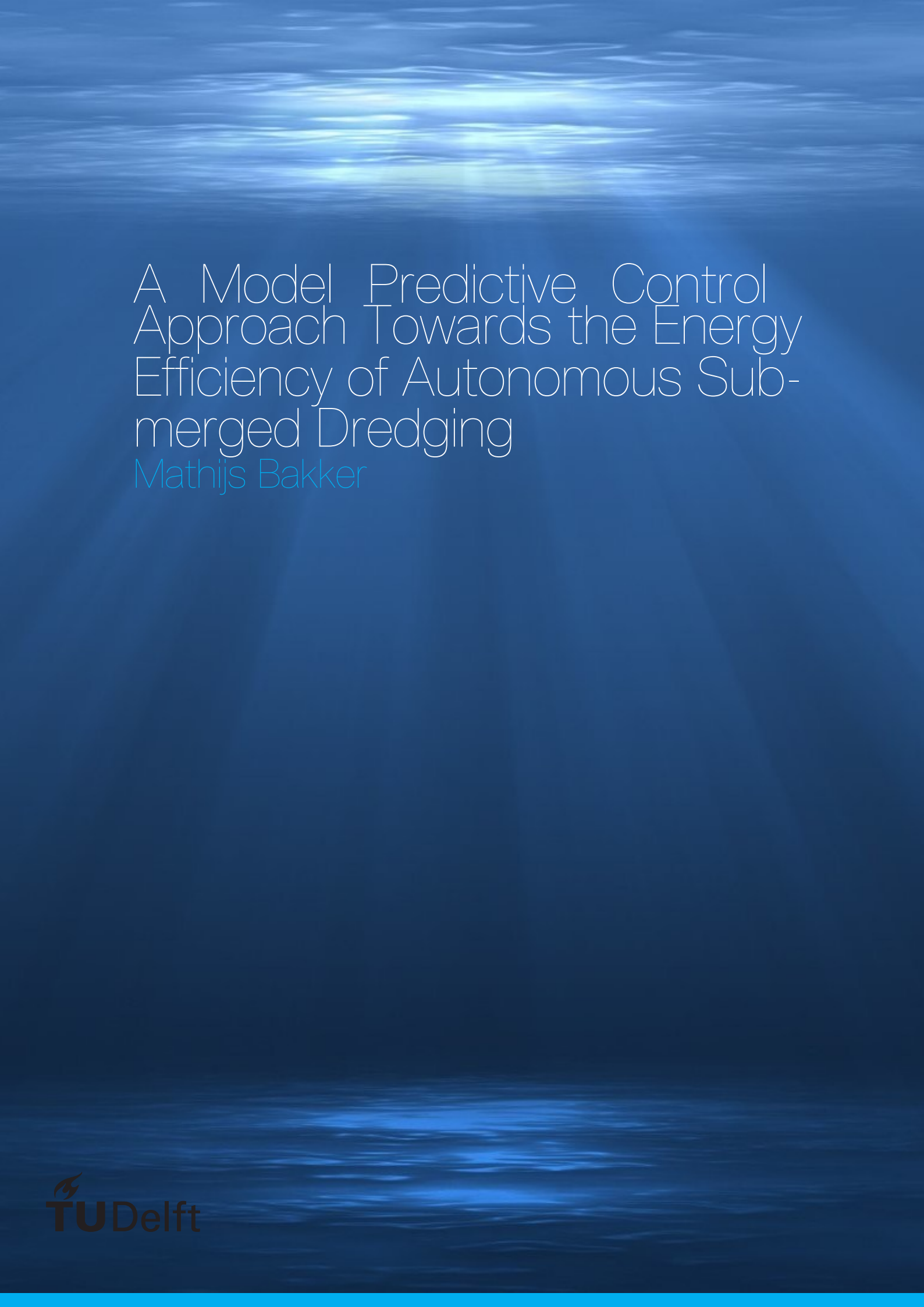

A Model Predictive Control Approach Towards the Energy Efficiency of Autonomous Submerged Dredging

Mathijs Bakker

TU Delft

A Model Predictive Control Approach Towards the Energy Efficiency of Autonomous Submerged Dredging

by

Mathijs Bakker

Performed at

C-Job Naval Architects

to obtain the degree of Master of Science in Marine Technology
in the specialization of Marine Engineering
at the Delft University of Technology,
to be defended publicly on Thursday, August 11, 2022, at 09:00.

Student number: 4601297
Thesis number: MT.21/22.043.M
Project duration: October 13, 2021 – August 11, 2022

Thesis committee:			
	Ir. K. Visser,	TU Delft,	Chair
	Dr. A. Coraddu,	TU Delft,	Daily supervisor
	Ing. R. Hijdra,	C-Job,	Daily supervisor

This thesis is confidential and cannot be made public until August 11, 2024.

An electronic version of this thesis is available at http://repository.tudelft.nl/.

TU Delft

C-JOB DEDICATED NAVAL ARCHITECTS

Preface

Dear reader,

This report is the result of 9 months of work on the Autonomous Low Energy Replenishment Dredger (ALERD) as part of the master thesis for the master Marine Technology.

I would like to thank Rolph Hijdra, the founder of ALERD, and who gave me the opportunity to work on my thesis at C-Job Naval Architects. Since the beginning, I was very enthusiastic and curious about the ALERD and its potential. This work hopefully contributes to a future-proof and sustainable solution for dredging. Our weekly meetings and discussions were always very helpful, and your enthusiasm about the ALERD project, the outcomes and potential of my simulation model, and in general about autonomous shipping worked very motivating.

Next, I like to thank Andrea Coraddu, for your time and our weekly meetings, and for your enthusiasm and support since the beginning of this master thesis. Your insights and contributions to this research were really helpful.

I would also like to thank my colleagues at C-Job who supported me during my graduation, and Vittorio Garofano for his time and insights in Model Predictive Control.

Finally, I would like to thank my friends and family for their support for the last six years.

Mathijs Bakker
August, 2022
Delft

Abstract

As part of the ”Innovations in the Coastline Care” program of the Dutch Rijkswaterstaat, and taking into account the need to decrease emissions, C-Job Naval Architects has developed the Autonomous Low Energy Replenishment Dredger (ALERD). The ALERD is an autonomous underwater vehicle, that will be used for submerged dredging, and is developed as a cost-effective solution for performing coastal replenishment along the Dutch coastline. It will have a large hopper inside the hull, in which the dredged soil can be stored, transported, and eventually be discharged close to the shore. Submerged dredging comes with all kinds of new challenges, for instance stability and buoyancy control during the submerged dredging operations. In this research, a time-domain simulation model is developed, able of controlling a mathematically modelled underwater vehicle in 6 degrees of freedom (DoF).

Due to the current phase of the ALERD concept, no detailed information of the hydrodynamic characteristics is available. It is seen as unfavorable to carry out CFD-simulations or scale-model tests, since both are seen as expensive and time-consuming methods, and the main parameters of the ALERD are not final yet. Therefore, it is chosen to parametrically model the ALERD using mathematical expressions for the hydrodynamic coefficients used in the equations of motion. The equations of motion in six DoF are rewritten in a state-space representation, to perform time-domain simulations with.

The ALERD has a unique operational profile, since it will be submerged during the three operational modes, which are transit, dredging and discharging. An operational profile is defined for the ALERD, based on conventional dredgers doing coastal replenishment along the Dutch coastline. Each operational mode has its own characteristics, such as depth, speed, and duration. It is chosen to control the depth, forward speed, and pitch angle of the ALERD, using motion controllers. Controlling the depth and pitch angle contribute to the total energy requirements for stability and buoyancy control, while speed control is added to create a realistic time-domain simulation. Proportional-derivative-integral (PID) control is used to create a benchmark, and the more advanced control method Model Predictive Control (MPC) is used to improve the outcomes of the simulations. A Model Predictive Control approach is used to minimize the control effort, which is directly coupled with the energy requirements. The main disturbances during the dredging and discharging operations are added, which are the trimming moment produced by the draghead during the dredging operation, and the change of mass in the hopper during dredging and discharging.

The contributors to the energy requirements for stability and buoyancy control are the main ballast tank, the depth control tank, and the trim tank system. These systems are used in combination with the motion controllers to provide the required restoring forces and moments. The main ballast tank is used to compensate for the change of weight in the hopper, the depth control tank is used in combination with the motion controllers to control the depth and to track the desired depth reference, and the trim tank system is used to control the pitch angle and track the desired pitch reference. It is shown that using MPC for controlling the depth and pitch angle, results in the best reference tracking while minimizing the required energy.

A sensitivity analysis is done, using a Monte Carlo Simulation, to assess the effect of modelling uncertainties on the outcome of the simulations, and to assess the performance of the controllers. Six coefficients are chosen, on which uncertainty is applied, since there is uncertainty in the calculated values for the used added mass and linear damping coefficients in the equations of motion. It is shown that MPC is capable of dealing with modelling uncertainties, while minimizing the energy requirements and ensure sufficient trajectory tracking of both the depth and pitch angle reference.

One of the outcomes of the research is that the required energy for stability and buoyancy control has a contribution of 16% on the total amount of required energy. Using this result, submerged dredging results in an energy saving of more than 66% compared to conventional dredging, for the specific operational profile defined in this research.

The end product of this research is a time-domain simulation model, in which MPC is used to control an underwater vehicle that is parametrically modelled. MPC ensures the control effort, which is directly coupled to the energy requirements, is minimized. Minimizing the energy requirements is necessary

for the ALERD to make it a cost-effective solution. The controllers are designed in such a way that they show sufficient performance in tracking the reference trajectories for the depth and pitch angle, taking into account physical constraints and modelling uncertainties.

Contents

Nomenclature

Abbreviations

CB	Center of Buoyancy
CG	Center of Gravity
CO	Center of Origin
RB	Rigid Body
ALERD	Autonomous Low Energy Replenishment Dredger
AUMD	Autonomous Underwater Maintenance Dredger
AUV	Autonomous Underwater Vehicle
CAPEX	Capital Expenses
CFD	Computational Fluid Dynamics
DCT	Depth Control Tank
DoF	Degree of Freedom
HRC	Hydrographic Research Center
HRC-AUV	Light Autonomous Underwater Vehicle
IKZ	Innovaties in de Kustlijnzorg
IMO	International Maritime Organization
KPI	Key Performance Indicator
LSW	Light Ship Weight
LTI	Linear Time-Invariant
MBT	Main Ballast Tank
MD	Measured Disturbance
MO	Measured Output
MPC	Model Predictive Control
MV	Manipulated Variable
OPEX	Operational Expenses
PID	Proportional-Integral-Derivative control
QP	Quadratic Program
TSHD	Trailing Suction Hopper Dredger
TT	Trim Tank

Greek symbols

ρ_ε	Dimensionless constraint violation penalty weight
α_0, β_0	Factors describing a prolate ellipsoid [-]
β_c	Current direction [rad]
δb	Deflection angle bow plane [rad]
δr	Deflection angle rudder [rad]
δs	Deflection angle stern plane [rad]
Δ	Displacement [ton]
η_{pump}	Pump Efficiency [-]
λ	Length ratio [-]
$_{DCT}$	Mass in DCT [kg]
$\boldsymbol{\eta}$	Position vector
$\boldsymbol{\omega}$	Angular velocity vector
$\boldsymbol{\tau_{crossflow}}$	Vector with cross-flow drag
$\boldsymbol{\tau_{R_T}}$	Vector with total ship resistance
$\boldsymbol{\tau}$	Hydrodynamic forces and moments vector
$\boldsymbol{\Theta}$	Vector with Euler angles ϕ, θ, ψ
μ	Mean of a normal distribution
∇	Displaced volume [m^3]
ν	Kinematic viscosity [m^2/s]
ϕ	Roll angle [rad]

ψ	Yaw/heading angle [rad]
ρ	Fluid density [kg/m^3]
σ	Standard deviation of a normal distribution
θ	Pitch angle [rad]
ε	Slack variable used in MPC cost function
ξ	Slack variable used in MPC cost function
ζ	System resistance factor [-]
$m_{TT,fore}$	Mass change in forward TT [kg]

Roman symbols

$\bar{d}$	Equivalent diameter prolate ellipsoid [m]
$\bar{x_n}$	Sample mean
Δu	Change in manipulated variable
$\dot{V}$	Volume flow rate [m^3/s]
$\boldsymbol{C_A}$	Added mass coriolis-centripetal matrix
$\boldsymbol{C}$	Coriolis-centripetal matrix
$\boldsymbol{D}$	Damping matrix
$\boldsymbol{f}$	Force vector
$\boldsymbol{g}_0$	Pretrimming (ballast control) vector
$\boldsymbol{G}$	Matrix with restoring forces and moments
$\boldsymbol{g}$	Restoring forces and moments vector
$\boldsymbol{H}$	Transformation matrix
$\boldsymbol{I}$	Identity matrix
$\boldsymbol{J}$	Euler transformation matrix
$\boldsymbol{M_A}$	Added Mass Matrix
$\boldsymbol{M}$	Inertia and added mass matrix
$\boldsymbol{m}$	Moment vector
$\boldsymbol{P}$	Transformation matrix using vessel parallel coordinates
$\boldsymbol{R}$	Euler transformation matrix for linear velocity and positions
$\boldsymbol{r}$	Position vector
$\boldsymbol{r}$	Vector with reference signal
$\boldsymbol{S}$	Cross-product operator
$\boldsymbol{T}$	Euler transformation matrix for angular velocity
$\boldsymbol{u}$	Input vector with manipulated variables used for MPC
$\boldsymbol{v_c}$	Current velocity vector
$\boldsymbol{v_r}$	Relative velocity vector
$\boldsymbol{v}$	Velocity vector
$\boldsymbol{W}$	Matrix with tuning weights
$\boldsymbol{x}$	State vector
$\boldsymbol{y}$	Output vector with manipulated outputs used for MPC
A	Area of control surface [m^2]
a	Half the length of an ellipsoid [m]
B	Buoyancy [N]
B	Width [m]
b	Radius of an ellipsoid [m]
c	Radius of an ellipsoid [m]
C_T	Thrust Coefficient [-]
C_D	Drag coefficient [-]
C_{F0}	ITTC'57 Skin friction coefficient [-]
C_L	Lift coefficient [-]
D	Draught [m]
d_{pipe}	Pipe diameter [m]
D_{prop}	Propeller diameter [m]
D_{sp}	Drag force stern plane [N]
e	Length-diameter ratio ellipsoid [-]
$e(t)$	PID time-varying error signal
F_n	Froude Number [-]

g	gravitational acceleration [m/s^2]
I	Moment of Inertia [kgm^2]
i	Numbering of prediction horizon step
J	Cost function for MPC
j	Numbering of MV, MO, change in MV, and MD
k	Form factor [-]
K, M, N	Moments about the x-axis, y-axis and z-axis respectively [Nm]
k_1, k_2, k'	Lamb's k-factors [-]
K_d	PID derivative gain
K_i	PID integral gain
K_p	PID proportional gain
K_T	Thrust coefficient [-]
L	Length [m]
L_{sp}	Lift force stern plane [N]
m	Control horizon [s]
m	Mass [kg]
n	Propeller speed [rps]
n	Sample size
P	Power [W]
p	Prediction horizon [s]
p	Pressure [Pa]
p, q, r	Angular velocities about the x-axis, y-axis and z-axis respectively [rad/s]
Q	Propeller torque [Nm]
R_e	Reynolds Number [-]
R_T	Total ship resistance [N]
r_{44}	Roll damping factor [-]
S	Hull wetted surface [m^2]
s	Scaling factor, used in the cost function for MPC
s_n	Sample standard deviation
T	Propeller thrust [N]
t	Time [s]
T_s	Controller sampling time [s]
$t_{n-1,\alpha/2}$	Student's t-distribution parameter
u	Manipulated variable (MV)
u, v, w	Velocities in the x, y and z directions respectively [m/s]
v	Fluid velocity [m/s]
V_c	Current speed [m/s]
V_s	Ship speed [m/s]
W	Weight [N]
w	Weight factor, used in the cost function for MPC
X	Random variable
x, y, z	Positions in the x-axis, y-axis and z-axis respectively [m]
X, Y, Z	Forces in the x-axis, y-axis and z-axis respectively [N]
y	Manipulated output (MO)
z_k	Decision of the QP solver for MPC
$K_{\dot{p}}$	Added Mass in yaw direction
K_p	Linear damping in yaw direction
$M_{\dot{q}}$	Added Mass in pitch direction
M_q	Linear damping in pitch direction
$N_{\dot{r}}$	Added Mass in roll direction
N_r	Linear damping in roll direction
$X_{\dot{u}}$	Added Mass in surge direction
X_u	Linear damping in surge direction
$Y_{\dot{v}}$	Added Mass in sway direction
Y_v	Linear damping in sway direction
$Z_{\dot{w}}$	Added Mass in heave direction

Z_w	Linear damping in heave direction

Superscripts and Subscripts

Δu	Change in manipulated variable MV
b	Body-fixed frame
b	Center of Buoyancy
g	Center of Gravity
i	Inertial frame
i	Numbering of prediction horizon step
j	Numbering of MV, MO, change in MV, and MD
k	Control interval MPC controller [s]
n	NED frame
u	Manipulated variable MV
y	Measured output MO
T	Calculation of the transpose

List of Figures

List of Tables

1

Introduction

1.1. Project Background

Each year, the maintenance works along the Dutch coastline requires on average 12 million cubic meters of sand. These maintenance works are carried out using trailing suction hopper dredgers (TSHDs), which emit greenhouse gasses during dredging operations. The Dutch Rijkswaterstaat has the ambition to decrease these emissions to zero at the latest by 2030. To achieve this ambition, Rijkswaterstaat started the innovations in the coastline care (”Innovaties in de Kustlijnzorg, (IKZ)”) program. The aim of this program is to develop a sustainable, zero emission and cost-effective concept that can be used for maintenance work along the Dutch coastline [14]. As part of this program, C-Job Naval Architects (C-Job) is developing the Autonomous Low Energy Replenishment Dredger (ALERD). The ALERD is the successor of the autonomous underwater maintenance dredger (AUMD) which is a concept design developed by C-Job to show the potential benefits of using an autonomous underwater dredger compared to a conventional TSHD.

1.1.1. Autonomous Underwater Maintenance Dredger

The AUMD is a preliminary concept design developed by C-Job to show the advantages and disadvantages of using an autonomous underwater vehicle for maintenance works in the port of Rotterdam and Eemshaven compared to the reference trailing suction hopper dredger (TSHD) ”Rijndelta”. This research showed that due to the reduced wave making and wave breaking resistance, the installed power for propulsion can be reduced by 55%. Since the AUMD will operate near the seabed, the installed pump power can be reduced by 80% due to the reduced suction depth. Furthermore, due to the submerged dredging operation, the operability is improved. The reduced installed power for propulsion and pumps in combination with using electrical power results in a cost-effective and sustainable solution for maintenance work in Dutch ports [8]. A visualization of the AUMD concept can be found in Figure 1.1.

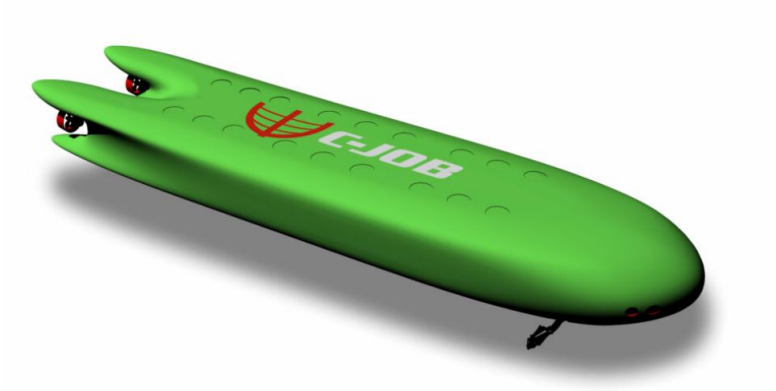

Figure 1.1: Preliminary concept design of the AUMD [8]

1.1.2. Autonomous Low Energy Replenishment Dredger

The ALERD is developed by C-Job as the successor of the AUMD and the main difference is the operational profile of the ALERD compared to the AUMD. Since the ALERD is part of the IKZ program, it will be designed for coastal replenishment instead of maintenance work in ports. The final main dimensions of the ALERD are unknown at this point, and therefore the dimensions of the AUMD serve as a starting point.

Since the main goal of the ALERD is coastal replenishment, it will have a large hopper in the hull. The AUMD (and thus the ALERD as well) is designed in such a way that the hopper will always be filled, either with seawater or with a soil mixture of water and sand. Discharging of the soil will take place using the bottom door openings in the hull. Water can enter the hopper using the upper or lower flooding holes in the hull. These holes can also be seen in the visualization of the AUMD concept in Figure 1.1.

1.2. Problem Definition

The ALERD concept is the first autonomous submarine that will be used for dredging purposes. Underwater dredging comes with all kinds of new unknown challenges compared to traditional dredging. This research focuses specifically on the energy requirements of the ALERD for stability and buoyancy control. C-Job is interested in the required energy since it is one of the most important aspects of the ALERD which will be fully electric, and it can demonstrate whether underwater dredging is advantageous compared to conventional dredging seen from an energetic point of view.

To be able to estimate the energy requirement for stability and buoyancy control, the primary aim of this research is to develop a simulation model for the ALERD for a complete operational cycle. This specific energy requirement can be compared to a conventional TSHD in order to show the potential benefits and cost-effectiveness of dredging underwater autonomously. Since the final main dimensions are unknown, C-Job has the wish to estimate the energy requirement for different dimensions of the ALERD.

Due to the current phase of the ALERD concept, expensive and time-consuming methods such as model tests or CFD-analysis are unfavorable, also taking into account the fact that there is no final hull form available. Therefore, a model must be developed that is able to do time-domain simulations while controlling the motions using motion control methods, in which the ALERD is parametrically described, enabling the user to change the main parameters and compare different designs. The simulation model should not only be able to simulate and control the ALERD in the time domain, it should also be able to optimize the energy consumption required for one operational cycle. To our best knowledge, such a model does not exist yet, also taking into account the unique operational profile and dredging operations of the ALERD. Therefore, research must be done on which motion control method is able of controlling the ALERD, while minimizing the control effort and thus the required energy for motion control.

1.3. Research Aim and Objectives

1.3.1. Research Aim

"The development of a time-domain simulation model, in which the hydrodynamics of an autonomous submerged dredger are modelled, and which is able to perform trajectory-tracking using a motion controller, while optimizing the required energy consumption for motion control".

In order to achieve the research aim, multiple research objectives and research questions are defined in the next section.

1.3.2. Research Questions

In order to gather the relevant knowledge, needed for achieving the research objective, a literature review is done prior to the development of the simulation model, described in this report. The objectives of this literature review are listed below, and the outcomes of the literature review are used as a starting point to develop the simulation model.

Research Objectives Literature Review

1. Find in the literature modelling approaches that can simulate underwater vehicles numerically.

2. Find in the literature the state-of-the-art motion control methods that can be used to control a simulation model of an underwater vehicle.
3. Find in the literature the state-of-the-art stabilizing systems for underwater vehicles.
   (a) Determine how can they be implemented in the simulation model.
   (b) Estimate their energy requirements for the different stabilizing systems.
4. Determine the destabilizing influences on underwater vehicles based on the expected operational profile of the ALERD.
   (a) Determine the destabilizing influences on conventional dredging vessels.
   (b) Determine the destabilizing influences on underwater vehicles.

Research Questions and Sub-Questions
The following research questions are answered throughout this report and are required to reach the research aim defined above.

1. How can the hydrodynamics of underwater vehicles such as the ALERD be mathematically modelled and implemented in a time-domain simulation model?
2. What is the operational profile of one complete dredging cycle of the ALERD?
   (a) What are the time-varying disturbances acting on the ALERD during the operational cycle?
   (b) Which DoFs of the ALERD contribute to the energy requirement for buoyancy and stability control?
3. Which motion control method is the best suitable for trajectory-tracking and controlling the different DoFs of the ALERD?
   (a) Which motion control method gives the most energy efficient outcome when performing trajectory-tracking?
   (b) Which motion control method is most suitable for taking into account physical constraints?
4. How can the physical systems, needed for stability and buoyancy control, be implemented in the simulation model and used to calculate the energy requirements?
5. How does uncertainty in the modelling of underwater vehicles such as the ALERD affect the performance of the motion controllers and therefore the outcome of the simulation model?
   (a) What are physical KPIs and controller KPIs in the simulation model?
   (b) How does uncertainty in the modelling approach affect the KPIs?
6. Using the outcomes of the time-domain simulations, what is the contribution of the energy requirements for stability and buoyancy control to the complete energy consumption for submerged dredging?

1.4. Research Relevance

In this section, the relevance of this research based on ethical and societal aspects will be given. The abbreviation ALERD contains the words autonomous, low-energy and replenishment dredger, which all have societal and ethical aspects and which will be covered here. This section will provide some ethical and societal aspects of the complete ALERD concept.

1.4.1. Protection of the Dutch Coast

Each year the Dutch coast needs to be maintained to protect the mainland from flooding and this becomes more and more important, looking at the effect of climate change and the rise of the sea level. The sea bottom, beaches, and dunes along the coast that are needed to protect the mainland suffer from erosion due to storms, waves, wind and current and each year new sand is needed to recover that. The Dutch Rijkswaterstaat, responsible (amongst others) for coastal maintenance, has defined the Basic coastline (BCL) which is a measure to determine the coastal decline and erosion. When it is expected the BCL will be exceeded, sand replenishment is necessary. The two most important replenishment methods applied along the Dutch are coastal replenishment and beach replenishment, where extra sand is added either on the sea bottom near the coast or directly on the beach. Figure 1.2 shows three conventional TSHDs doing coastal replenishment off the coast of Texel [29], using the rainbow technique. According to Rijkswaterstaat, on average 12 million cubic meters of sand is necessary each year to protect the Dutch coast, which is achieved by using dredgers [14]. Dredgers are necessary to maintain the coast and protect the mainland, and it is expected that this need is only growing in the near future. Therefore, it is also necessary to come up with new and innovative dredging concepts such as the ALERD that can maintain and protect the coast in a more sustainable and cost-effective way.

Figure 1.2: Coastal replenishment with three THSDs rainbowing [29]

1.4.2. Sustainable Dredging

There is a growing need for coastal maintenance, and at the same time there is the worldwide need to reduce emissions such as carbon dioxide and nitrogen dioxide. Rijkswaterstaat has the ambition to reduce the greenhouse gas emissions due to coastal maintenance to zero at the latest by 2030, as described in the innovations in the coastline care program. This ambition, in combination with recent worldwide climate agreements and the increasing rules and regulations regarding pollutant emissions, stresses the need for new, innovative, sustainable and cost-effective solutions for dredging such as the ALERD.

Figure 1.3: Natura 2000 areas in the Netherlands [1]

One example is shown in Figure 1.3, which shows the Natura 2000 areas in the Netherlands, indicated in green, yellow and blue. Natura 2000 areas are protected nature areas, and they cover a significant part of the Netherlands, including areas where dredging activities for coastal maintenance and sand replenishment take place, such as the Wadden area and other parts of the Dutch coast. In these areas additional rules and regulations apply and special permits are necessary for activities emitting nitrogen, such as dredging, and therefore new concepts such as the ALERD are a good solution for dredging in nature protected areas. The ALERD will be fully electric and therefore emission-free while operating.

As already mentioned in the problem description, the most important aspect of the ALERD is autonomous underwater dredging. It is demonstrated that underwater dredging reduces the power consumption for propulsion and pumps significantly due to the decrease of wave making- and braking resistance and the reduced suction depth [8]. This power reduction, in combination with the use of electric power onboard for propulsion and pumps, can lead to a sustainable solution for coastal maintenance, contributing to the goal of Rijkswaterstaat. However, it is up to this point unknown what the additional energy requirements for stability and buoyancy control of underwater dredging are compared to conventional dredging at the water surface. Therefore, it is important to quantify this specific energy requirement to show potential advantages or disadvantages of underwater dredging.

1.4.3. Environmental Values

In [10] multiple advantages of the ALERD regarding nature and environment are mentioned, which are called the environmental values.

One of the advantages of underwater dredging is the invisibility of the vessel for recreational beach users. There is no visual amenity and noise disturbance caused by TSHDs operating close to the beach, and therefore dredging operations can be performed all year round, even in the holiday season. There are no pollutant emissions and visual black smoke since the ALERD will be fully electric and submerged during dredging operations.

The lack of conventional (diesel-) engines and emissions contribute to more quietness in the coastal area, which is beneficial for both recreational users and the nature in these vulnerable and protected nature areas. Furthermore, because of the reduction in required propulsion and pump power and the absence of (diesel-) engines and gearboxes, the underwater noise reduces, which is beneficial for the underwater life. The increased hydrostatic pressure due to the submerged depth reduces the change of cavitation occurring at the propeller or in the pumps, which is normally seen as a significant source

of noise production.

Due to operating close to the seabed, the dredged material can be placed more precisely on the designated areas using bottom door openings [11]. Due to the shorter distance to the bottom, there is less dredge plume, which is seen as beneficial for the underwater environment. Another advantage of using bottom door openings is the low energy consumption compared to rainbowing (see Figure 1.2), which is seen as an energy intensive process.

1.4.4. Cost-Effective Solution

In addition to sustainability, another main driver of the ALERD and also an important goal of the IKZ program is the cost-effectiveness of the concept. Sustainable solutions such as emission-free ships using electrical power often come with a high cost-price, since those innovative techniques are still under development and therefore more expensive. The expected reduction of required power for propulsion and pumps reduces the number of batteries or fuel cells needed for the supply of electrical power onboard the ALERD. This will reduce the cost price and increase the cost-effectiveness. The absence of accommodation for the crew is another cost saving feature of the ALERD. However, it is expected that certain aspects such as the hull are more expensive compared to conventional dredgers. Other estimated initial and operational costs are in detailed described in [10] and [11] and won't be given here. For the predecessor of the ALERD, the AUMD, it is estimated that the initial capital expenses (CAPEX) are higher compared to conventional dredger and the operational expenses (OPEX) are lower, in the end resulting in a cost-effective solution for coastal replenishment.

1.4.5. Impact of Autonomous Shipping

In [9] a study is presented looking at 6091 major accidents for all classes of commercial ships, and it is concluded that in 62% human errors caused the accidents. However, it is also important to mention that incidents today are averted by the crew of ships and that it will be very hard to show that increased automation can match this number. In Figure 1.4 a schematic overview of remaining incidents with autonomous ships is drawn and [9] bases its findings on reports of accidents and averted incidents. The reduction of incidents due to automation is indicated with the white areas and the net result of incidents still occurring in autonomous ships is indicated with the gray areas. It is concluded that it is generally accepted that automation of human processes onboard of ships has the potential to decrease accidents, however this assumption remains to be shown and automation has the potential of creating accidents itself due to, for instance, the implementation of new technologies.

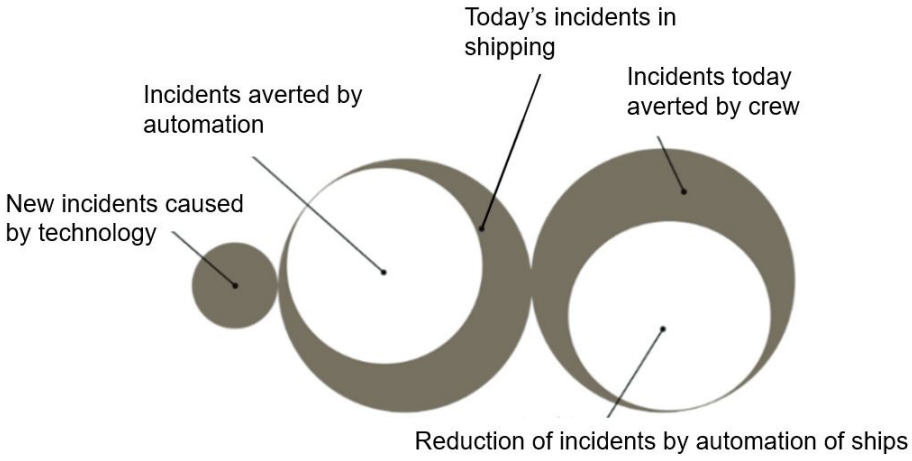

Figure 1.4: Schematic overview of remaining incidents with autonomous ships [9]

According to [30] unmanned or low-manned ships will reduce the number of people at risk at sea. Increased safety is considered one of the primary perceived drivers for autonomous shipping and in [30] the first statistic analysis is performed to determine the distribution of human casualties and lost ships over accident types, ship types, and ship sizes. It is shown that 44% of all accidents are navigation related, but it is uncertain what percentage of these accidents might be prevented due to autonomous

navigation. When looking at the entire worldwide fleet, [30] concludes that the removal of the crew from all ships comes down to a reduction of 174 lives lost per year. An important note is that the fleet of dredgers is only a small percentage of the entire fleet, and that most incidents and lives lost are on small cargo ships ($L < 120m$). However, it is expected that removing the crew from ships will always lead to more safety for crew and ships. In [30] the same conclusion is drawn as in [9], which is the fact that autonomous shipping reduces the number of incidents, ship losses and lives lost, but the percentage is uncertain and that it is important to put more effort in research that enables safe elimination of the crew's role in all functions of the ship.

In [20] the limitations of autonomous ships compared to manned ships are described accordingly, and the role of humans in autonomous systems is described. It is stated that humans can employ creative and adaptive solution-orientated thinking and decision-making in abnormal situations necessary to avert incidents, where autonomous systems may be deficient. It mentions that the occurrence of navigational accidents is expected to decrease for autonomous ships, however, the rate of non-navigational accidents could increase due to the complexity of the new technology on autonomous ships, analogous to the conclusions in [9] and also shown in Figure 1.4.

The potential effects of autonomous technologies on the future work organization and roles of humans within maritime operations is explored based on interviews with subject-matter experts working within the industry and academia in [20]. These experts say that with the shift to autonomous operations, the roles and skills of future marine operators may shift from traditional seafarers to non-seafarers with a different background. The role of operators will most likely shift from operating onboard ships to a more supervisory role on land, which reorganizes humans within the system. It is therefore too easy to say that removing people from ships eliminates the human errors causing accidents, since the design and development of autonomous ships is implemented and controlled by humans, just like traditional shipping performed today. Future marine operators may never go to sea, but still need basic knowledge and experience of seafaring to interact with and interpret operations of the autonomous ship. Other potential relevant skills are related to programming, information technology, analytics and serious gaming skills, according to the interviewed experts in [20]. [20] highlights the importance of developing new education and training programs based on new and evolving skills required for the "seafarers" of the future. New training and education programs need to be developed to match learning objectives with the new and emerging operational demands created by unmanned and autonomous maritime systems, as concluded in [20].

It is however expected that the shift from offshore to onshore operations is accompanied with resistance of seafarers. Since the scope of work of onshore operations is significantly different compared to the work onboard of ships, the willingness of seafarers to retrain themselves might be low. An important aspect is the thrust and acceptance of new technologies such as autonomous ships in the society.

In general, it can be concluded that autonomous shipping will change the role of traditional seafarers and that it will lead to a reduction of crew sizes and in the end to completely unmanned ships. In [30], the authors considered this as one of the benefits of autonomous shipping, since it is expected that in the coming years a shortage in manning will occur. According to [30] it is predicted that by 2025 an additional, 147500 officers are needed. Reducing the crew size can counteract the predicted shortage of seafarers.

[25] offers a review and analytical discussion on the upcoming changes in maritime transport, focusing on the role of the human operator, distribution of responsibilities between human and machine, maritime career issues and new challenges for maritime education and training institutions. In this research, it is mentioned that the most important issue of changing the shipping world to autonomous shipping is the acceptance of the society, for which it is necessary to overcome legal and emotional barriers [25]. Legal barriers are mentioned in [20] where it is stated that regulatory bodies such as the International Maritime Organization (IMO) and insurers are struggling to keep the pace led by technologists to shift to autonomous sailing.

1.5. Report Outline

In Chapter 2, the hydrodynamic modelling of the ALERD and implementation of the mathematical equations into Matlab and Simulink will be discussed. The methodology, used to define an underwater vehicle in 6 DoF, using mathematical formulations, is described here. Furthermore, it is explained how the mathematical model is implemented in Matlab and Simulink, in order to do time-domain simulations for

a given time period.

In Chapter 3, a description is given of the different motion control methods that are used in the simulation model, which are PID control and MPC. The operational profile of the ALERD is defined in this chapter, as well as the time-varying disturbances due to the dredging operations. The actuators are defined, used by the motion controllers to create the required restoring forces and moments.

In Chapter 4, the modelling and mathematical derivation of the physical systems used as actuators by the motion controllers for stability and buoyancy control will be given. The physical systems are modelled in Simulink and linked with the output of the motion controllers, in order to assess the corresponding energy requirements.

In Chapter 5, a sanity check is done to validate the developed simulation model, by assessing the outcomes of the simulations and by checking the internal relationships within the model.

In Chapter 6, the results from the simulations, using the different motion controllers, are discussed. A comparison is made between the results from the PID and MPC controllers, based on the controller performance and the outcomes of the energy calculations.

In Chapter 7, a sensitivity analysis is done. Monte Carlo Simulations are done to investigate the effect of modelling uncertainties on the outcomes of the simulations. The controller performance is assessed taking into account the uncertainties, and confidence intervals are constructed for the outcomes of the simulation model.

2

Methodology

In this chapter, the methodology, used to mathematically model underwater vehicles such as the ALERD, is described. This modelling approach is required to be able to simulate the motions of the ALERD, in a time-domain simulation model, in six degrees of freedom (DoF). This approach is particularly useful at the current design stage of the ALERD, in which the final main dimensions and hull form are unknown. Parametric modelling of underwater vehicles using mathematical expressions in a time-domain simulation model allows changing the main parameters such as the length or displacement, which makes it possible to compare different designs with each other.

2.1. ALERD Concept

In this section, a description of the Autonomous Low Energy Replenishment Dredger (ALERD) concept will be given. As mentioned in Chapter 1, the ALERD will be an autonomous underwater vehicle used for dredging. The ALERD is the successor of the Autonomous Underwater Maintenance Dredger (AUMD).

2.1.1. Hull Form and Hopper

In Figure 2.1, the hull and the layout inside the hull of the ALERD can be seen. The hull form is similar as depicted in Figure 1.1 from Chapter 1, and is determined in previous studies [8]. The hull form from Figure 1.1 and 2.1 is the hull from the AUMD, which was developed for maintenance work in harbors. Due to the current stage of the ALERD concept, this hull form will also be used as the basis for the ALERD in this research. The hull form and the main dimensions of the hull from the ALERD still need to be optimized, which will be done in future research, since the ALERD has a different application compared to the AUMD. The ALERD will be used for coastal replenishment, and uses two dragheads to excavate the soil from the bottom. The propulsion of the ALERD will be done using two azimuthing thrusters. In [17], the systems required for delivering the energy are determined. In this study, it is shown that using batteries is the most cost-effective solution to provide the required energy onboard the ALERD.

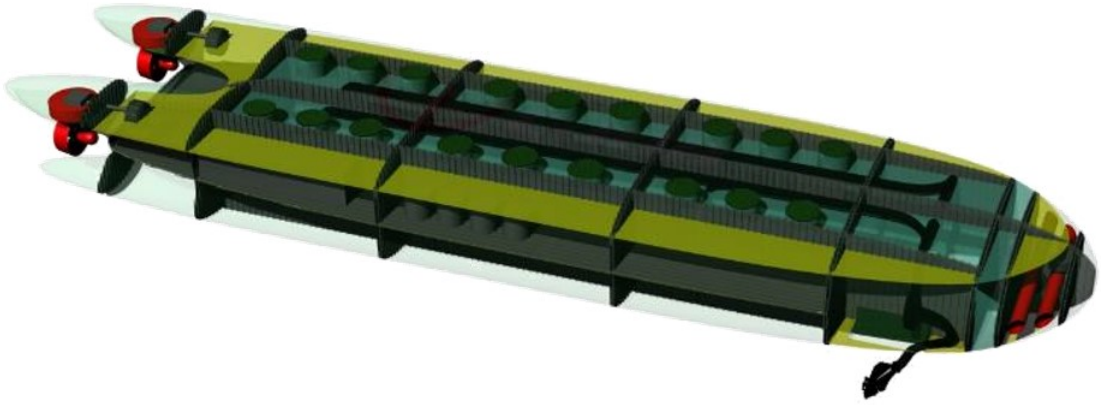

Figure 2.1: Hull form of the ALERD

In Figure 2.2, the cross-section of the hull is shown. The hopper, used to store the dredged soil, is located inside the hull of the ALERD. The hopper itself can be found in Figure 2.3. In Figure 2.3, the flooding holes and the bottom door openings can be seen, which are located at the top and the bottom of the hopper, respectively. For the ALERD, it is chosen to have the hopper always filled, with either seawater or a mixture of seawater and the dredged soil. If the ALERD is dredging, the dredged material will be pumped inside the hopper using the dredging pumps. The upper flooding holes can be used to get rid of the excess of water. The bottom door openings can be used to discharge the dredged soil.

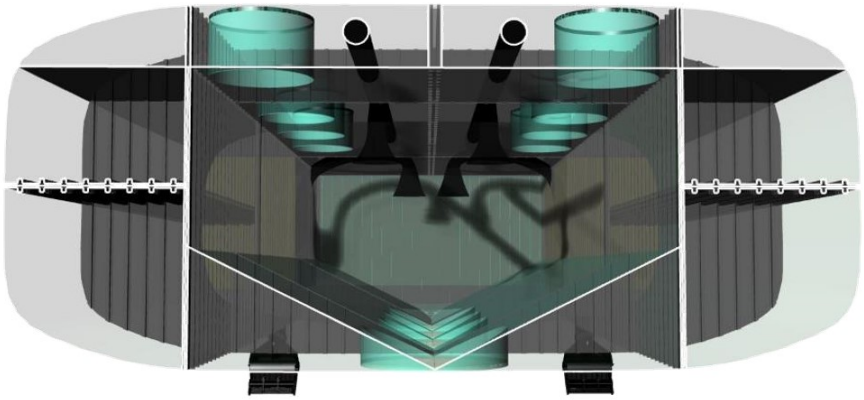

Figure 2.2: Cross-section of the hull with hopper

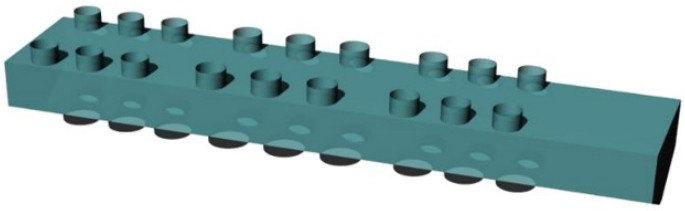

Figure 2.3: Hopper

2.1.2. Main Dimensions

The initial main dimensions of the ALERD, used in this research, can be found in Table 2.1 and are based on a previous study, performed in [10]. The dimensions, displacement, and hopper volume are corresponding to the hull form of the AUMD shown in Figure 2.1. These dimensions will be used throughout this report, and in the simulation model, when performing time-domain simulations.

The results from the simulations, in terms of energy requirements for stability and buoyancy control, will be compared with the energy requirements from the conventional dredger. To make a fair comparison, a conventional TSHD performing coastal replenishment along the Dutch coastline is chosen, with a similar operational profile and similar hopper volume. Based on that comparison, it can be shown whether underwater dredging is advantageous compared to conventional dredging at the water surface, looking at the energy requirements for stability and buoyancy control. This comparison is described in more detail in Chapter 6.

The capacity of the hopper is determined based on the main dimensions of the hull and the work performed in [17], where the most cost-effective hopper volume for the ALERD is determined. This hopper volume will be used in this research as well, and is used to determine the ballast capacity of the main ballast tanks, which will be done in Chapter 3.

Table 2.1: Main dimensions of the ALERD

Parameter	Value	Unit
L	80	m
B	20	m
D	8.5	m
BG	0.43	m
Δ	10830	ton
Hopper Volume	2360	m^3

2.2. Overview Matlab Functions Used to Model the ALERD

In Figure 2.4 an overview of the Matlab functions, used for modelling the ALERD, is given. The original functions, which are listed below, and shown in Figure 2.4, are based on the method developed by Fossen [7] and can be found in the Marine Systems Simulator (MSS) library [6]. This library provides models for ships and underwater vehicles, and is free accessible. Therefore, the useful functions serve as a good starting point for the development of a simulation model for an underwater vehicle such as the ALERD. The Fossen approach for modelling and controlling underwater vehicles is widely used throughout the available literature, and can be seen as the state-of-the-art modelling approach. It is often used to model and simulate small underwater vehicles, such as AUVs.

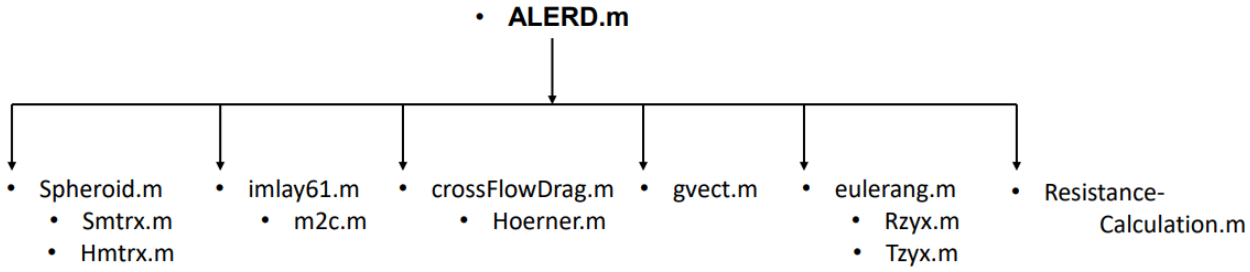

Figure 2.4: Matlab Function Overview

In the list below, the sections in which the different Matlab functions are described are given.

- Spheroid.m in Section 2.5.4
- Smtrx.m in Section 2.5.2
- Hmtrx.m in Section 2.5.4
- imlay61.m in Section 2.6.1
- m2c.m in Section 2.6.2

- gvect.m in Section 2.6.4
- Rzyx.m in Section 2.7.1
- Tzyx.m in Section 2.7.2
- crossFlowDrag.m in Section 2.8.1
- Hoerner.m in Section 2.8.1
- eulerang.m in Section 2.9

ALERD.m is the main Matlab function, in which the equations of motion are defined in 6 degrees of freedom (DoF), and the corresponding state-space representation is formulated. In this function, the other subfunctions from the list and Figure 2.4 are used. The state-space model is solved using Simulink for a given time period, in order to perform time-domain simulations. In the upcoming sections in this chapter, all the used Matlab functions will be described in detail.

2.3. Hydrodynamic Modelling of the ALERD

The hydrodynamics of underwater vehicles can be described using equations of motion in six DoF. The used notation for the position, velocities, forces, and moments can be found in Table 2.2. This notation is widely used in the literature and research about underwater vehicle hydrodynamics, and will be used throughout this report as well. The positive directions, rotations, and different reference frames can be found in Figure 2.5. These will be used throughout this report and in the simulation model as well. Important to note is that the positive z-direction is downwards. When reading figures and plots from the depth, this can feel counterintuitive, since a diving maneuver of the ALERD is indicated with a positive change in z.

Table 2.2: Used notation for 6 DOF equations of motion [7], [23]

DOF	Motions	Forces	Linear velocity	Positions
1	Surge	X	u	x
2	Sway	Y	v	y
3	Heave	Z	w	z
	Rotations	**Moments**	**Angular velocity**	**Rotation angles**
4	Roll	K	p	ϕ
5	Pitch	M	q	θ
6	Yaw	N	r	ψ

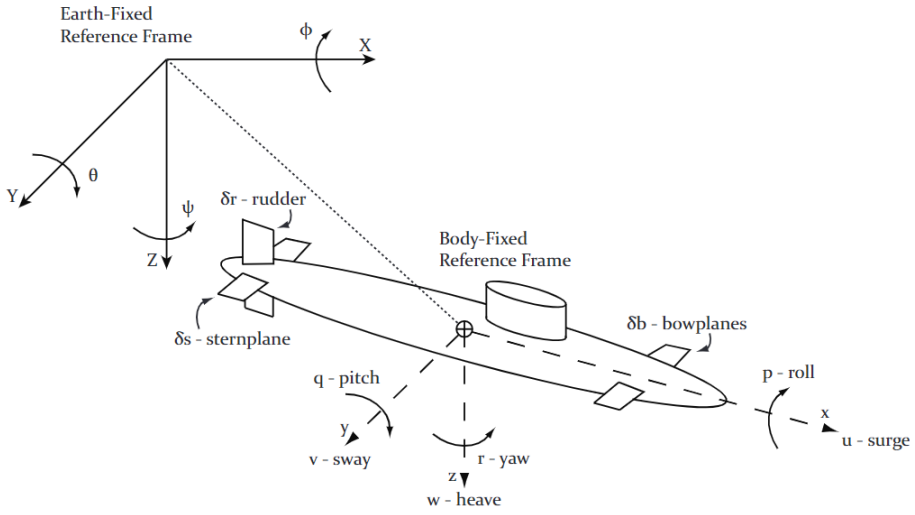

Figure 2.5: Coordinate frame definitions for underwater vehicles [18]

2.4. Equations of Motion for Underwater Vehicles

In Equation 2.1 the nonlinear ordinary differential equation of motion describing all 6 DoF for underwater vehicles can be seen. This equation is written in the widely used vectorial notation developed by Fossen [7].

$$\boldsymbol{M\dot{v}} + \boldsymbol{C(v)v} + \boldsymbol{D(v)v} + \boldsymbol{g(\eta)} = \boldsymbol{\tau} \tag{2.1}$$

Where:

- $\boldsymbol{M} = \boldsymbol{M_{RB}} + \boldsymbol{M_A}$ - System inertia matrix (including added mass)
- $\boldsymbol{C(v)} = \boldsymbol{C_{RB}(v)} + \boldsymbol{C_A(v)}$ - Coriolis-centripetal matrix (including added mass)
- $\boldsymbol{D(v)}$ - damping matrix
- $\boldsymbol{g(\eta)}$ - restoring gravitational and buoyancy forces

$$\boldsymbol{\eta} = \begin{bmatrix} x & y & z & \varphi & \theta & \psi \end{bmatrix}^{\mathsf{T}} \tag{2.2}$$

$$\boldsymbol{v} = \begin{bmatrix} u & v & w & p & q & r \end{bmatrix}^{\mathsf{T}} \tag{2.3}$$

$$\boldsymbol{\tau} = \begin{bmatrix} X & Y & Z & K & M & N \end{bmatrix}^{\mathsf{T}} \tag{2.4}$$

$\boldsymbol{\eta}$ and $\boldsymbol{v}$ are the position and velocity vector respectively, and $\boldsymbol{\tau}$ is the generalized vector with the external forces and moments. In the upcoming sections, the derivation of all the used matrices from equation 2.1 will be given, including the corresponding Matlab file from Figure 2.4.

2.4.1. Ellipsoidal Hull Form Assumption

The ALERD will be modelled as an underwater vehicle assuming the hull form to be ellipsoidal with port/starboard (xz) and fore/aft (yz) symmetry, leading to a reduced rigid body mass matrix, which can be found in equation 2.24. This approach makes it possible to parametrically vary the main dimensions of the hull, while the symmetry assumptions make it possible to disregard the off-diagonal terms in the mass and damping matrices. These terms cannot be calculated using mathematical expressions, but require more time-consuming and expensive approaches such as CFD-analysis, or scale model tests. According to the literature, the diagonal structure of these matrices can be seen as a quite good approximation for underwater vehicles operating at low to medium speed, since the off-diagonal terms are often much smaller [7].

The actual hull form of the ALERD will be based on the initial hull form of the AUMD, which is the predecessor of the ALERD, shown in Figure 1.1 and Figure 2.1. However, since no hydrodynamic data of this hull form is known at this point, the assumption of an ellipsoidal hull form is necessary to make, since it is not possible to set up the equations of motion otherwise.

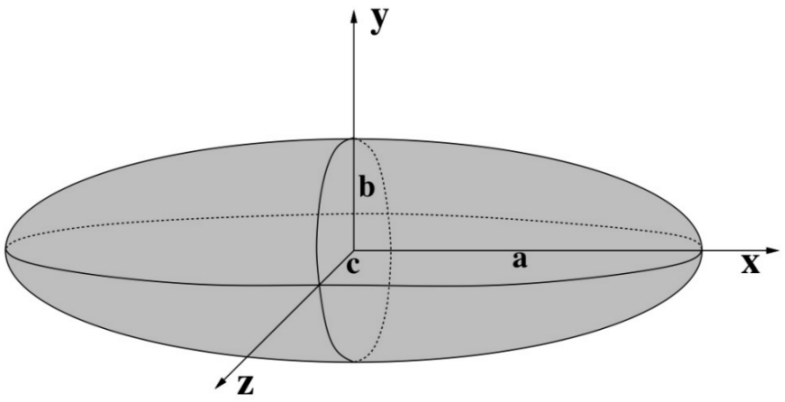

Figure 2.6: Prolate Ellipsoid

In Figure 2.6 a representation of a prolate ellipsoid can be found. A prolate ellipsoid is obtained by letting $b = c$ and $a > b$, resulting in the following expressions for the mass and the moments of inertia (see equation 2.5 and 2.6).

$$m = \frac{4}{3}\pi\rho abc = \frac{4}{3}\pi\rho ab^2 \tag{2.5}$$

$$\begin{aligned} I_{xx} &= \frac{1}{5}m\left(b^2 + c^2\right) = \frac{2}{5}mb^2 \\ I_{yy} &= \frac{1}{5}m\left(a^2 + c^2\right) = \frac{1}{5}m\left(a^2 + b^2\right) \\ I_{zz} &= \frac{1}{5}m\left(a^2 + b^2\right) = I_{yy} \end{aligned} \tag{2.6}$$

The value of $b = c$ is chosen in such a way that the mass of the prolate ellipsoid is equal to the mass of the ALERD, which can be found in Table 2.1. With equation 2.7 the corresponding diameter of the ellipsoid can be calculated, and this value will be used for both b and c [23].

$$\bar{d} = \left(\frac{6\Delta}{\pi\rho L}\right)^{0.5} \tag{2.7}$$

2.5. Rigid-Body Kinetics

2.5.1. Reference Frames

For the modelling of ships and underwater vehicles, different and multiple reference frames can be used. In the present simulation model for the ALERD, two different reference frames are used, which are the North-East-Down (**NED**) and body-fixed (**BODY**) reference frames. The corresponding coordinate systems are listed below;

- **NED**; $\{n\} = (x_n, y_n, z_n)$
- **BODY**; $\{b\} = (x_b, y_b, z_b)$

The two reference frames can also be found in Figure 2.7. The NED coordinate system (or inertial reference frame) is seen as a fixed coordinate system, while the body-fixed reference frame (BODY) is a moving coordinate frame which is fixed to the craft [7]. The position and orientation of a craft are described relative to the inertial reference frame ($\{n\}$). The linear and angular velocities of a craft are described in the body-fixed reference frame ($\{b\}$).

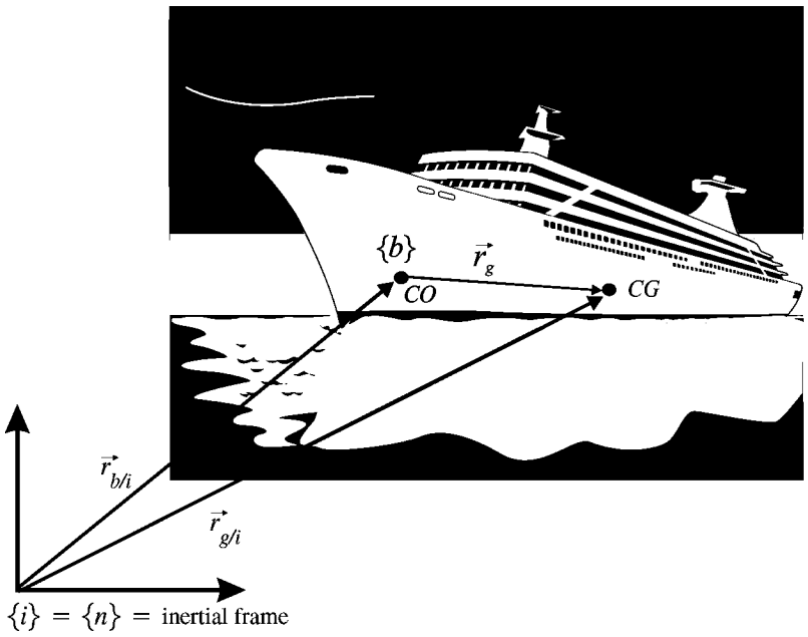

Figure 2.7: Definition of the inertia frame, and the origin of CO and CG [7]

Notation of the vectors
In the upcoming sections, the equations of motion from Equation 2.1 will be derived, following the methodology of Fossen, which is completely described in [7]. The vectors used for deriving the equations of motion can be found in Equation 2.8.

$$\begin{aligned}
&\boldsymbol{f}_b^b = [X, Y, Z]^\top && \text{- force through } o_b \text{ expressed in } \{b\} \\
&\boldsymbol{m}_b^b = [K, M, N]^\top && \text{- moment about } o_b \text{ expressed in } \{b\} \\
&\boldsymbol{v}_{b/n}^b = [u, v, w]^\top && \text{- linear velocity of } o_b \text{ relative to } o_n \text{ expressed in } \{b\} \\
&\boldsymbol{\omega}_{b/n}^b = [p, q, r]^\top && \text{- angular velocity of } \{b\} \text{ relative to } \{n\} \text{ expressed in } \{b\} \\
&\boldsymbol{r}_g^b = \left[x_g, y_g, z_g\right]^\top && \text{- vector from } o_b \text{ to CG expressed in } \{b\}
\end{aligned} \tag{2.8}$$

Definition of CO, CG and CB
The two reference frames and the definition of the origin of the body-fixed reference frame can be used to drastically simplify the equations of motion from Equation 2.1. This results in a decrease of the elements that need to be determined for these equations.

For the modelling of underwater vehicles, it is a common approach to assume that the center of buoyancy coincides with the center of the origin of the body-fixed frame $\{b\}$ ($CO = CB$), resulting in the vector $\boldsymbol{r}_{bb}^b = [0, 0, 0]$. The center of gravity is defined as $\boldsymbol{r}_{bg}^b = \left[x_g, y_g, z_g\right]$. Due to the assumption of multiple planes of symmetry, the vector can be reduced to $\boldsymbol{r}_{bg}^b = \left[0, 0, z_g\right]$, where z_g is equal to the vertical distance between the center of gravity to the center of buoyancy BG. The value of BG is already known for the ALERD and can be found in Table 2.1. This value will be used in the simulation model, even though the ALERD is mathematically modeled as an ellipsoid. As mentioned above, this leads to two instead of three symmetry planes.

2.5.2. Cross-Product Operator

The cross-product operator, also called S-matrix, is defined in the Matlab function Smtrx.m. This S-matrix can be used as cross-product operator, and can be used to calculate a cross-product with any other vector. This matrix is also used to construct the H-matrix, which is needed to convert the inertia matrix from CG to any arbitrary point, such as CO. The cross-product operator can be found in Equation 2.9, where the vector $\boldsymbol{\lambda}$ is an arbitrary vector, used to calculate the cross product with.

$$\boldsymbol{\lambda} \times \boldsymbol{a} := \boldsymbol{S}(\boldsymbol{\lambda})\boldsymbol{a}$$
$$\boldsymbol{S}(\boldsymbol{\lambda}) = -\boldsymbol{S}^{\mathsf{T}}(\boldsymbol{\lambda}) = \begin{bmatrix} 0 & -\lambda_3 & \lambda_2 \\ \lambda_3 & 0 & -\lambda_1 \\ -\lambda_2 & \lambda_1 & 0 \end{bmatrix} \tag{2.9}$$
$$\boldsymbol{\lambda} = \begin{bmatrix} \lambda_1 \\ \lambda_2 \\ \lambda_3 \end{bmatrix}$$

2.5.3. Translational and Rotational Motion about CG

To derive the inertia matrix and Coriolis-centripetal matrix in the equations of motion from Equation 2.1, the relationship between an inertial reference frame and a moving reference frame must be used. The two different frames can be found in Figure 2.5 and Figure 2.7. In Figure 2.7, the inertial (or earth-fixed) reference frame and body fixed reference frame can be seen, including the position vectors. Those vectors can be time-differentiated to obtain the velocities and accelerations. The complete mathematical derivation of the time-differentiation of vectors in moving reference frames can be found in [7] and will not be given here. The equations and derivations given here are relevant since they are used in the Matlab functions from Figure 2.4.

CO is the origin of the body fixed frame b, which is moving with an angular velocity vector $\boldsymbol{\omega}$ with respect to the inertial frame. As already mentioned, in the modelling of underwater vehicles, it is a common approach to locate CO at the center of buoyancy CB.

Newton's second law can be expressed in terms of conservation of both linear momentum and angular momentum. Expressing Newton's second law in terms of conservation of linear momentum and angular momentum, and writing it in vector notation, the following relationships for the velocity and rotation about CG can be derived, shown in Equation 2.10.

$$\begin{aligned} \vec{f}_g &= {}^{i}\frac{\mathrm{d}}{\mathrm{d}t}\left(m\vec{v}_{g/i}\right) \\ &= {}^{i}\frac{\mathrm{d}}{\mathrm{d}t}\left(m\vec{v}_{g/n}\right) \\ &= {}^{b}\frac{\mathrm{d}}{\mathrm{d}t}\left(m\vec{v}_{g/n}\right) + m\vec{\omega}_{b/n} \times \vec{v}_{g/n} \\ &= m\left(\dot{\vec{v}}_{g/n} + \vec{\omega}_{b/n} \times \vec{v}_{g/n}\right) \end{aligned} \tag{2.10}$$

$$m\left[\dot{\boldsymbol{v}}^b_{g/n} + \boldsymbol{S}\left(\boldsymbol{\omega}^b_{b/n}\right)\boldsymbol{v}^b_{g/n}\right] = \boldsymbol{f}^b_g \tag{2.11}$$

Using the cross-product operator S described above, and expressing the vectors from Equation 2.10 in the body fixed reference frame $\{b\}$, leads to Equation 2.11. The same approach can be followed for the rotational motion about CG.

$$\begin{aligned} \vec{m}_g &= {}^{i}\frac{\mathrm{d}}{\mathrm{d}t}\left(I_g\vec{\omega}_{b/i}\right) \\ &= {}^{i}\frac{\mathrm{d}}{\mathrm{d}t}\left(I_g\vec{\omega}_{b/n}\right) \\ &= {}^{b}\frac{\mathrm{d}}{\mathrm{d}t}\left(I_g\vec{\omega}_{b/n}\right) + \vec{\omega}_{b/n} \times \left(I_g\vec{\omega}_{b/n}\right) \\ &= I_g\dot{\vec{\omega}}_{b/n} - \left(I_g\vec{\omega}_{b/n}\right) \times \vec{\omega}_{b/n} \end{aligned} \tag{2.12}$$

$$\boldsymbol{I}_g\dot{\boldsymbol{\omega}}^b_{b/n} - \boldsymbol{S}\left(\boldsymbol{I}_g\boldsymbol{\omega}^b_{b/n}\right)\boldsymbol{\omega}^b_{b/n} = \boldsymbol{m}^b_g \tag{2.13}$$

Combining Equations 2.11 and 2.13 leads to the rigid-body equations of motion expressed in CG, which can be found in Equation 2.14.

$$\underbrace{\begin{bmatrix} m\boldsymbol{I}_{3\times3} & \boldsymbol{0}_{3\times3} \\ \boldsymbol{0}_{3\times3} & \boldsymbol{I}_g \end{bmatrix}}_{\boldsymbol{M}_{RB}^{CG}} \begin{bmatrix} \dot{\boldsymbol{v}}_{g/n}^b \\ \dot{\boldsymbol{\omega}}_{b/n}^b \end{bmatrix} + \underbrace{\begin{bmatrix} m\boldsymbol{S}\left(\boldsymbol{\omega}_{b/n}^b\right) & \boldsymbol{0}_{3\times3} \\ \boldsymbol{0}_{3\times3} & -\boldsymbol{S}\left(\boldsymbol{I}_g\boldsymbol{\omega}_{b/n}^b\right) \end{bmatrix}}_{\boldsymbol{C}_{RB}^{CG}} \begin{bmatrix} \boldsymbol{v}_{g/n}^b \\ \boldsymbol{\omega}_{b/n}^b \end{bmatrix} = \begin{bmatrix} \boldsymbol{f}_g^b \\ \boldsymbol{m}_g^b \end{bmatrix} \tag{2.14}$$

The inertia and Coriolis-centripetal matrices from Equation 2.14 need to be transformed to the arbitrary point CO, which is chosen to be coinciding with CB. To make this transformation, the H-matrix can be used, which will be derived in the next section.

2.5.4. H-Matrix

In this section, a derivation is given for the transformation of the equations of motion to an arbitrary origin CO, since this point can be used to take advantage of the ship geometry, and hydrodynamic forces and moments are often computed in this point as well. The translational and rotational motions around CG, derived in the previous section, are used. Furthermore, using Figure 2.7 and the position vectors, the transformation from CG to CO can be derived. The expression between the velocity of CG and CO, expressed in the body-fixed reference frame, $\{b\}$ can be found in Equation 2.16. This expression can be derived by time-differentiating the position vectors, which can be found in Figure 2.7 and in Equation 2.15. With Equation 2.16, the transformation matrix $\boldsymbol{H}\left(\boldsymbol{r}_g^b\right)$ can be derived. This derivation can be found in Equations 2.17, 2.18, and 2.19. The rigid-body equation of motion from Equation 2.14 can be transformed to CO with this transformation matrix, and the resulting expression, the rigid-body mass and Coriolis-centripetal matrices can be found in Equation 2.20, 2.21, and 2.22 respectively.

$$\vec{r}_{g/n} = \vec{r}_{b/n} + \vec{r}_g \tag{2.15}$$

$$\begin{aligned} \boldsymbol{v}_{g/n}^b &= \boldsymbol{v}_{b/n}^b + \boldsymbol{\omega}_{b/n}^b \times \boldsymbol{r}_g^b \\ &= \boldsymbol{v}_{b/n}^b - \boldsymbol{r}_g^b \times \boldsymbol{\omega}_{b/n}^b \\ &= \boldsymbol{v}_{b/n}^b + \boldsymbol{S}^\top\left(\boldsymbol{r}_g^b\right)\boldsymbol{\omega}_{b/n}^b \end{aligned} \tag{2.16}$$

$$\begin{bmatrix} \boldsymbol{v}_{g/n}^b \\ \boldsymbol{\omega}_{b/n}^b \end{bmatrix} = \boldsymbol{H}\left(\boldsymbol{r}_g^b\right)\begin{bmatrix} \boldsymbol{v}_{b/n}^b \\ \boldsymbol{\omega}_{b/n}^b \end{bmatrix} \tag{2.17}$$

$$\boldsymbol{H}\left(\boldsymbol{r}_g^b\right) := \begin{bmatrix} \boldsymbol{I}_{3\times3} & \boldsymbol{S}^\top\left(\boldsymbol{r}_g^b\right) \\ 0_{3\times3} & \boldsymbol{I}_{3\times3} \end{bmatrix} \tag{2.18}$$

$$\boldsymbol{H}^\top\left(\boldsymbol{r}_g^b\right) = \begin{bmatrix} \boldsymbol{I}_{3\times3} & 0_{3\times3} \\ \boldsymbol{S}\left(\boldsymbol{r}_g^b\right) & \boldsymbol{I}_{3\times3} \end{bmatrix} \tag{2.19}$$

$$\boldsymbol{H}^\top\left(\boldsymbol{r}_g^b\right)\boldsymbol{M}_{RB}^{CG}\boldsymbol{H}\left(\boldsymbol{r}_g^b\right)\begin{bmatrix} \dot{\boldsymbol{v}}_{b/n}^b \\ \dot{\boldsymbol{\omega}}_{b/n}^b \end{bmatrix} + \boldsymbol{H}^\top\left(\boldsymbol{r}_g^b\right)\boldsymbol{C}_{RB}^{CG}\boldsymbol{H}\left(\boldsymbol{r}_g^b\right)\begin{bmatrix} \boldsymbol{v}_{b/n}^b \\ \boldsymbol{\omega}_{b/n}^b \end{bmatrix} = \boldsymbol{H}^\top\left(\boldsymbol{r}_g^b\right)\begin{bmatrix} \boldsymbol{f}_g^b \\ \boldsymbol{m}_g^b \end{bmatrix} \tag{2.20}$$

$$\boldsymbol{M}_{RB}^{CO} := \boldsymbol{H}^\top\left(\boldsymbol{r}_g^b\right)\boldsymbol{M}_{RB}^{CG}\boldsymbol{H}\left(\boldsymbol{r}_g^b\right) \tag{2.21}$$

$$\boldsymbol{C}_{RB}^{CO} := \boldsymbol{H}^\top\left(\boldsymbol{r}_g^b\right)\boldsymbol{C}_{RB}^{CG}\boldsymbol{H}\left(\boldsymbol{r}_g^b\right) \tag{2.22}$$

The matrix $\boldsymbol{H}\left(\boldsymbol{r}_g^b\right)$ is defined in the Matlab function Hmtrx.m, and used, together with the function Smtrx.m, to calculate the rigid body mass and Coriolis-centripetal matrix in the Matlab function Spheroid.m. This is also shown in Figure 2.4. In the next section, the required elements in both matrices, required for modelling the ALERD, are filled in.

The derivations given in the sections above make it possible to use the simulation model for modelling underwater vehicles in 6 DoF. For simulating the ALERD, many simplifications in the equations above can be made, assuming low to medium speed operations, and by decoupling the 6 DoF using the assumption of diagonal matrices in the equations of motion. However, the derivations above are provided to give a complete overview of all the matrices and vectors that are used in the different Matlab functions. This section can therefore also be used as reference when using these functions, to understand the mathematical derivation and relationships behind the used matrices.

2.5.5. Rigid Body Matrix

The rigid body matrix, expressed in CG, can be found in Equation 2.14 and is a diagonal matrix. The expression of $\boldsymbol{H}\left(\boldsymbol{r}_g^b\right)$ is derived in the previous section, and is used to transform the rigid body matrix from CG to CO. This is done in Equation 2.23. Equation 2.24 shows the rigid body matrix in CO, with the elements which need to be determined for the ALERD. In Equations 2.23 and 2.24, it is clear to see that there are two planes of symmetry, and that CG is located below CB, which is equal to CO. The off-diagonal terms are due to the location of z_g, which does not correspond with CB (and thus CO). The operations described here are executed in the Matlab function Spheroid.m. The elements of the rigid body matrix can be filled in using the mass of the ALERD and the moments of inertia corresponding to a prolate ellipsoid, which are already derived in Section 2.4.1.

$$\boldsymbol{M}_{RB}^{CO} = \boldsymbol{H}^{\top}\left(\boldsymbol{r}_{bg}^b\right) \operatorname{diag}\left\{m, m, m, \frac{2}{5}mb^2, \frac{1}{5}m\left(a^2+b^2\right), \frac{1}{5}m\left(a^2+b^2\right)\right\} \boldsymbol{H}\left(\boldsymbol{r}_{bg}^b\right) \tag{2.23}$$

$$\boldsymbol{M}_{RB}^{CO} = \begin{bmatrix} m & 0 & 0 & 0 & mz_g & 0 \\ 0 & m & 0 & -mz_g & 0 & 0 \\ 0 & 0 & m & 0 & 0 & 0 \\ 0 & -mz_g & 0 & I_{xx} & 0 & 0 \\ mz_g & 0 & 0 & 0 & I_{yy} & 0 \\ 0 & 0 & 0 & 0 & 0 & I_{zz} \end{bmatrix} \tag{2.24}$$

2.5.6. Coriolis-centripetal Matrix

The corresponding Coriolis-centripetal matrix in CO can be found in equation 2.25. As already discussed in the previous sections, the Coriolis-centripetal matrix is due to the rotation of the body-fixed reference frame with respect to the inertial reference frame. The Coriolis-centripetal matrix in CG can be found in Equation 2.14. Similar as for the rigid body mass matrix, the operations to calculate and fill in this matrix are executed in the Matlab function Spheroid.m.

$$\boldsymbol{C}_{RB}^{CO}\left(\boldsymbol{v}_r\right) = \boldsymbol{H}^{\top}\left(\boldsymbol{r}_{bg}^b\right) \begin{bmatrix} 0 & -mr & mq & 0 & 0 & 0 \\ mr & 0 & -mp & 0 & 0 & 0 \\ -mq & mp & 0 & 0 & 0 & 0 \\ 0 & 0 & 0 & 0 & I_{zz}r & -I_{yy}q \\ 0 & 0 & 0 & -I_{zz}r & 0 & I_{xx}p \\ 0 & 0 & 0 & I_{yy}q & -I_{xx}p & 0 \end{bmatrix} \boldsymbol{H}\left(\boldsymbol{r}_{bg}^b\right) \tag{2.25}$$

2.6. Hydromechanics of Underwater Vehicles

In this section, the hydrodynamic coefficients for the ALERD are determined, which are the added mass and linear damping coefficients. Furthermore, the vector with hydrostatic restoring forces and moments is derived.

2.6.1. Added Mass Matrix

Based on the assumption that the hull form will be a prolate ellipsoid, in combination with the assumption that the ALERD will only be moving at low to medium speed, the off-diagonal terms of the added mass matrix are neglected. Different compared to the rigid-body matrix, for the added mass matrix, three planes of symmetry are assumed. This is due to the fact that off-diagonal terms cannot be determined using mathematical expressions. As already mentioned, this diagonal structure for the added mass matrix, is often seen as a good approximation. The diagonal terms from the added mass matrix can be estimated with Lamb's k-factors and the corresponding equations, described in [7], [13], [23]. The diagonal added mass matrix can be found in equation 2.26.

$$\boldsymbol{M}_A = \begin{bmatrix} X_{\dot{u}} & 0 & 0 & 0 & 0 & 0 \\ 0 & Y_{\dot{v}} & 0 & 0 & 0 & 0 \\ 0 & 0 & Z_{\dot{w}} & 0 & 0 & 0 \\ 0 & 0 & 0 & K_{\dot{p}} & 0 & 0 \\ 0 & 0 & 0 & 0 & M_{\dot{q}} & 0 \\ 0 & 0 & 0 & 0 & 0 & N_{\dot{r}} \end{bmatrix} \tag{2.26}$$

Lamb Equations for a Prolate Ellipsoid

The Equations for a prolate ellipsoid, needed to calculate the k-factors, can be found in Equation 2.27, 2.28, and 2.29. Lamb's k-factors can be found in Equation 2.30 and can be used to calculate the diagonal added mass coefficients. Due to the assumption of three symmetry planes for the added mass matrix, $Y_{\dot{v}} = Z_{\dot{w}}$ and $M_{\dot{q}} = N_{\dot{r}}$ [7], [28].

$$e = \sqrt{1 - \frac{b^2}{a^2}} \tag{2.27}$$

$$\alpha_0 = \frac{2\left(1 - e^2\right)}{e^3}\left[\frac{1}{2}\ln\left(\frac{1+e}{1-e}\right) - e\right] \tag{2.28}$$

$$\beta_0 = \frac{1}{e^2} - \frac{1 - e^2}{2e^3}\ln\left(\frac{1+e}{1-e}\right) \tag{2.29}$$

$$\begin{aligned} k_1 &= \frac{\alpha_0}{2 - \alpha_0} \\ k_2 &= \frac{\beta_0}{2 - \beta_0} \\ k' &= \frac{e^4\left(\beta_0 - \alpha_0\right)}{\left(2 - e^2\right)\left[2e^2 - \left(2 - e^2\right)\left(\beta_0 - \alpha_0\right)\right]} \end{aligned} \tag{2.30}$$

$$\begin{aligned} X_{\dot{u}} &= m \cdot k_1 \\ Y_{\dot{v}} = Z_{\dot{w}} &= m \cdot k_2 \\ M_{\dot{q}} = N_{\dot{r}} &= I_{yy} \cdot k' \\ K_{\dot{p}} &= r_{44} \cdot I_{xx} \end{aligned} \tag{2.31}$$

The value for the added mass in roll ($K_{\dot{p}}$) can be determined using r_{44}. In [7] typical values for r_{44} are in the range of 0.2 - 0.4. This value will be zero in case of the ALERD, since the roll moment is not considered during the simulations. The equations to calculate the added mass for a prolate ellipsoid are defined in the Matlab function Imlay61.m. In general, the elements in the added mass matrix are based on the hull form of a ship, and are therefore already expressed in the center of buoyancy CB of the ship. Since CO coincides with CB, the added mass and added mass Coriolis-centripetal do not need to be transformed.

2.6.2. Added Mass Coriolis-Centripetal Matrix

The corresponding added mass Coriolis-centripetal matrix about CO can be seen in equation 2.32. The derivation of this matrix and the added mass matrix is similar to the approach described for the rigid body mass and Coriolis-centripetal matrix, shown in Equation 2.14. The Coriolis-centripetal matrix is calculated in the Matlab function Imlay61.m, in combination with the function m2c.m. The function m2c.m uses the mass matrix in combination with the velocity vector (translational and rotational) to create the corresponding Coriolis-centripetal matrix. The mathematical derivation of the relationship defined in the function m2c.m and the corresponding matrices is given in [7] and will not be described here.

$$\boldsymbol{C}_A\left(\boldsymbol{\nu}_r\right) = \begin{bmatrix} 0 & 0 & 0 & 0 & -Z_{\dot{w}}w_r & Y_{\dot{v}}v_r \\ 0 & 0 & 0 & Z_{\dot{w}}w_r & 0 & -X_{\dot{u}}u_r \\ 0 & 0 & 0 & -Y_{\dot{v}}v_r & X_{\dot{u}}u_r & 0 \\ 0 & -Z_{\dot{w}}w_r & Y_{\dot{v}}v_r & 0 & -N_{\dot{r}}r & M_{\dot{q}}q \\ Z_{\dot{w}}w_r & 0 & -X_{\dot{u}}u_r & N_{\dot{r}}r & 0 & -K_{\dot{p}}p \\ -Y_{\dot{v}}v_r & X_{\dot{u}}u_r & 0 & -M_{\dot{q}}q & K_{\dot{p}}p & 0 \end{bmatrix} \tag{2.32}$$

2.6.3. Damping Matrix

Since there are no CFD calculations or model test results available, the damping coefficients need to be estimated. When operating at high speed, damping of underwater vehicles is highly non-linear and coupled, and the non-linear damping coefficients are dominant [7]. It is assumed that the ALERD will be operating at low to medium speed, where the linear damping terms are dominating [7]. Furthermore, the assumption is made that the ALERD is operating with decoupled motions, which is often seen as a good approximation [28]. With the used assumptions, only the linear damping therms need to be determined. The linear damping matrix will be diagonal, as can be seen in equation 2.33, and consists of potential damping and skin friction.

$$\boldsymbol{D} = \begin{bmatrix} X_u & 0 & 0 & 0 & 0 & 0 \\ 0 & Y_v & 0 & 0 & 0 & 0 \\ 0 & 0 & Z_w & 0 & 0 & 0 \\ 0 & 0 & 0 & K_p & 0 & 0 \\ 0 & 0 & 0 & 0 & M_q & 0 \\ 0 & 0 & 0 & 0 & 0 & N_r \end{bmatrix} \tag{2.33}$$

Due to the lack of data from reference ships, it is chosen to use the linear damping terms from an AUV and scale them with the ALERD. Results from calculations of the HRC-AUV from [28] are used. Due to the symmetry assumptions, $Y_v = Z_w$ and $M_q = N_r$. The values for the linear damping coefficients can be found in Table 2.3.

Table 2.3: Linear Damping Coefficients HRC-AUV [28]

Parameter	Value	Unit
X_u	181.45	$\frac{N}{m/s}$
Y_v	1219.8	$\frac{N}{m/s}$
Z_w	1219.8	$\frac{N}{m/s}$
K_p	126.62	$\frac{Nm}{rad/s}$
M_q	9096.9	$\frac{Nm}{rad/s}$
N_r	9096.9	$\frac{Nm}{rad/s}$

Scaling the damping coefficients to the size of the ALERD is done using the Froude scaling similarities between the ALERD and the HRC-AUV. The geometric and inertial values of the HRC-AUV can be found in [28]. The Froude numbers for both the HRC-AUV and ALERD are comparable using their design speeds and lengths.

$$F_n = \frac{V_s}{\sqrt{g \cdot L}} \tag{2.34}$$

$$F_{n,ALERD} = F_{n,AUV} \tag{2.35}$$

$$\lambda = \frac{L_{ALERD}}{L_{AUV}} \tag{2.36}$$

The linear damping coefficients of the HRC-AUV are multiplied with the Froude scaling law to obtain the coefficients of the ALERD. The used Froude scaling conversion factors can be found in Table 2.4. The linear damping coefficients in Equation 2.33 are dominating at low to medium speed, and are calculated in the main Matlab function ALERD.m.

Table 2.4: Froude Scaling Conversion Factors

Parameter	Unit	Scale Factor
Force	N	λ^3
Speed	m/s	$\lambda^{0.5}$
Moment	Nm	λ^4
Time	s	$\lambda^{0.5}$

Reynolds Scaling
In general, it is assumed that Froude scaling, which is done above, is not useable for submerged underwater vehicles, due to the absence of the free surface and waves. In fully submerged mode, only frictional and viscous damping terms are present [22]. The Reynolds similarity is another method to scale the linear damping coefficients from the model (HRC-AUV) to full scale (the ALERD). However, similar Reynolds numbers are normally impossible to achieve for a scale model and the actual ship, due to the fact that viscosity cannot be scaled. This can be explained by looking at the equation for the Reynolds number (Equation 2.37). A similar Reynolds number between the model (HRC-AUV) and full scale ship (ALERD), results in a very high required speed for the HRC-AUV.

$$Re = \frac{V_s \cdot L}{\nu} \tag{2.37}$$

Therefore, the Froude scaling conversion factors from Table 2.4 are used to scale the linear damping terms. The viscous resistance of the hull of the ALERD in the longitudinal direction is calculated using the Reynolds number, which is described in more detail in Section 2.8.2.

2.6.4. Restoring Forces and Moments Vector

For the ALERD, the restoring forces and moments vector will be constructed assuming that the initial weight is equal to the buoyancy ($W = B$).

The weight W of the ALERD is equal to mg, with the mass already known (see Table 2.1). The buoyancy B is equal to $\rho g \nabla$. The used convention for the signs and positive directions is shown in Figure 2.8. The vector with restoring forces and moments is calculated in the Matlab function gvect.m. The equations used in this function will be described in this section. The two vectors of the gravitational and buoyancy force can be seen in Equation 2.38 and 2.39 respectively. The complete vector with restoring forces and moments of an underwater vehicle can be found in equation 2.42. This vector is without derivation used in the function gvect.m, and therefore, a short mathematical derivation will be given in this section.

$$\boldsymbol{f}_g^n = \begin{bmatrix} 0 \\ 0 \\ W \end{bmatrix} \tag{2.38}$$

$$\boldsymbol{f}_b^n = -\begin{bmatrix} 0 \\ 0 \\ B \end{bmatrix} \tag{2.39}$$

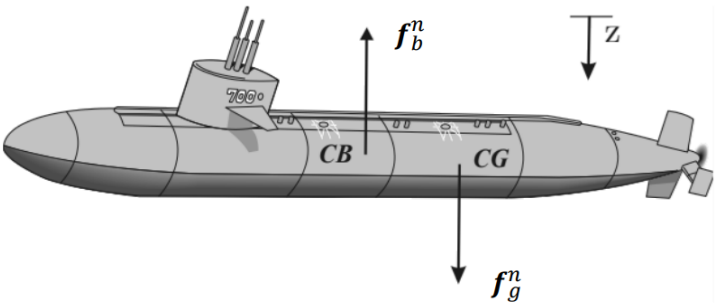

Figure 2.8: Used sign conventions for submarines

As can be seen in Figure 2.8, the gravitational force vector $\boldsymbol{f}_g^n$ and the buoyancy force vector $\boldsymbol{f}_b^n$ act in the vertical plane of the inertial reference frame $\{n\}$. If the ALERD is moving, the body fixed frame $\{b\}$ will move, so the force vectors need to be transformed from the $\{n\}$ frame to the $\{b\}$ frame. This can be done using the Euler angle transformations. Euler's transformations are in more detailed described in Section 2.7.1

The two vectors from Equations 2.38 and 2.39 can be rotated to the body-fixed frame $\{b\}$ using Euler rotations. This is done in Equation 2.40. The resulting forces and moments vector due to the

rotation is shown in Equation 2.41. The equations in this vector can be written out, leading to the vector shown in Equation 2.42.

$$\begin{aligned} \boldsymbol{f}_g^b &= \boldsymbol{R}_b^n \left(\boldsymbol{\Theta}_{nb}\right)^{-1} \boldsymbol{f}_g^n \\ \boldsymbol{f}_b^b &= \boldsymbol{R}_b^n \left(\boldsymbol{\Theta}_{nb}\right)^{-1} \boldsymbol{f}_b^n \end{aligned} \tag{2.40}$$

$$\boldsymbol{g}(\boldsymbol{\eta}) = -\begin{bmatrix} \boldsymbol{f}_g^b + \boldsymbol{f}_b^b \\ \boldsymbol{r}_g^b \times \boldsymbol{f}_g^b + \boldsymbol{r}_b^b \times \boldsymbol{f}_b^b \end{bmatrix} = -\begin{bmatrix} \boldsymbol{R}_b^n \left(\boldsymbol{\Theta}_{nb}\right)^{-1} \left(\boldsymbol{f}_g^n + \boldsymbol{f}_b^n\right) \\ \boldsymbol{r}_g^b \times \boldsymbol{R}_b^n \left(\boldsymbol{\Theta}_{nb}\right)^{-1} \boldsymbol{f}_g^n + \boldsymbol{r}_b^b \times \boldsymbol{R}_b^n \left(\boldsymbol{\Theta}_{nb}\right)^{-1} \boldsymbol{f}_b^n \end{bmatrix} \tag{2.41}$$

$$\boldsymbol{g}(\boldsymbol{\eta}) = \begin{bmatrix} (W-B)\sin(\theta) \\ -(W-B)\cos(\theta)\sin(\phi) \\ -(W-B)\cos(\theta)\cos(\phi) \\ -\left(y_g W - y_b B\right)\cos(\theta)\cos(\phi) + \left(z_g W - z_b B\right)\cos(\theta)\sin(\phi) \\ \left(z_g W - z_b B\right)\sin(\theta) + \left(x_g W - x_b B\right)\cos(\theta)\cos(\phi) \\ -\left(x_g W - x_b B\right)\cos(\theta)\sin(\phi) + \left(y_g W - y_b B\right)\sin(\theta) \end{bmatrix} \tag{2.42}$$

This vector can be reduced to the vector given in equation 2.43 assuming that $W = B$ and using the assumption of symmetry ($x_g = 0$, $y_g = 0$).

$$\boldsymbol{g}(\boldsymbol{\eta}) = \begin{bmatrix} 0 \\ 0 \\ 0 \\ z_g W \cos(\theta)\sin(\phi) \\ z_g W \sin(\theta) \\ 0 \end{bmatrix} \tag{2.43}$$

As mentioned, the vector from Equation 2.42 is used in the Matlab function gvect.m.

2.7. Transformation Between Reference Frames

In this section, the transformation matrices, used to transform the translational and rotational velocities from the body fixed $\{b\}$ frame to the inertial $\{n\}$ frame are derived.

2.7.1. Euler Angle Transformation

In Figure 2.7, the two reference frames, the body fixed $\{b\}$ frame and the inertial $\{n\}$ frame are shown. The velocity vector $\boldsymbol{v}_{b/n}^b$ orientated in one reference frame can be rotated to the other reference frame using Euler transformations, as shown in Equation 2.44. This can be done using the three Euler angles roll ϕ, pitch θ, and yaw ψ (Equation 2.45). Each Euler angle has its own rotation matrix, and in the simulation model, the zyx convention is used. This rotation sequence, and the corresponding Euler rotation matrix, are shown in Equation 2.46. This rotation matrix can be used to rotate a vector from $\{b\}$ to $\{n\}$. The transpose of this matrix can be used to rotate a vector from $\{n\}$ to $\{b\}$. In the Matlab function Rzyx.m, the rotation matrix shown in Equation 2.46 is calculated.

$$\boldsymbol{v}_{b/n}^n = \boldsymbol{R}_b^n \left(\boldsymbol{\Theta}_{nb}\right) \boldsymbol{v}_{b/n}^b \tag{2.44}$$

$$\boldsymbol{\Theta}_{nb} = [\phi, \theta, \psi]^\top \tag{2.45}$$

$$\boldsymbol{R}_b^n \left(\boldsymbol{\Theta}_{nb}\right) := \boldsymbol{R}_{z,\psi} \boldsymbol{R}_{y,\theta} \boldsymbol{R}_{x,\phi}. \tag{2.46}$$

The rotation matrix from Equation 2.46 with its elements can be seen in Equation 2.47. In this matrix, $c = cos(.)$ and $s = sin(.)$.

$$\boldsymbol{R}_b^n \left(\Theta_{nb}\right) = \begin{bmatrix} \mathrm{c}\psi\mathrm{c}\theta & -\mathrm{s}\psi\mathrm{c}\phi + \mathrm{c}\psi\mathrm{s}\theta\mathrm{s}\phi & \mathrm{s}\psi\mathrm{s}\phi + \mathrm{c}\psi\mathrm{c}\phi\mathrm{s}\theta \\ \mathrm{s}\psi\mathrm{c}\theta & \mathrm{c}\psi\mathrm{c}\phi + \mathrm{s}\phi\mathrm{s}\theta\mathrm{s}\psi & -\mathrm{c}\psi\mathrm{s}\phi + \mathrm{s}\theta\mathrm{s}\psi\mathrm{c}\phi \\ -\mathrm{s}\theta & \mathrm{c}\theta\mathrm{s}\phi & \mathrm{c}\theta\mathrm{c}\phi \end{bmatrix} \tag{2.47}$$

2.7.2. Angular Velocity Transformation

The body-fixed angular velocity vector $\boldsymbol{\omega}_{b/n}^{b} = [p, q, r]^{\top}$ can be transformed to the Euler rate vector (Equation 2.48) with the transformation matrix $\boldsymbol{T}_{\Theta}(\Theta_{nb})$. This is also shown in Equation 2.49. The transformation matrix including its elements is shown in Equation 2.50, where $s = sin(.)$, $c = cos(.)$, and $t = tan(.)$. The complete derivation of this matrix can be found in [7].

$$\dot{\boldsymbol{\Theta}}_{nb} = [\dot{\phi}, \dot{\theta}, \dot{\psi}]^{\top} \tag{2.48}$$

$$\dot{\boldsymbol{\Theta}}_{nb} = \boldsymbol{T}_{\Theta}(\boldsymbol{\Theta}_{nb})\, \boldsymbol{\omega}_{b/n}^{b} \tag{2.49}$$

$$\boldsymbol{T}_{\Theta}(\boldsymbol{\Theta}_{nb}) = \begin{bmatrix} 1 & \mathrm{s}\phi\mathrm{t}\theta & \mathrm{c}\phi\mathrm{t}\theta \\ 0 & \mathrm{c}\phi & -\mathrm{s}\phi \\ 0 & \mathrm{s}\phi/\mathrm{c}\theta & \mathrm{c}\phi/\mathrm{c}\theta \end{bmatrix} \tag{2.50}$$

The transformation matrix from Equation 2.50 is calculated in the Matlab function Tzyx.m, where the zyx convention is used. The transformation matrix $\boldsymbol{T}_{\Theta}(\boldsymbol{\Theta}_{nb})$, as well as the transformation matrix defined in the previous section ($\boldsymbol{R}_{b}^{n}(\boldsymbol{\Theta}_{nb})$), are used to define the state-space representation. This will be discussed in more detail in Section 2.9.

2.8. Hydrodynamic Forces and Moments

The right-hand side of the equations of motion (Equation 2.1) consists of the all the forces and moments, acting on the ALERD. The used hydrodynamic forces and moments in the simulation model are the cross-flow drag, viscous drag and control forces and moments. In the sections below, each of them will be described in more detail.

2.8.1. Cross-Flow Drag

The cross-flow drag principle, which can be seen as nonlinear damping, is included in the simulation model and the main function ALERD.m. If a ship has a large relative current angle (Equation 2.51), additional damping forces in heave and sway, and damping moments in pitch and sway are generated.

$$|\beta_c - \psi| \gg 0 \tag{2.51}$$

In Equation 2.51, β_c is the current direction. The description and the possibility to implement ocean current in the simulation model is described in more detail in Section 2.10. If there is no current applied, the resulting cross-flow drag forces and moment are equal to zero.

The cross-flow drag forces and moments are calculated in the Matlab function crossFlowDrag.m. The complete equations for the nonlinear damping forces and moments can be found in [7]. The 2-D drag coefficient, which is based on Hoerner's curve, is used in these equations and calculated in the separate Matlab function Hoerner.m. This coefficient is a function of the beam B and draft T of a ship, and can be found in Figure 2.9. Based on this ratio, the corresponding coefficient can be calculated and used in the equations for the cross-drag forces and moments.

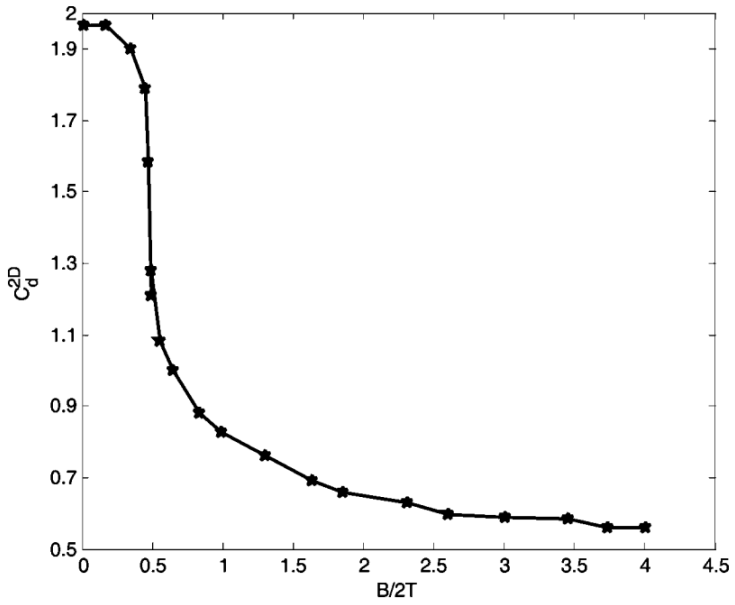

Figure 2.9: 2-D crossflow coefficient [7]

2.8.2. Bare Hull Resistance

In addition to the linear drag coefficients and the cross-flow drag, the drag of the hull in longitudinal direction, consisting of the form and viscous resistance, is calculated. Since the ALERD is fully submerged during its operations, the wave making and wave breaking resistance can be neglected. In [8] resistance calculations are made in order to calculate the required propulsion power. These calculations are slightly adjusted based on [21] and implemented into the simulation model. In [21] analytical bare hull resistance calculations for submerged ships are compared with CFD simulations, and it is concluded that the used equations give accurate results. In [21], the total resistance coefficient C_T is used to calculate the total resistance, and this coefficient is shown in Equation 2.54. The total resistance is acting only in the surge direction and is calculated using Equation 3.25. In this equation, V_s is the horizontal ship speed, S is the wetted surface of the hull, C_{F0} is the skin friction coefficient from the ITTC'57 friction line (Equation 2.53) and $(1+k)$ is the form factor. From earlier studies in [8] it can be concluded that for the ALERD, using the main parameters from Table 2.1, $S = 3900m^2$, $V_s = 8.5kts$, and the form factor is $(1+k) = 1.1$. The Reynolds number is calculated with Equation 2.37, and the kinematic viscosity of water at 10^o is $\nu = 1.354 \cdot 10^{-6} m^2/s$.

$$R_T = \frac{1}{2} \cdot \rho \cdot V_s^2 \cdot S \cdot C_T \cdot (1+k) \tag{2.52}$$

$$C_{F0} = \frac{0.075}{\left(\log_{10}(Re) - 2\right)^2} \tag{2.53}$$

$$C_T = C_{F0}(1 + 1.5(\frac{D}{L})^{1.5} + 7(\frac{D}{L})^3)) \tag{2.54}$$

The equations used above are implemented in the Matlab file ResistanceCalculation.m, which is used in the main function ALERD.m. The resulting force vector is shown in Equation 2.55.

$$\boldsymbol{\tau_{R_T}} = \begin{bmatrix} -R_T \\ 0 \\ 0 \\ 0 \\ 0 \\ 0 \end{bmatrix} \tag{2.55}$$

The calculated resistance force is only acting in surge direction, and is dependent on the forward speed. This is also shown in the force vector from Equation 2.55. This vector is already expressed in the $\{b\}$ frame, and is therefore not transformed. Furthermore, using the assumption of small angles, there is no need to use rotation matrices, for rotating the force when having a pitch angle for example.

2.8.3. Control Forces and Moments

The vector $\boldsymbol{\tau}$ contains, besides the hydrodynamic forces and moments described above, the control forces and moments for the DoF that are controlled using a motion controller. Each DoF that is controlled will have a separate actuator to produce the required restoring forces and moments. The control input for the different actuators, as well as their modelling, will be described in detail in Chapter 3. The forces and moments that are used to control the ALERD will all be expressed in the body-fixed ($\{b\}$) reference frame.

2.9. State-Space Model

The mathematical model of the ALERD with the equations of motion can be expressed as a state-space model and solved using Simulink. Using the equations of motion, a state-space model is defined, which can be found in equation 2.56 [7].

$$\boldsymbol{f}(\boldsymbol{x},\boldsymbol{u}) = \begin{bmatrix} \boldsymbol{M}^{-1}[\boldsymbol{\tau} + \boldsymbol{\tau}_{\boldsymbol{R_T}} + \boldsymbol{\tau}_{\boldsymbol{crossflow}} - \boldsymbol{C}(\boldsymbol{v})\boldsymbol{v} - \boldsymbol{D}(\boldsymbol{v})\boldsymbol{v} - \boldsymbol{g}(\boldsymbol{\eta})] \\ \boldsymbol{J}(\boldsymbol{\eta})\boldsymbol{v} \end{bmatrix} \tag{2.56}$$

$$\boldsymbol{f}(\boldsymbol{x},\boldsymbol{u}) = \dot{\boldsymbol{x}} = \begin{bmatrix} \dot{\boldsymbol{v}}^{\mathrm{T}}, & \dot{\boldsymbol{\eta}}^{\mathrm{T}} \end{bmatrix}^{\mathrm{T}} \tag{2.57}$$

$$\dot{\boldsymbol{v}} = \begin{bmatrix} \dot{u} & \dot{v} & \dot{w} & \dot{p} & \dot{q} & \dot{r} \end{bmatrix}^{\mathrm{T}} \tag{2.58}$$

$$\dot{\boldsymbol{\eta}} = \boldsymbol{J}(\boldsymbol{\eta})\boldsymbol{v} \tag{2.59}$$

$$\dot{\boldsymbol{\eta}} = \begin{bmatrix} \dot{x} & \dot{y} & \dot{z} & \dot{\phi} & \dot{\theta} & \dot{\psi} \end{bmatrix}^{\mathrm{T}} \tag{2.60}$$

$$\boldsymbol{J}(\boldsymbol{\eta}) = \begin{bmatrix} \boldsymbol{R}_b^n(\boldsymbol{\Theta}_{\mathrm{nb}}) & 0_{3\times3} \\ 0_{3\times3} & \boldsymbol{T}_\Theta(\boldsymbol{\Theta}_{\mathrm{nb}}) \end{bmatrix} \tag{2.61}$$

$$\boldsymbol{x} = \begin{bmatrix} \boldsymbol{v}^{\mathrm{T}}, & \boldsymbol{\eta}^{\mathrm{T}} \end{bmatrix}^{\mathrm{T}} \tag{2.62}$$

$$\boldsymbol{v} = \begin{bmatrix} u & v & w & p & q & r \end{bmatrix}^{\mathrm{T}} \tag{2.63}$$

$$\boldsymbol{\eta} = \begin{bmatrix} x & y & z & \phi & \theta & \psi \end{bmatrix}^{\mathrm{T}} \tag{2.64}$$

$$\boldsymbol{x}_0 = \begin{bmatrix} \boldsymbol{v}_0^{\mathrm{T}}, & \boldsymbol{\eta}_0^{\mathrm{T}} \end{bmatrix}^{\mathrm{T}} \tag{2.65}$$

The state-space model from Equation 2.56 consists of the vector with accelerations and velocities of the ALERD (Equation 2.57 and 2.58). The accelerations can be determined by re-writing the equations of motion in terms of the acceleration. The vector $\dot{\boldsymbol{\eta}}$ (Equation 2.60) can be determined using Equation 2.59. In Equation 2.56 and 2.59, $\boldsymbol{J}(\boldsymbol{\eta})$ is the Euler angle transformation matrix, used to transform the velocity vector (with translational and rotational velocities) from the body-fixed frame $\{b\}$ to the inertial frame $\{n\}$, to calculate the vector $\dot{\boldsymbol{\eta}}$. The Euler transformation matrix can be found in Equation 2.61 and is calculated in the Matlab function eulerang.m. This function uses the transformation matrices derived in Section 2.7.

The equations can be solved for $\dot{\boldsymbol{x}}$ and integrated using Simulink to obtain the vector $\boldsymbol{x}$, which gives the position and orientation vector $\boldsymbol{\eta}$ of the ALERD with respect to the inertial frame $\{n\}$, as well as the velocity vector $\boldsymbol{v}$. Those two vectors are given in Equations 2.64 and 2.63 respectively.

The state vector defined in Equation 2.65 is used as initial input vector for the state-space model. With this initial input, the state-space model can be solved. The solution of the state-space model is the

vector $\dot{\boldsymbol{x}}$, which can be seen in equations 2.56 and 2.57. This vector is integrated to obtain an updated version of the vector $\boldsymbol{x}$, which serves as the new input vector for the state-space model. By repeating these steps for a certain given time frame, a time-domain simulation can be performed.

2.10. Ocean Current

Ocean currents can be implemented in the simulation model as an optional environmental disturbance. It is assumed that the current is irrotational and constant. The current speed and direction can be defined and used as input for the simulations. Using the approach described in [7], the current forces and moments can be implemented into the equations of motion. This can be achieved by replacing the absolute velocity vector with a relative velocity vector. The relative velocity can be calculated using Equation 2.66.

$$\boldsymbol{v_r} = \boldsymbol{v} - \boldsymbol{v_c} \tag{2.66}$$

The ocean current speed vector expressed in $\{b\}$ can be found in Equation 2.67.

$$\boldsymbol{v}_c = [\underbrace{u_c, v_c, w_c}_{\boldsymbol{v}_c^b}, 0, 0, 0]^\top \tag{2.67}$$

If current is applied in the simulation model, the relative velocity vector from Equation 2.66 must be used to determine the hydrodynamic terms of the Coriolis centripetal matrices and the damping matrices in the equations of motion, since these are velocity dependent. In [7] it is shown that the rigid body terms are independent of the linear velocity vector $\boldsymbol{v} = [u, v, w]^\top$. Therefore, for both the rigid body terms and the hydrodynamic terms, the velocity vector can be replaced with the relative velocity vector, which is shown in Figure 2.68. The complete mathematical derivation of Equation 2.68 can be found in [7], and is considered out of scope of this report.

$$\boldsymbol{M}\dot{\boldsymbol{v}}_r + \boldsymbol{C}(\boldsymbol{v}_r)\boldsymbol{v}_r + \boldsymbol{D}(\boldsymbol{v}_r)\boldsymbol{v}_r + \boldsymbol{g}(\boldsymbol{\eta}) + \boldsymbol{g}_0 = \boldsymbol{\tau} \tag{2.68}$$

2D Current Model

In the main Matlab function ALERD.m, 2D current can be applied, using two input variables V_c and β_c. V_c is the ocean current speed, and β_c is the direction of the current, with respect to the ship, expressed in the $\{n\}$ frame.

The ocean current is expressed in the body-fixed $\{b\}$ frame, using Equation 2.69. Note that Equation 2.69 shows that $V_c = \sqrt{u_c^2 + v_c^2}$. In this equation, ψ is the yaw angle of the ship.

$$\boldsymbol{v}_c^b = \begin{bmatrix} V_c \cos(\beta_c - \psi) \\ V_c \sin(\beta_c - \psi) \\ 0 \end{bmatrix} = \begin{bmatrix} u_c \\ v_c \\ w_c \end{bmatrix} \tag{2.69}$$

2.10.1. State-Space Model Including Current

If current is applied in the simulation model, the velocity vector in the equations of motions is replaced with the relative velocity vector from equation 2.66. The application of current will also lead to a different state-space model. The new state-space model, including ocean current, can be found in equation 2.70. The time-derivative of the current velocity vector ($\dot{\boldsymbol{v}}_c$) is added to the state-space model as additional acceleration, and the velocity vector in the equations of motion is replaced by the relative velocity vector. The additional acceleration vector due to the current can be found in Equation 2.71. If the input variables V_c and β_c are equal to zero, the state-space model reduces to the original state-space model from Equation 2.56.

$$\boldsymbol{f}(\boldsymbol{x}, \boldsymbol{u}) = \begin{bmatrix} \dot{\boldsymbol{v}}_c + \boldsymbol{M}^{-1}[\boldsymbol{\tau} + \boldsymbol{\tau}_{R_T} + \boldsymbol{\tau}_{crossflow} - \boldsymbol{C}(\boldsymbol{v}_r)\boldsymbol{v}_r - \boldsymbol{D}(\boldsymbol{v}_r)\boldsymbol{v}_r - \boldsymbol{g}(\boldsymbol{\eta})] \\ \boldsymbol{J}(\boldsymbol{\eta})\boldsymbol{v}_r \end{bmatrix} \tag{2.70}$$

$$\dot{\boldsymbol{v}}_{\boldsymbol{c}}^{\boldsymbol{b}} = \begin{bmatrix} \dot{\psi} V_c \sin(\beta_c - \psi) \\ -\dot{\psi} V_c \cos(\beta_c - \psi) \\ 0 \\ 0 \\ 0 \\ 0 \end{bmatrix} \tag{2.71}$$

2.11. Overview Simulink Model

In Figure 2.10, a complete schematic overview of the simulation model made in Simulink is given. In this chapter, the main Matlab function ALERD.m with the state-space model is derived. This function is used in Simulink to perform time-domain simulations. The state-space model calculates the actual state of the ALERD based on the input state vector, which is compared with the desired state. The desired state is based on the control objectives of the ALERD, which will be defined using the operational profile. Motion controllers are used to calculate the necessary input for the actuators, needed to provide the restoring forces and moments required to bring the error to zero.

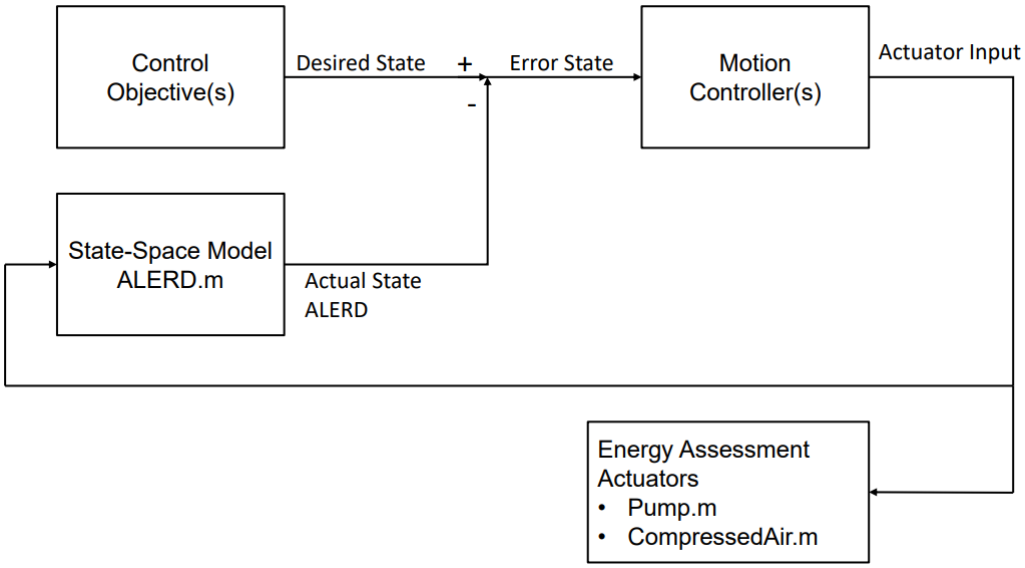

Figure 2.10: Schematic Overview Simulink Simulation Model

In Chapter 3, the control objectives for the ALERD will be defined, and the used motion controllers will be described. The actuator input, which is the output of the controllers, is used as input for the Matlab function ALERD.m, where it is translated into required forces and moments.

The actuator input will also be used to calculate the corresponding power and energy requirements for the physical systems, used to deliver the required forces and moments. Two separate Matlab functions, Pump.m and CompressedAir.m, are used to translate the actuator input to energy requirements, taking into account the corresponding physical systems. These two functions, as well as the physical systems used to provide the necessary restoring forces and moments, will be described in Chapter 4.

3

Motion Control

In this chapter, the motion control methods, which will be used in the simulation model, are described. The defined state-state space model from the previous chapter has 6 DoF that can be controlled, in order to achieve predefined control objectives. The control objectives are based on the operational profile of the ALERD and will be defined in the upcoming sections. To create a benchmark model with simulation results, proportional-integral-derivative (PID) control is used. The more advanced control method Model Predictive Control (MPC) is used to compare the results from the PID controller with, to show the potential advantages and disadvantages, and in the end to minimize the energy requirements for controlling the motions of the ALERD.

3.1. Control Objectives

The motions in the 6 DoF described in Chapter 2 are often divided into slightly or non-interacting motions. In the literature, this is seen as a valid assumption, due to the vehicle symmetry assumptions and low to medium speed operations [28]. The 6 equations of motion can also be divided into two different subsystems, which are listed below. The longitudinal subsystem considering surge, heave, and pitch is the basis for forward speed control and depth/diving control. The lateral subsystem considering sway, roll, and yaw can be used for heading control. The two subsystems are listed below, and the used notation can be found in Table 2.2.

- Longitudinal subsystem with states: x, z, u, w, q and θ
- Lateral subsystem with states: y, v, p, r, ϕ and ψ

For the ALERD, the focus will be on the longitudinal subsystem, in which the forward speed, pitch, and depth are controlled. It is assumed that controlling the motions in heave and pitch will require the most energy for stability and buoyancy control. The energy consumption due to the forward speed (control) is based on the required power for propulsion, and is not affecting the energy requirement for stability and buoyancy control. The disturbances due to the dredging and discharging operations will mainly influence the heave and pitch motion, which will be described in more detail in Section 3.1.3. Motions in roll are often neglected for underwater vehicles according to the literature. Since it is expected that the ALERD is operating at low to medium speed, it assumed that additional roll moments can be compensated with a positive value of BG, rather than requiring active ballast systems. However, the dredging and discharging operations can influence the roll motions, for instance if the hopper is not symmetrically loaded. This is not taken into account in the current research, but is highly recommended for future research. The heading can be controlled using rudders in combination with propellers, which do not directly influence the energy requirements for stability and buoyancy control.

Taking in account all these considerations, the primary control objectives will be controlling the motions from the longitudinal subsystem, which will be done using proportional-integral-derivative control (PID control), to create a benchmark, and Model Predictive Control (MPC), as more advanced and promising control method for complex systems such as underwater vehicles.

From the longitudinal subsystem, the state z will be actively controlled, which is the actual depth of the ALERD. As will be described in the next section, the operational profile of the ALERD requires multiple changes in depth. The state w, which is the vertical (heave) velocity, is a direct result of

controlling the depth, since a change in depth leads to a change in vertical heave velocity. Furthermore, the pitch angle θ will be actively controlled. The state q, which is the pitch rate, is directly coupled with controlling the pitch angle θ. Controlling the depth z and pitch angle θ is seen as the basis to assess the energy requirement for stability and buoyancy control of the ALERD.

The forward speed u will be controlled using a speed controller, to create a more realistic operational profile. The changing speeds during the operational profile will also be covered in the next section. A changing forward speed will result in a changing position in x direction, and possibly in y direction if a heading controller is used.

3.1.1. Operational Profile ALERD

The control objectives for the ALERD are based on the operational profile of conventional dredgers, which is provided in an operational profile analysis made by C-Job [11]. In this operational profile analysis, AIS-data is analyzed from conventional dredgers doing coastal replenishment along the Dutch coastline. Three different operational modes can be distinguished, which combined form one complete operational cycle. The three different operational modes are listed below;

- Dredging
- Transit
- Discharging

Each operational mode has its own characteristics, such as water depth, speed, and duration. In the operational profile analysis, the median of the data points is calculated using AIS-data from 12 different dredgers. These values are used to determine the operational profile of the ALERD. The data of the operational profile from conventional dredgers can be found in Table 3.1.

Table 3.1: Operational Profile Data

Operational Mode	**Dredging**	**Transit**	**Discharging**	**Total Cycle**	**Unit**
Speed	1.7	10.7	0.2	-	[kn]
Median Water Depth	21	16	8	-	[m]
Maximum Water Depth	29.5	-	-	-	[m]
Minimum Water Depth	-	6	4	-	[m]
Time Duration	32%	52%	16%	100%	[-]
Time Duration	56	91	28	175	[min]

The median of the transit speed is 10.7 knots, as can be seen in Table 3.1, and is calculated using the AIS data from conventional dredgers which were active in the Dutch coastline care. In [10] an optimal transit speed for the ALERD is calculated, which is equal to 8.5 knots. Using this speed, the transit duration will increase, leading to an increase in the total cycle time. The new values for the duration, including the optimal transit speed, can be found in Table 3.2.

Table 3.2: Operational profile with optimal transit speed

Operational Mode	**Dredging**	**Transit**	**Discharging**	**Total Cycle**	**Unit**
Speed	1.7	8.5	0.2	-	[kn]
Time Duration	56	116	28	200	[min]
Time Duration	28%	58%	14%	100%	[-]

The depth for each different operational mode is used to generate a reference depth signal in z-direction, that is used as a control objective. Furthermore, the speed for the different modes is the basis for the forward speed controller. The time duration of the dredging and discharging operation can be used to determine the rate of change in cargo weight (dredged soil) inside the hopper, which needs to be compensated with active ballast systems.

Vertical Diving & Surfacing Speed

What is different, compared to conventional dredgers, is that the ALERD will be operating below the water surface. Therefore, there is an additional operational mode, which is the change of depth of the

ALERD. The change of depth consists of diving and surfacing, and it is assumed that these operations are done during the transit mode, before the start of the dredging or discharging operation.

In previous studies, performed by C-Job, additional information about submarines is provided by MARIN. According to MARIN, navy submarines have a typical vertical dive speed of 1 m/s. This is considered to be too quick for the ALERD, taking into account safety considerations, the autonomous operations, the shallow water depth in the operational area of the ALERD, and the fact that navy submarines are also designed to perform emergency dives. Therefore, it is assumed that the maximum vertical speed w will be 0.1 m/s. In other words, the ALERD can rise or descend 1 meter in 10 seconds. Diving or descending takes place during the transit mode, which is also shown in Figure 3.1.

3.1.2. Reference Signals for Control Objectives

The control objectives (the reference signals) will be created in Simulink using the signal generator. In these generators, the reference signal for the depth (z) and the pitch angle (θ) are defined.

Reference Signal for the Depth

The reference signal for z is based on Table 3.1. The actual value for z is measured using the position of the origin of $\{b\}$ (CO) with respect to the inertial frame $\{n\}$. In other words, z is the position of the center of buoyancy, since in Chapter 2 it is defined that CO = CB. For each operational mode, the median water depth is known, and especially for the transit mode, this is a relevant parameter. From the literature study, which was done in preparation for this report, it is concluded that both the near-bottom and the near-surface effect can have a significant effect on underwater vehicles, in terms of additional resistance and lift forces. This fact, in combination with the diameter of the ALERD and the relatively shallow water depth of the North-sea area, leads to the assumption that during transit mode, the center of origin of the hull (CB=CO) will be halfway the total water depth, for which 8 meters is chosen.

It is assumed that the dredging operations will be executed two meters above the seabed, measured with respect to the bottom of the hull. The depth of CO during the dredging operations will therefore be the bottom clearance of two meters, plus half the diameter of the ALERD. The diameter is defined in Table 2.1 and is equal to 8.5 meters. Therefore, the reference of z during dredging operations will be 5.75 meters measured from the seafloor. Measured from the surface, taking into account the depth of 21 meters, the z-position of the CO is 14.75 meters, and as can be seen in Figure 3.1, this number is rounded to 15 meters.

As shown in Table 3.1, discharging will take place in shallow water. Conventional dredgers are discharging in a water depth of eight meters. This is too shallow, since the initial height of the ALERD is 8.5 meters. Therefore, it is assumed that discharging will take place at the minimum distance of CO with respect to the water surface, which is equal to z is 4.25 meters. In this way, the ALERD is at least submerged, assuming calm water without waves.

In Figure 3.1, the desired signal for the z-position of CO of the ALERD is shown. Due to the downward positive z-direction (as defined in Figure 2.5), a change in depth is indicated with a positive value for z.

A few important notes must be made, looking at the reference signal for the depth in Figure 3.1. A reference signal is used for the motion control method as a control objective, which in this case is reference tracking. If the used motion controller is well-designed, it is capable of tracking every reference signal that is defined and used as input. Therefore, the controller design is more important than the definition of the reference signal when developing a simulation model using motion controllers.

The changes in depth, both diving and rising, determine the total amount of required energy, and are therefore the most important to take into account, to be able to accurately estimate the required amount of energy. For the reference signal of the depth, it is therefore chosen to make it as realistic as possible with the available information, considering the realistic maximum water depths for each operational mode, in the operational area of the ALERD, and the corresponding required changes in depth.

The start and end of the simulation are both at $z = 0$, which in fact means that the upper half of the ALERD is above the water surface. This is done purely illustrative, since the simulation model including the equations of motion do not consider the surfaced condition. For the surfaced condition of underwater vehicles, all kinds of different hydrodynamic and stability effects are introduced, which are out of scope of this research. The surfaced condition can be seen as starting in the harbor, and ending

in the harbor, which concludes one complete operational cycle. It is more likely that the ALERD will do 3 or more dredging and discharging cycles, within one complete operational cycle, before finishing in the harbor. It this turns out to be the case, the reference signal can be adjusted, by just adding additional transit, dredging, and discharging operations.

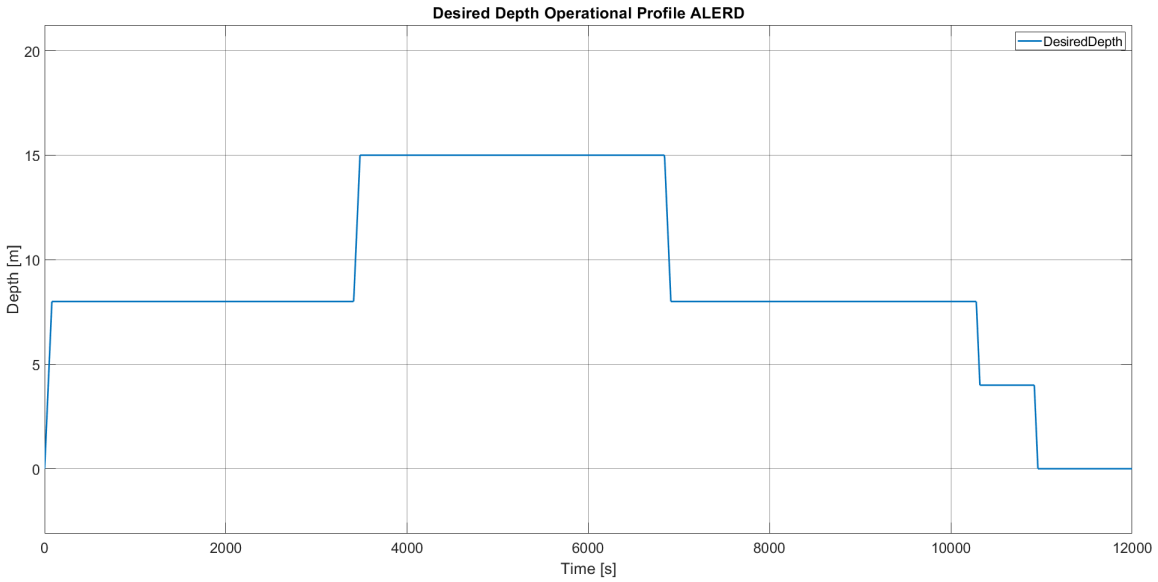

Figure 3.1: Reference signal for the z-position

Reference Signal for the Pitch Angle

The second control objective is the pitch angle θ. Since it is expected that the ALERD will mainly operate in shallow waters, it is important to keep the pitch angle at zero degrees, considering the hull length of 80 meters and expected maximum water depth of around 21 meters. Therefore, the control objective is to keep the pitch angle at zero degrees at all times.

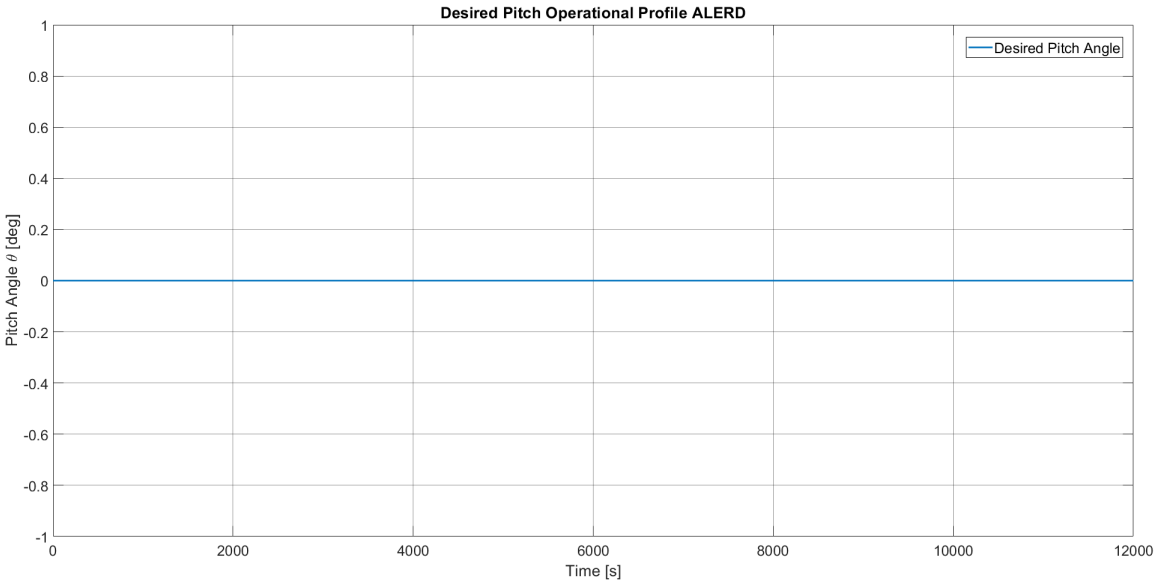

Figure 3.2: Reference signal for the pitch angle

It should be noted that Figure 3.1 and 3.2 are the control objectives based on one specific operational profile, described in Table 3.1 and [11]. Many scenarios can be created, by adding different reference signals for both the z-position and the pitch angle θ, or by including control objectives for other motions.

3.1.3. Signals for Disturbances

During the operational profile of the ALERD, disturbances due to the dredging and discharging operations will occur. For these disturbances, a time-varying signal will be created, which is used as input in the simulation model. The motion controllers are used to achieve the control objectives, defined in the previous section, while taking into account the disturbances defined in this section.

Mass Change in the Hopper

During the dredging operations, the hopper content will change from pure seawater to a mixture of dredged soil and seawater, and finally pure soil. The hopper is already discussed in Chapter 2, and is shown in Figure 2.3. The location of the hopper in the hull is schematically drawn in Figure 3.3. The hopper is symmetrically located around the center of buoyancy CB of the ALERD, leading to no additional trimming or rolling moments, since it is assumed that the center of gravity of the hopper, including the cargo mass (either water, a soil mixture, or pure soil) is located at CB of the ALERD. As already discussed in Chapter 2, the CB coincides with the center of origin (CO) of the body-fixed reference frame, which is also schematically drawn in Figure 3.3. The center of gravity of the ALERD is located below the CB, leading to $BG = 0.43$, which is the result of previous studies. This value for BG can be found in Table 2.1, and is assumed to be constant during the simulations.

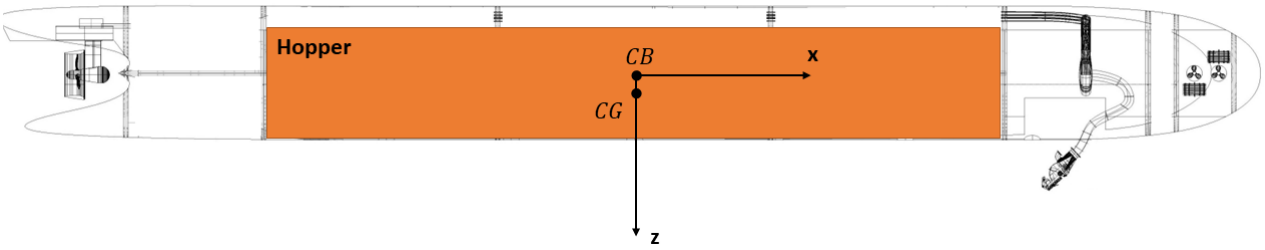

Figure 3.3: Schematic overview of the hopper location

Table 3.3: Densities

Parameter	Value	Unit
ρ_{water}	1025	kg/m^3
$\rho_{mixture}$	1900	kg/m^3

Table 3.4: Tank Mass

Parameter	Value	Unit
Hopper Mass (Water)	2419	ton
Hopper Mass (Mixture)	4484	ton
Mass Change Hopper	2065	ton
Mass Main Ballast Tank	2065	ton

The difference in density of the fluids can be found in Table 3.3. The change in weight in the hopper needs to be actively compensated if the depth and pitch are controlled. The increase in weight of the hopper, due to the higher density of the mixture, can be found in Table 3.4. The change of mass in the hopper is compensated using the main ballast tanks (MBTs). The weight of ballast water in the MBTs is equal to the weight difference in the hopper, as can be seen in Table 3.4. In Figure 3.4 and Figure 3.5, a schematic overview of the cross-section and the longitudinal section of the hull is shown, respectively. In these Figures, it is shown that the MBTs are located between the hopper and the hull. Furthermore, two other tank systems are shown, which are the depth control tank (DCT) and trim tanks (TT). These will be described in more detail in Section 3.4. Figures 3.4 and 3.5 are indicative and can be used to get an insight in the location of the tanks. The dimensions of the tanks and the hopper are not calculated and given, since these are unknown at this point and for the simulations, only the volume and the weight of the tanks and the hopper are used as input parameters. However, based

on the required hopper and tank volumes, the dimensions can be calculated. The initial dimensions of the hull (Table 2.1), in combination with the used hull form, have sufficient space for all the used tank systems from Figure 3.4 and the hopper. Therefore, it can be concluded that the used volumes for the tank systems are realistic and can all fit inside the hull of the ALERD. Since the final dimensions and the hull arrangement are not known at this point, it is chosen to not make a detailed general arrangement of the hull. The length and width of the tank systems from Figure 3.4 and Figure 3.5 are therefore illustrative and give a schematic overview. The calculation of the final required tank dimensions and arrangement is out of scope of this research, and will be done in future research.

It is assumed that during the dredging operations, water is pumped out of the tanks with the same mass flow rate and at the same time instant as the incoming soil mixture. With this assumption, the change mass of the ALERD remains zero considering the hopper mass and MBT mass, and no additional forces and moments are created due to the mass change in the hopper. Furthermore, it is assumed that the hopper is loaded symmetrically and that there are no free-surface effects in the hopper. The MBTs are schematically drawn as two tanks, located at the port- and starboard side of the hull. It is expected that, to reduce the free surface effects in the tanks, the MBTs will be divided in multiple compartments in longitudinal direction. This can also be the case for the hopper. The location of the longitudinal and transversal position of CG of the ALERD including the hopper and tank systems is assumed to be constant, as already mentioned, and both the starboard and port side MBT can be filled and emptied symmetrically. The required mass flow needed to empty the MBTs is used as input for calculating the pump power, which will be discussed in Chapter 4.

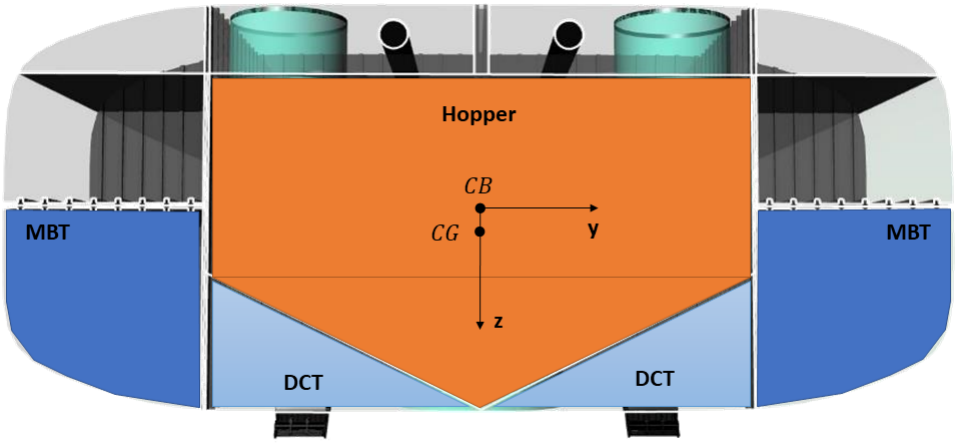

Figure 3.4: Schematic overview of the cross-section of the hull

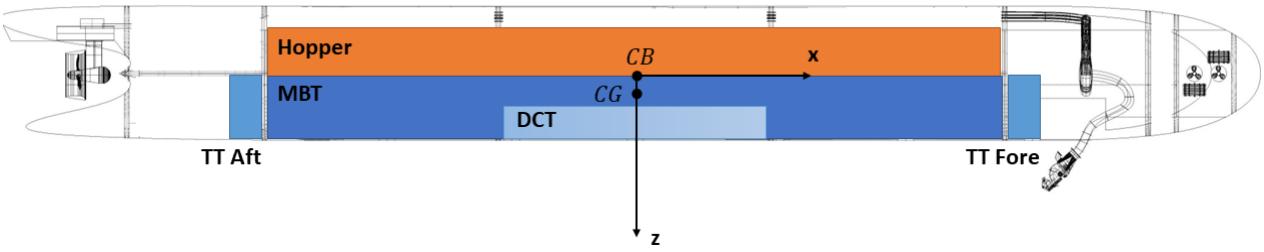

Figure 3.5: Schematic overview of the hopper and the tanks

In Figure 3.6, the change of mass in the hopper over time is shown. It can be seen that during the dredging operation, which takes 56 minutes (3360 seconds), there is a constant amount of mass added in the hopper, up to 2065 ton at the end of the operation. This corresponds to the information provided in Table 3.1 and 3.4.

The decrease of mass in the hopper is due to the discharging operation. During the discharge operation, a large amount of weight is removed from the hopper in a short amount of time, see Figure

3.6. To compensate for this loss in weight, the MBTs are filled with the same mass flow rate instantaneously. This is assumed to ensure no additional forces and moments are produced, which is a similar assumption as for the dredging operation. Filling the tanks is done by opening the flooding holes, and does not require a pump. In Table 3.1, it is shown that for conventional dredgers, the discharge operations take on average 28 minutes (1680 seconds). For the ALERD, it is assumed that the discharging operations will take about 600 seconds, which is a result of previous studies [10]. This discharge time is implemented in the reference signal generator of the simulation model and can be seen in Figure 3.1, and the change of mass in the hopper due to the discharged soil can be seen in Figure 3.6.

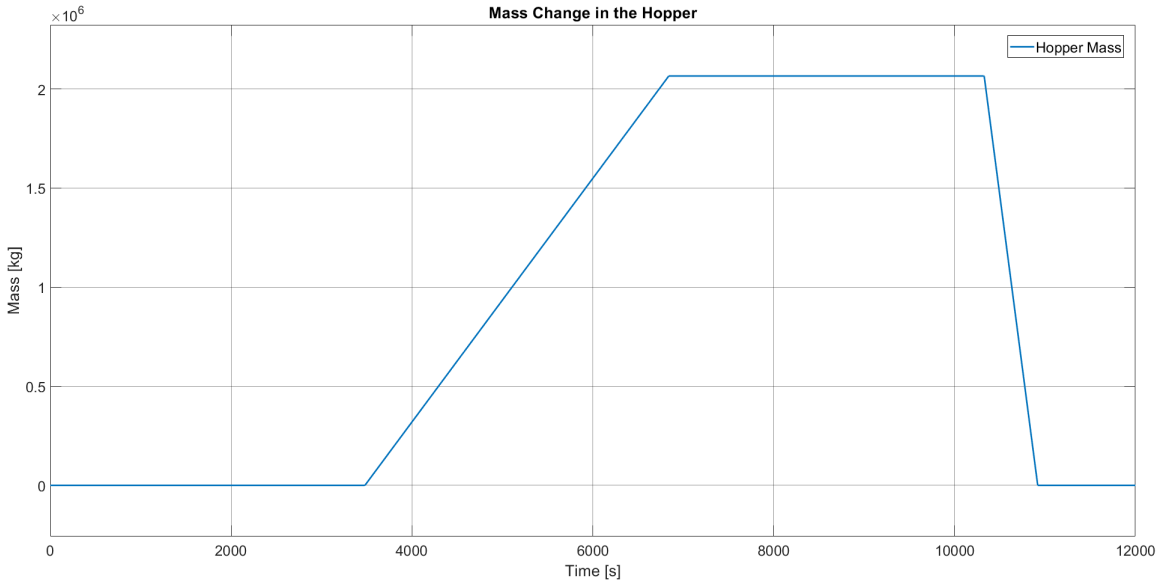

Figure 3.6: Mass change in the hopper

Draghead Trimming Moment

During the dredging operation, there is an additional trimming moment due to the draghead. In [15] the resistance of a draghead and the suction tubes is calculated for a conventional dredger. The size and amount of the used dragheads, which is two, is similar for the ALERD, and therefore it is assumed that the draghead resistance is equal. The resistance force is acting in the negative x direction. Since the suction tubes are significant shorter for the ALERD due to the low suction depth, the resistance of the suction tubes is scaled using the length ratio. The resistance of both the suction tubes and the dragheads is dependent on the forward speed and the current. The forward speed during dredging used in [15] is equal to 2 knots and assumed constant, the resistance of the two dragheads is equal to $258kN$, and the resistance of the suction tubes is equal to $2kN$. The resistance force of the two dragheads during dredging operations is shown in Figure 3.7. This total resistance of $260kN$ results in a constant trimming moment during the dredging operation, which needs to be compensated to ensure that the pitch angle remains zero. The moment arm is taken as 3.5 meters, which is the vertical distance between the seafloor and the attachment position of the suction tubes on the hull ALERD. The attachment position of the suction tubes is assumed to be 1.5 meters above the bottom of the hull, while the hull-bottom clearance during dredging is assumed to be 2 meters (see also Figure 3.1). The created moment will be in the positive direction, considering the reference frames from Figure 2.5, and therefore ballast water needs to be moved from the forward to the aft trim tank. This will be discussed in more detail in Section 3.4 and the results are given in Chapter 6.

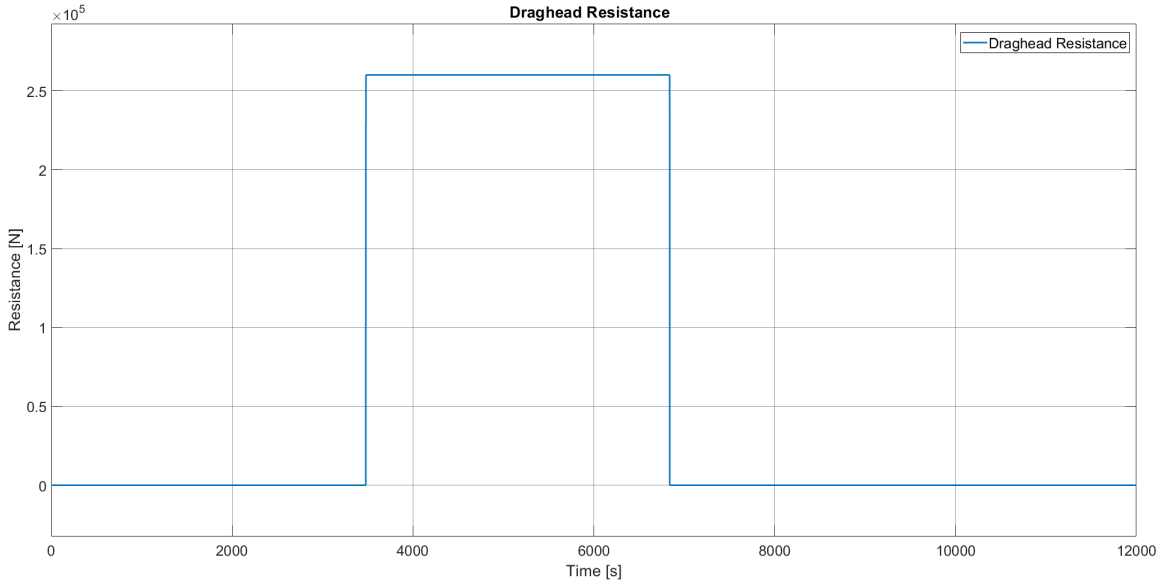

Figure 3.7: Resistance force of the draghead during dredging operations

3.2. Proportional-Integral-Derivative (PID) Control

In Section 3.1, the control objectives and disturbances due to the dredging and discharging operation are described. In order to achieve the control objectives and to take into account the time-varying disturbances, motion controllers can be used.

The first used control method in the simulation model is proportional-integral-derivative (PID) control. PID control is widely used in underwater vehicle control due to the ease of practical implementation [19] and can be used for setpoint regulation and trajectory-tracking. The PID controllers are used as benchmark controllers, in order to show the potential advantages of using more advanced control methods such as MPC for controlling underwater vehicles in different DoFs. MPC will be described in Section 3.6.2. A comparison between the motion controllers, their performance, and the results from the simulations using the different controllers will be made in Chapter 6.

A PID controller is a feedback loop controller and uses an error to determine the necessary control action in order to minimize this error. The error is calculated based on the desired setpoint and the actual state of the system. The general equation of a PID controller can be found in Equation 3.1. In this equation, K_p is the proportional controller gain, K_i is the integral controller gain, and K_d is the derivative controller gain. Furthermore, $e(t)$ is the calculated error.

$$f(t) = K_p e(t) + K_i \int_0^t e(t)dt + K_d \frac{de(t)}{dt} \tag{3.1}$$

Looking at Equation 3.1, it can be seen that the proportional gain produces an output proportional to the error. With the integral action in a PID controller, the accumulated error is calculated using the sum of the instantaneous error over time. This accumulated error is multiplied by the integral gain K_i and added to the controller input. The integral term eliminates the steady-state error caused by the proportional action, but since the integral action uses accumulated errors from the past, it can lead to an overshoot with respect to the set-point value. The derivative action calculates the time-derivative of the error and predicts the system's behavior in the future. This improves the settling time and stability of the system. To achieve the desired behavior of the controlled system, the three parameters K_p, K_i, and K_d need to be determined. This can be done using tuning rules or by using the automatic tuning function in Simulink.

The performance of the PID controller (and MPC) can be assessed using four characteristics or key performance indicators (KPIs), which are listed below.

1. Rise Time
2. Overshoot
3. Settling Time

4. Steady-state Error

The rise time is the time it takes for the controller to reach 90% of the desired level for the first time, the overshoot is defined as the maximum deviation of the actual signal with respect to the steady-state. The steady-state error is the error between the desired output and the steady-state output, and the settling time is the time it takes to reach the steady-state. Those four criteria determine the performance of the controller.

The two DoF heave (z) and pitch (θ) will have their own PID-controller. Furthermore, the forward speed u will have a PID-controller to control the forward speed based on the operational profile. The heading (ψ) can also be controlled using a heading controller. However, since the objective of the simulation model is to calculate the energy requirements for stability and buoyancy control, the focus will be on the depth and pitch controllers. The required control forces and moments, which follow from the output of the PID controllers, will be described in Section 3.4. Each DoF will have its own independent actuator to produce the required restoring forces and moments.

3.3. Model Predictive Control

Model Predictive Control (MPC) is used in the simulation model as a more advanced motion control method, to be able to compare the results from the benchmark PID controllers with, based on controller performance, constraint handling, and corresponding energy requirements. In this section, some theoretical aspects of MPC will be discussed, as well as the used linear time invariant (LTI) model, the defined cost function and the usage of the MPC toolbox in Matlab and Simulink.

In Figure 3.8, the principle of Model Predictive Control is shown. In this figure, r is the reference setpoint or trajectory, u is the manipulated variable (MV), which is used to force the measured output (MO) y towards the target set point or trajectory [24].

MPC determines the optimal output u, necessary to reach the target, by solving a constrained optimization problem. The optimal output is based on the cost function, which is defined on beforehand, taking into account constraints for the MVs. In Section 3.3.1, the principle of the cost function will be described, and the cost function used in for the MPC controller in the simulation model will be defined.

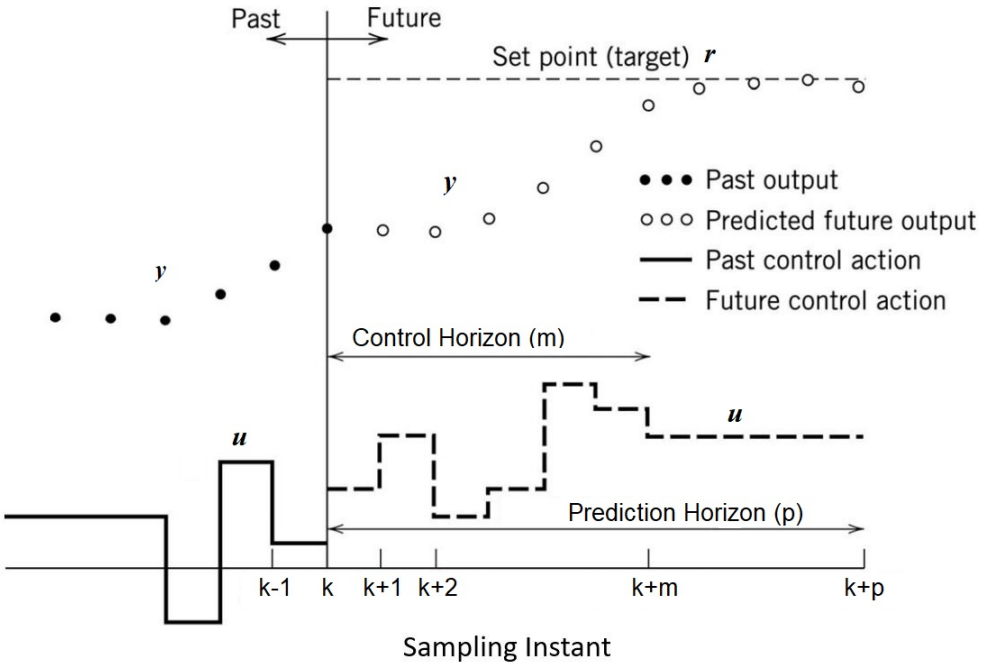

Figure 3.8: MPC principle with control and prediction horizon [31]

Prediction and Control Horizon

In Figure 3.8, the control horizon m and prediction horizon p are indicated. The prediction horizon is the time used by the controller to predict the ”future”. This prediction horizon is a manual input and can be chosen by the controller designer, and must be long enough to represent the effect of a change

in the MV u on the MO y. In Figure 3.8, it is clear to see that the set point target r is reached within the prediction horizon, and the effect of the changing manipulated variable y on the measured output variable y is clearly captured [33].

The control horizon is the section of time within the prediction horizon, where MV moves are allowed. This can also be seen in Figure 3.8. The value for the MV u is kept constant when the end of the control horizon is reached. In general, the control horizon will be chosen between $1 \leq m \leq p$.

The control horizon and prediction horizon are dependent on the system and can be modified when tuning the MPC controller with the Matlab MPC toolbox.

Sample Time

The sample time of the MPC controller must be defined as well, and does not have to be equal to the sample time of the complete simulation model [16]. In Figure 3.8, the sampling instant is plotted on the horizontal axis. k is a certain time instant, and the difference between k and $k+1$ is the sample time. The rate of change of an MV is based on the sample time.

For ships and underwater vehicles, the dynamics are in the order of seconds, while the sample time of the simulation model is 0.05 seconds. The manipulated variable (u) of the controller is the mass change in the depth control tank, which is in the order of seconds as well. It is not realistic to assume a sample time smaller than 1 second, and therefore the sampling time of the simulation model itself cannot be used. The sample time of the MPC controller can be chosen on beforehand and, if necessary, modified in the MPC toolbox from Simulink.

3.3.1. Cost Function and Constraints

In Equation 3.2, an arbitrary discrete system is defined with a state vector $\boldsymbol{x}$, input vector $\boldsymbol{u}$, and output vector $\boldsymbol{y}$. The state-space model from Equation 2.56 must be transformed to a linear-time invariant model, to be used in combination with the MPC toolbox. This will be done in the next section.

In Equation 3.3, the cost function J is defined, which is minimized by the MPC controller for the complete prediction horizon. As already mentioned, the cost function is user-defined. This cost function minimizes the tracking error between the reference vector $\boldsymbol{r}$ and model output $\boldsymbol{y}$, which can also be seen in Figure 3.8, while optimizing the output for the manipulated variable u. The cost function is subject to constraints, which can be seen in Equation 3.4. Constraints can be put on both the manipulated variable u and model output y, and their rates. The constraints for the rate of change of a manipulated variable are shown in Equation 3.5, where a minimum and maximum change of the manipulated variable for each time step can be defined. A maximum (and minimum) mass flow rate for a pump is an example of a hard constraint for the rate of change of a manipulated variable.

$$\begin{aligned} \boldsymbol{x}(\boldsymbol{k}+1) &= f(\boldsymbol{x}(\boldsymbol{k}), \boldsymbol{u}(\boldsymbol{k})) \\ \boldsymbol{y}(\boldsymbol{k}) &= \boldsymbol{h}(\boldsymbol{x}(\boldsymbol{k})) \end{aligned} \tag{3.2}$$

$$\min_{u} \quad J(\boldsymbol{x}(\boldsymbol{k}), \boldsymbol{u}(\boldsymbol{k}+i))$$

$$\min_{\boldsymbol{u}} \sum_{i=1}^{p} \|\boldsymbol{r}(\boldsymbol{k}+i \mid \boldsymbol{k}) - \boldsymbol{y}(\boldsymbol{k}+i \mid \boldsymbol{k})\| \tag{3.3}$$

subject to

$$\begin{aligned} \boldsymbol{u}_{min} \leq \boldsymbol{u}(\boldsymbol{k}+j \mid \boldsymbol{k}) \leq \boldsymbol{u}_{max} \\ \boldsymbol{y}_{min} \leq \boldsymbol{y}(\boldsymbol{k}+i \mid \boldsymbol{k}) \leq \boldsymbol{y}_{max} \\ \forall i \in \{1, \cdots, p\} \text{ and } j \in \{(1, \cdots, m\} \end{aligned} \tag{3.4}$$

$$\Delta \boldsymbol{u}_{\min} \leq \Delta \boldsymbol{u}(k+i) \leq \Delta \boldsymbol{u}_{\max} \tag{3.5}$$

Hard input constraints on the manipulated variable u and their rates represent the physical limitations of the actuators used in the model, such as the pump system and the pipelines. As can be seen in Equation 3.4, a minimum and maximum value can be determined, for which the u and y can be constrained. These hard constraints cannot be violated, since in reality it will break the physical system. Often it is chosen to constraint the rate of change of the manipulated variable u, instead of their maximum and minimum value. Furthermore, constraining the output y must be done to take into

account model limitations. For instance, if MPC control is used for depth control, the maximum output y, representing the depth, is equal to the maximum water depth.

Constraint Softening
Since the MPC controllers are used to control the depth and pitch angle of the ALERD, output constraints are necessary to ensure realistic outcomes of the simulations. Constraints can be softened using slack variables, which enable the solver to violate the constraints in order to get a feasible solution.

In Equation 3.6, the slack variable ξ is introduced. The variables W_w and W_ξ are tuning weights, representing the trade-off between the amount and duration of the constraint violation. As can be seen in Equation 3.6 and 3.7, the slack variable ξ creates an extra degree of freedom at the constraints.

$$\min_{\boldsymbol{u},\xi} \|\boldsymbol{r}(\boldsymbol{k}+i \mid \boldsymbol{k}) - \boldsymbol{y}(\boldsymbol{k}+i \mid \boldsymbol{k})\|_{W_w} + \underbrace{\|\boldsymbol{\xi}(\boldsymbol{k}+i \mid \boldsymbol{k})\|_{W_\xi}}_{\text{softening}} \tag{3.6}$$

subject to

$$\begin{aligned} &\boldsymbol{u}_{min} \leqslant \boldsymbol{u}(\boldsymbol{k}+j \mid \boldsymbol{k}) \leqslant \boldsymbol{u}_{max}, \\ &\boldsymbol{y}_{min} - \boldsymbol{\xi}(\boldsymbol{k}+i \mid \boldsymbol{k}) \leqslant \boldsymbol{y}(\boldsymbol{k}+i \mid \boldsymbol{k}) \leqslant \boldsymbol{y}_{max} + \boldsymbol{\xi}(\boldsymbol{k}+i \mid \boldsymbol{k}), \\ &\text{where } \xi \geqslant 0, \\ &\forall i \in \{1,\cdots,p\} \quad \text{and} \quad j \in \{1,\cdots,m\}. \end{aligned} \tag{3.7}$$

The slack variable ξ and tuning weights are parameters which can be used to tune the MPC controller, in order to get the requested performance.

Optimization Problem and QP solver
The MPC controller solves an optimization problem. In the next section, the MPC toolbox from Simulink and its implementation into the simulation model will be discussed. In this toolbox, a quadratic program (QP) solver is used to determine the optimal solution for the manipulated variables, used in the plant model until the next control interval.

The QP solver takes into account the cost function and the constraints, described in Section 3.3.1. The solution of the solver is the adjustment of the manipulated variable (MV) that minimizes the cost function, while satisfying the constraints [4]. The complete derivation of the QP solver, the corresponding matrices, and the optimization of the output variables is out of scope of this research. This research mainly focuses on the definition of the cost function, the constraints, and the performance of the controller in terms of reference tracking, and corresponding energy requirements. The theoretical background and derivations of the QP solver and corresponding matrices can be found in the Mathworks documentation for the MPC toolbox [4].

3.3.2. MPC Toolbox Matlab/Simulink

In Section 3.3.1, a description is given of the cost function and constraints needed for MPC controllers. In this section, the MPC toolbox from Matlab/Simulink and the variables that are used will be described. For this research, it is chosen to use the MPC toolbox, with embedded cost function and solver, to be able to compare the results from the PID controller with the MPC controller. This approach ensures that MPC can be used and implemented in the existing simulation model in Simulink, without having to design the complete MPC controller by hand. The main objective is to choose the constraints, prediction and control horizon, tuning weights, and scale factors, necessary for the controller to track the desired reference trajectory, while minimizing the corresponding energy requirements.

Linear Time-Invariant Model
The MPC toolbox from Simulink requires a linear time-invariant (LTI) model. It must be noted that, using the assumptions of low to medium speed operation, and using the diagonal matrices, the used state-space model from Equation 2.56 is (almost) completely linear, apart from some small terms in the Coriolis-centripetal matrix. Linearizing the system about $\boldsymbol{\nu} = 0$, and assuming small rotational angles for ϕ and θ, the equations of motion reduce to Equation 3.14 [7], [12].

Using the assumption of small angles for ϕ and θ, the rotational matrix from Equation 2.56 reduces to a rotation matrix only using the yaw angle ψ, as can be seen in Equations 3.8, 3.9, and 3.10. A new

position vector can be defined, using a Vessel Parallel Coordinate System and Equation 3.11. The complete derivation of Vessel Parallel coordinates can be found in [7]. In this research, they are used to generate the necessary LTI system needed for MPC control.

$$\dot{\boldsymbol{\eta}} = \boldsymbol{J}_{\Theta}(\boldsymbol{\eta})\boldsymbol{v} \approx \boldsymbol{P}(\boldsymbol{\psi})\boldsymbol{v} \tag{3.8}$$

$$\boldsymbol{P}(\psi) = \begin{bmatrix} \boldsymbol{R}(\psi) & 0 \\ 0_{3\times3} & \boldsymbol{I}_{3\times3} \end{bmatrix} \tag{3.9}$$

$$\boldsymbol{R}(\boldsymbol{\psi}) = \begin{bmatrix} \cos\psi & -\sin\psi & 0 \\ \sin\psi & \cos\psi & 0 \\ 0 & 0 & 1 \end{bmatrix} \tag{3.10}$$

$$\boldsymbol{\eta_p} = \boldsymbol{P}^{T}(\psi)\boldsymbol{\eta} \tag{3.11}$$

If low to medium speed is assumed, the yaw rate r can be assumed zero, which reduces Equation 3.11 to Equation 3.12, due to the fact that the rotation matrix $\boldsymbol{R}(\psi)$ becomes the identity matrix. The expression from Equation 3.12 has a linear relationship.

$$\dot{\boldsymbol{\eta}}_{\boldsymbol{p}} \approx \boldsymbol{v} \tag{3.12}$$

Equation 3.13 is the matrix with restoring forces and moments, which is used in Equation 3.14. Equation 3.14 are the 6 DoF linear time-invariant equations of motion, which can be written as linear time-invariant state space model. This is shown in Equation 3.15 and 3.16. The state space representation from Equation 3.16 is used as input model for the MPC controller. It must be noted that only 2 DoF will be controlled, which are the heave (z) and pitch angle (θ). However, when using Equation 2.56, it is possible to control the complete 6 DoF of an underwater vehicle.

$$\boldsymbol{G} = \mathrm{diag}\{0, 0, 0, (z_g - z_b)\,W, (z_g - z_b)\,W, 0\} \tag{3.13}$$

$$\boldsymbol{M}\dot{\boldsymbol{v}} + \boldsymbol{D}\boldsymbol{v} + \boldsymbol{G}\boldsymbol{\eta}_p = \boldsymbol{\tau} \tag{3.14}$$

$$\dot{\boldsymbol{x}} = \boldsymbol{A}\boldsymbol{x} + \boldsymbol{B}\boldsymbol{u} \tag{3.15}$$

where $\dot{\boldsymbol{x}} = \left[\dot{\boldsymbol{\eta}}_p^{\top}, \dot{\boldsymbol{v}}^{\top}\right]^{\top}$, $\boldsymbol{x} = \left[\boldsymbol{\eta}_p^{\top}, \boldsymbol{v}^{\top}\right]^{\top}$, and $\boldsymbol{u} = \boldsymbol{\tau}$.

$$\boldsymbol{A} = \begin{bmatrix} 0 & \boldsymbol{I} \\ -\boldsymbol{M}^{-1}\boldsymbol{G} & -\boldsymbol{M}^{-1}\boldsymbol{D} \end{bmatrix}, \quad \boldsymbol{B} = \begin{bmatrix} 0 \\ \boldsymbol{M}^{-1} \end{bmatrix} \tag{3.16}$$

In the above equations, the vector $\boldsymbol{\tau}$ is the vector which includes all the control forces and moments.

Cost Function and MPC Toolbox Input Parameters

The Mathworks Help Center has extended documentation with explanation of the MPC toolbox, the used variables, and the theoretical background with the used equations behind the toolbox. Exploring these equations theoretically, helps to design the MPC controller using the toolbox, and to properly choose the input parameters such as the scaling factors and weights.

$$J\,(z_k) = J_y\,(z_k) + J_u\,(z_k) + J_{\Delta u}\,(z_k) + J_{\varepsilon}\,(z_k) \tag{3.17}$$

In Equation 3.17 the cost function of the MPC controller is shown, with z_k the QP decision. The total cost function can be divided into the four cost functions, listed below.

- $J_y(z_k)$; Output reference tracking (Equation 3.18)
- $J_u(z_k)$; Manipulated variable tracking (Equation 3.19)
- $J_{\Delta u}(z_k)$; Manipulated variable move suppression (Equation 3.20)
- J_{ε}; Constraint Violation (Equation 3.21)

$$J_y(z_k) = \sum_{j=1}^{n_y} \sum_{i=1}^{p} \left\{ \frac{w_{i,j}^y}{s_j^y} \left[r_j(k+i \mid k) - y_j(k+i \mid k) \right] \right\}^2 \tag{3.18}$$

$$J_u(z_k) = \sum_{j=1}^{n_u} \sum_{i=0}^{p-1} \left\{ \frac{w_{i,j}^u}{s_j^u} \left[u_j(k+i \mid k) - u_{j,target}(k+i \mid k) \right] \right\}^2 \tag{3.19}$$

$$J_{\Delta u}(z_k) = \sum_{j=1}^{n_u} \sum_{i=0}^{p-1} \left\{ \frac{w_{i,j}^{\Delta u}}{s_j^u} \left[u_j(k+i \mid k) - u_j(k+i-1 \mid k) \right] \right\}^2 \tag{3.20}$$

$$J_\varepsilon(z_k) = \rho_\varepsilon \varepsilon_k^2 \tag{3.21}$$

In the four cost functions, the variable z_k is the QP decision, i.e. the MV adjustment that minimizes the cost function while satisfying the constraints. The QP decision can be found in Equation 3.22.

$$z_k^T = \begin{bmatrix} u(k \mid k)^T & u(k+1 \mid k)^T & \cdots & u(k+p-1 \mid k)^T & \varepsilon_k \end{bmatrix} \tag{3.22}$$

The parameters used in the cost functions, which serve as input variables for the Matlab MPC toolbox, are listed below.

- u is a manipulated variable (MV).
- Δu is the rate of a manipulated variable (MV).
- y is a measured plant output (MO).
- r is a reference setpoint or trajectory.
- n_y and n_u are the number of measured outputs (MOs) and manipulated variables (MVs), respectively.
- j is used as subscript to indicate a certain plant output, manipulated variable, or change in a manipulated variable.
- p is the prediction horizon.
- i is used as subscript to indicate a certain prediction horizon step.
- $w_{i,j}^y$, $w_{i,j}^u$ and $w_{i,j}^{\Delta u}$ are weight factors at the i^{th} prediction horizon step, for the j^{th} plant output, manipulated variable, and the rate of change of the manipulated variable, respectively.
- s_j^y and s_j^u are scale factors for the j^{th} plant output and manipulated variable, respectively.
- ρ_ε is the dimensionless constraint violation penalty weight.
- ε_k is the dimensionless slack variable at control interval k.

The scale factor s and the plant output y, as well as the reference r, have engineering units. The tuning weights w are dimensionless.

Furthermore;

- $r_j(k+i \mid k)$ is the reference value for the j^{th} plant output at the i^{th} prediction horizon step, in engineering units.
- $y_j(k+i \mid k)$ is the predicted output value for the j^{th} plant output at the i^{th} prediction horizon step, in engineering units.
- $u_j(k+i \mid k)$ is the predicted MV value for the j^{th} plant output at the i^{th} prediction horizon step, in engineering units.
- $u_{j,target}(k+i \mid k)$ is the target MV value for the j^{th} plant output at the i^{th} prediction horizon step, in engineering units.

In Equation 3.21, ρ_ε is the dimensionless constraint violation penalty weight, and ε_k is the slack variable. Note that the notation can somewhat differ from the notation in Section 3.3.1, but the function of the variables remains the same. All the variables defined above can be used to tune the MPC controller in the MPC toolbox from Simulink. The information above is provided in the Mathworks help center for the MPC toolbox [4].

3.4. Control Forces and Moments

In this section, the control forces and moments, which are determined by the used motion controller, are described. The control forces and moments are the input for the force vector $\boldsymbol{\tau}$ in the state-space representation from Equation 2.56. Since the motions are decoupled, each DoF will be controlled using its own dedicated control force or moment.

3.4.1. Depth Control

In general, underwater vehicles change their depth using ballast water tanks. For the ALERD concept, the main ballast tank is used to compensate for the change of weight in the hopper, which is already described in Section 3.1.3. The control objective for the depth in z direction is based on the operational profile of the ALERD, and is shown in Figure 3.1. To create or lose additional weight, required for changing the depth of the ALERD, depth control tanks (DCTs) will be used. The required amount of weight that needs to be added from or removed to the tanks, m_{DCT}, is used as variable for the motion controllers, to control the depth z. The required output (m_{DCT}), determined by the motion controllers, is translated into a heave force and is used as input in the force vector $\boldsymbol{\tau}$ in the state-space model (Chapter 2). It is assumed that the DCTs are positioned in such a way that they do not create additional trimming moments, so adding or removing weight only creates additional forces in heave motion. Furthermore, it is assumed that the center of gravity of the ALERD does not change, meaning the value for BG will remain constant. By adding or removing mass from the DCT, negative, as well as positive forces can be generated. Negative forces are necessary to let underwater vehicles rise, due to the fact that the $W < B$ is required for rising. Negative forces can also be used to slow down descending maneuvers. In Equation 3.23, the heave force due to the mass in the DCT can be found. If mass is added to the DCT, i.e. $m_{DCT} > 0$, the heave force will have a positive sign, which is a downward force sending the ALERD down.

$$F_{DCT} = g \cdot m_{DCT} \tag{3.23}$$

3.4.2. Pitch Control

The pitch angle θ is also controlled using a motion controller. Due to the symmetry assumptions, and the low to medium speed operations, the pitch and heave motion are only slightly interacting. For underwater vehicles, the pitch can be controlled in different ways using trim tanks or stern-planes. In the simulation model, both options are available, and both will be described below. As already mentioned above, the control objective is to keep the pitch angle θ at zero degrees at all times, which is also shown in Figure 3.2.

Stern-Planes

Stern-planes are a way of controlling the combined depth and pitch motions of underwater vehicles. They are often applied on smaller AUVs to execute diving maneuvers. Stern-planes are able to deliver a vertical lift force in z-direction. They also generate an additional drag force in the forward (x) direction, which need to be compensated with additional propulsive power. The lift force can be used for changing the depth and pitch of the underwater vehicle. The generated lift is dependent on the speed of the underwater vehicle and the angle of attack of the planes.

If stern-planes are used, the output variable of the used motion controller for controlling both the pitch angle and the depth is the angle of attack of the stern-planes (δ_s). The angle of attack (δ_s) in combination with the speed of the underwater vehicle determines the magnitude of the generated lift force and the generated drag, which are shown in Equation 3.24 and 3.25. The lift coefficient C_L is linearly dependent with the angle of attack δ_s, and the drag coefficient C_D is also dependent (but not linearly) on δ_s. Furthermore, A is the stern-plane area and u is the forward speed. The stern-planes are often strategically positioned along the hull, and therefore generate an additional trimming moment, which can be seen in Equation 3.26. In this equation, x_{sp} is the x-location of the stern-planes, with respect to CB.

$$L_{sp} = \frac{1}{2} C_L \rho u^2 A \tag{3.24}$$

$$D_{sp} = \frac{1}{2} C_D \rho u^2 A \tag{3.25}$$

$$M_{sp} = x_{sp} \cdot L \tag{3.26}$$

In [27] transition algorithms are developed which can switch between vertical tunnel thrusters and bow- and stern-planes to control the combined pitch and depth motions. For the ALERD, it is possible to switch between the stern-planes, and for instance a trim tank system or vertical thrusters. To be able to do this, an optimal transition speed must be determined in order to optimize the energy consumption for pitch and depth control. Using the assumptions that the ALERD is operating at low to medium speed, that zero pitch must be maintained at all times, and that calculating an optimal transition speed and transition algorithm is out of the scope of this report, it is chosen to not use the stern-planes for pitch and depth control. Stern-planes are particular useful at higher speeds, where the heave and pitch motions are highly coupled, which is not the case for the ALERD.

Trim Tank System

In the previous section, it is concluded that stern-planes will not be used in the simulation model as actuator for controlling the pitch. Similar as for navy submarines, it is chosen to use a trim tank system for controlling the pitch instead. The trim tank system for the ALERD is a closed system consisting of two connected tanks. It is assumed that the two tanks are located 30 meters fore and aft with respect to the center of origin (CO) in longitudinal direction, indicated with $x_{TT,fore}$ and $x_{TT,aft}$. Due to the symmetrical positioning of the tanks, no additional trimming moments are produced, in both pitch and roll direction. The arrangement of the trim tanks will be described in more detail in Section 3.4.3.

The trim tanks can be used to create required restoring moments for controlling zero pitch at all times. The variable that can be used by the motion controllers to control the pitch angle is $m_{TT,fore}$, which is the mass that needs to be added to, or removed from, the forward trim tank. $m_{TT,fore}$ is translated into a trimming moment, and used as input in the forces and moments vector $\boldsymbol{\tau}$ from the state-space representation in Equation 2.56. The trimming moments, created by the trim tank system, can be found in Equation 3.27. The trim tank system is modelled in such a way, that adding mass to the forward tanks means that the same amount of mass is removed from the aft tank, ensuring the total mass in the trim tanks ($m_{TT,tot}$) remains constant at all times. Using the trim tanks does not change the weight of the ALERD, since it is a closed system and no additional weight is added or removed.

$$\begin{aligned} M_{TT,fore} &= g \cdot x_{TT,fore} \cdot \left(\frac{m_{TT,tot}}{2} + m_{TT,fore}\right) \\ M_{TT,aft} &= g \cdot x_{TT,aft} \cdot \left(\frac{m_{TT,tot}}{2} - m_{TT,fore}\right) \end{aligned} \tag{3.27}$$

3.4.3. Tank Arrangement

In the previous sections, the control forces and moments are described. In these sections, it is concluded that depth control will be done using the DCT, which can create a heave force. Pitch control is done using two trim tanks, located forward and aft in the hull. In Figure 3.9, the arrangement of these tanks is shown, as well as the MBT, used for compensating the change of weight in the hopper. The MBT is described in more detail in Section 3.1.3. It must be noted that Figure 3.9 is purely schematic, giving an overview of the position of the tanks. Similar as for the MBTs, the dimensions of the DCT and TTs are not determined in this research. The main parameters for the tanks, which are used as input for the simulation and which are the output of the motion controllers, are the required mass in the tanks, necessary to create the restoring forces and moments. Furthermore, for the trim tank system, the distances $x_{TT,fore}$ and $x_{TT,aft}$ are used as input to calculate the trimming moment. The location of the trim tanks is symmetrical positioned with respect to CB, with a large distance to enable them to create a large restoring trimming moment while using a minimum volume of ballast water.

The DCT is located as low as possible in the hull, which is beneficial for the value BG. This value must always be positive, to ensure positive stability for an underwater vehicle such as the ALERD. It is assumed that the distance between CB and CG is constant, i.e. the value of $BG = 0.43$ remains constant. Due to the longitudinal position of the DCT, the position of the longitudinal center of gravity will not change when the DCT is filled or emptied.

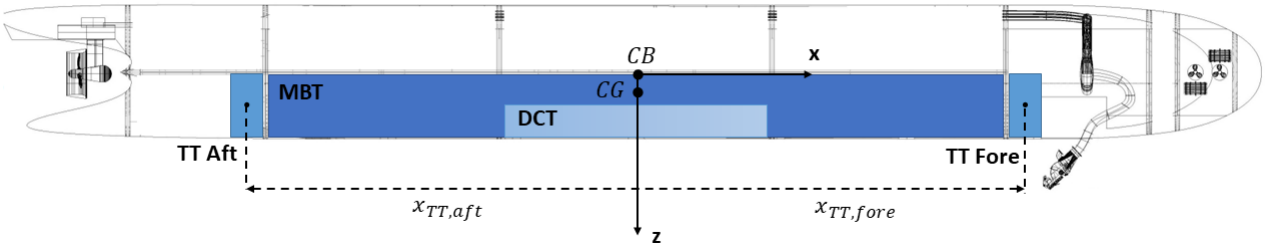

Figure 3.9: Schematic overview of the tank arrangement

In Table 3.5, the main parameters for the TTs are given. The total mass of water inside the tanks is assumed to be 10000 kg. In the initial condition, this mass is equally divided between the two tanks. The distances of the center of gravity of the tanks with respect to the center of origin of the ALERD are given as well, and are equal to 30 meters, as already mentioned in the previous section. The trim tank system is parametrically modelled, and the parameters can be changed in the simulation model if necessary. In Section 3.1.3, an overview of the cross-section of the hull, including the DCT and MBT, but without the TTs, can be found. In the cross-section of the hull, the trim tanks are placed in such a way that they do not generate additional rolling moments.

Table 3.5: Parameters trim tank system

Parameter	Value	Unit
$x_{TT,aft}$	30	m
$x_{TT,fore}$	30	m
$m_{TT,tot}$	10000	kg

3.4.4. Speed Controller

The speed of conventional dredgers changes during the operational cycle, as indicated in Table 3.1. The same counts for the ALERD, for which the speed profile can be found in Table 3.2. To obtain realistic simulations taking into account this speed profile, a speed controller is used to control the speed of the ALERD. The motions in the 6 DoF are almost completely decoupled, but the linear damping matrix is multiplied with the speed and the Coriolis-centripetal matrix is speed dependent. Therefore, the speed has an influence on the outcomes of the simulation model.

Important to note is that the speed controller is only used to make the simulations more realistic, taking into account physical constraints for the propeller speed, and taking into account ship dynamics. Another way of implementing a time-varying speed is to use a reference generator with the different speeds of the complete operational profile, and use this as direct input for the simulation model. However, it is chosen to use motion controllers instead.

The control input for the actuator, which are the propellers, is the propeller speed n, which produces a force in x-direction. By controlling the propeller speed, the forward speed of the ALERD is controlled as well.

The propeller speed n is the controller output, which is used as input for the main function ALERD.m. In this function, the corresponding propulsion force in x direction is calculated using the propeller characteristics, and Equation 3.28. The propeller thrust from Equation 3.28 is used in the force vector $\boldsymbol{\tau}$ in the state space representation from Equation 2.56. From previous studies ([8]), the propeller characteristics from Table 3.6 are determined, necessary to calculate the propeller thrust and torque. The initial number of propellers is two. This is implemented into the simulation model as well. The propeller torque can generate a rolling moment, but since two counter rotating propellers are used, it is assumed that this generated moment is negligible.

$$T = 0.5 \cdot \rho \cdot D_{prop}^4 \cdot K_T \cdot n^2 \tag{3.28}$$

$$Q = 0.5 \cdot \rho \cdot D_{prop}^5 \cdot K_Q \cdot n^2 \tag{3.29}$$

Table 3.6: Propeller characteristics

Wageningen B3-65 nozzle 19A	
D_{prop}	2.8 [m]
K_T	0.207 [-]
K_Q	0.0297 [-]
# of propellers	2

As mentioned before, the speed controller is only used to generate a realistic time-varying speed profile, based on the speed characteristics for the different operational modes. The required energy for the propulsion system, in combination with the used propeller and output of the motion controller, is not assessed in this research, since it does not contribute to the energy requirements for stability and buoyancy control.

3.5. Constraints

3.5.1. Physical Constraints for Depth and Pitch Control

To make a realistic simulation model using motion controllers, actuator limits must be implemented. Physical constraints are necessary, since for the PID-controller, the automatic tuning function from Simulink determines the three tuning parameters for the controllers without taking into account physical limitations of the used actuators and systems, such as pumps or propellers. The MPC toolbox from Matlab is also able of using physical constraints.

The constraints for the heave and pitch controllers are defined based on the physical limitations of the pipe-flow system and pumps, which are the physical systems used, and which are in more detail described in Chapter 4. These systems have several physical limitations, such as the maximum volume flow rate which a pump can handle, and a maximum allowed flow velocity in pipelines onboard ships. It is assumed that, since centrifugal pumps are capable of delivering high volume flows, the velocity of the seawater in the pipelines is the limiting factor. The flow velocity is dependent on the pipe diameter and the volume flow rate, as can be found in Equation 3.30.

$$v = \frac{\dot{V}_{pump}}{\frac{\pi}{4} \cdot d_{pipe}^2} \tag{3.30}$$

The pipe diameter is another physical limitation, since the space onboard the ALERD is not infinite and realistic values must be assumed. The maximum allowable flow velocity for a given pipe diameter is provided by C-Job. The maximum flow velocity combined with the pipe diameter can be used to calculate the maximum allowable volume flow rate, using Equation 3.30. The maximum allowable volume flow rate can be rewritten in terms of mass flow rate using the density of seawater, which is the output of the motion controllers. The maximum values with corresponding pipe diameter can be found in Table 3.7. It must be noted that for reading purposes, the numbers are rounded. The maximum mass flow rates are used to constrain the motion controllers for both the depth and pitch angle.

Table 3.7: Physical Constraints Pipes

Pipe Diameter [m]	**Maximum Flow Velocity [m/s]**	**Mass Flow Rate [kg/s]**
0.20	2.52	81
0.23	2.61	106
0.25	2.69	135
0.30	2.85	207
0.35	3.02	298
0.40	3.18	410
0.45	3.35	546
0.50	3.51	707
0.55	3.68	896
0.60	3.84	1114
0.65	4.01	1364
0.70	4.17	1647

3.5.2. Physical Constraints for Speed Control

To generate a realistic and time-varying speed, controller constraints must be implemented for the speed controller. Since the output of the PID controller for the speed is the propeller speed n, upper and lower limits are applied. It is assumed that the maximum propeller speed is 260 rpm, based on the propeller characteristics. The minimum propeller speed is assumed to be 0 rpm. A detailed description and derivation of the propeller constraints are out of scope of this research, and therefore, constraints for physical systems needed to deliver the propeller speed, such as (electrical) engines, are not taken into account as well.

Since the main control objectives of this research are depth and pitch control and the corresponding energy requirements, a detailed description of the constraints for these two controllers is made in the next section.

3.5.3. Controller Constraints

The controller constraints, in terms of overshoot, speed, and settling time, are based on the real life operations of the ALERD, corresponding to the operational profile. For instance, while descending to dredging depth, an overshoot of the reference depth reduces the hull-bottom clearance between the ALERD and the seafloor. Therefore, one of the controller constraints is a maximum allowable overshoot. A large settling time is also unfavorable and unrealistic in real life. If the dredging operations must take place with a minimum hull-bottom clearance, and it takes too long to reach this depth due to a large settling time, the operations cannot be carried out sufficiently.

Hard constraints for the controller are therefore based on the operational profile of underwater vehicles and real life operations. It is chosen to assume a maximum allowable overshoot of 0.5 meters, and a maximum allowable settling time of 5 minutes (300 seconds). These hard constraints are chosen arbitrarily, but based on safety and operational considerations.

3.6. Controller Design

Using the defined control objectives, the control forces and moments, and the constraints, the controllers can be designed accordingly. In the upcoming sections, both the PID controller design and the MPC controller design will be described.

The motion controllers, used to control the depth and pitch angle of the ALERD, have multiple objectives. From a practical point of view, the objectives during the reference tracking of the depth and pitch of an underwater vehicle used for dredging, can be defined as follows;

- Safe operations for the entire operational profile.
- Close reference tracking of the desired depth and pitch, for the entire operational profile.
- Physical constraints of the used actuators, such as the pumps, pipe-flow systems, and the propeller.
- Minimizing the energy consumption, required for the reference tracking.

3.6.1. PID Control Design for the ALERD

For PID control, the controller design is relatively straight-forward. Each DoF that is controlled with a PID controller has its own dedicated controller. For each DoF, the tuning parameters or controller gains K_p, K_i, and K_d must be chosen. This can be done using PID tuning-rules, or by using the automatic tuning from Simulink. For the automatic tuning function, Simulink linearizes the plant model, which in this case is the state-space representation from Equation 2.56, and determines the three tuning parameters while balancing the performance and robustness of the controller [3].

The results of the automatically tuned PID controller can be found in Chapter 6. The physical constraints, defined in Section 3.5.1, are incorporated in the simulation model using a Simulink block that limits the rate of change of a variable, or by limiting the minimum and maximum output using a saturation block.

3.6.2. MPC Design for the ALERD

As already described in Section 3.3, the MPC toolbox from Matlab is used to design the MPC controller. The objectives for the controller, defined above, can be incorporated into the cost function. Save operations and close reference tracking are closely related to each other. Insufficient controller behavior, such as large overshoots, or slow response, will lead in reality to unsafe situations, such as a small

hull-bottom clearance during the dredging operation. The physical constraints can be implemented in the MPC toolbox, by using both hard and soft constraints on the output of the manipulated variables, as well as on the rate of change of the manipulated variables. Minimizing the energy consumption is directly coupled with minimizing the control actions, needed for the reference tracking. All the required input variables for the Matlab MPC toolbox, described in the previous section, will be given below.

Input and Output Specifications

In Table 3.8, the plant inputs and outputs are defined, as well as their nominal value and scale factor. Note that the notation of the scale factor corresponds to the notation in the previous section. As can be seen, there are three plant inputs, from which two are manipulated variables and one is a measured disturbance. The two manipulated variables (MVs) are the mass in the depth control tank and trim tanks respectively, which is similar as the output from the two PID controllers. The last model input is the measured disturbance (MD), which is the draghead resistance. This resistance leads to a positive trimming moment, directly affecting the pitch angle, and must therefore be included in the MPC controller as MD. The two plant outputs (MOs) are the depth (z) and pitch angle (θ). Each MO has its own dedicated MV, since the depth is controlled using the mass in the DCT, and the pitch angle is controlled using the mass in the trim tanks.

As can be seen in Table 3.8, the nominal values are all set to zero. The nominal value for an MV is the target value, used in the cost function for the MVs, which is also shown in Equation 3.19. Since the main objectives are reference tracking and energy optimization for the ALERD, the MVs do not have a specific target, and the cost function for MV tracking (Equation 3.19) is not used in the complete cost function.

The nominal values, as well as the scale factors, are given in engineering units. The corresponding units can be found in Table 3.8 as well. The scale factor of the MVs, MD, and MOs must be set equal to their range, if the range is known or given. For instance, the minimum and maximum values for the mass in the DCT is chosen to be $+-1500kg$, which is based on the results from the PID controllers. The scale factor, which is the maximum range, is therefore set to $3000kg$. The same applies to the trim tank mass, draghead resistance, and the range for the depth and pitch angle. The depth range is between 0 and 25 meters, which is considered to be the maximum water depth. For the pitch angle, the control objective is to have a zero pitch angle for the complete operational profile. To have a valid QP decision from the MPC controller, it is chosen to define a small range for the pitch angle, between -0.002 and 0.002 rad, leading to a range of 0.004 rad. Setting these values to zero leads to an unstable controller in practice.

Table 3.8: MPC Input and Output Specifications

Plant Inputs	j	**Channel**	**Type**	**Name**	**Unit**	**Nominal Value**	**Scale Factor** s_j^u
	1	u(1)	MV	Mass DCT	kg	0	3000
	2	u(2)	MV	Mass TT	kg	0	4000
	3	u(3)	MD	Draghead Resistance	N	0	260000
Plant Outputs	j	**Channel**	**Type**	**Name**	**Unit**	**Nominal Value**	**Scale Factor** s_j^y
	1	y(1)	MO	Depth	m	0	25
	2	y(2)	MO	Pitch	rad	0	0.004

Constraints and Weights

In Table 3.9, the minima and maxima for the MVs, the MOs, and the MV rates, can be found. Similar as for the PID controllers, the hard constraints are based on the maximum flow velocities in the pipe, with the corresponding maximum and minimum mass flow rate. In Table 3.10, the hard and soft constraints for the MVs and MOs are indicated. A hard constraint is indicated with 0, while constraint softening can be done with values > 0. Hard constraints may not be violated by the QP solution, while constraint softening can ensure the QP solver has a feasible solution. As mentioned before, the change in manipulated variable (i.e. the mass flow rate) has a hard constraint, due to the physical limitations of the system.

Listed below are some values which can be used to soften the constraints, varying from hard to very soft, according to the Mathworks MPC Toolbox documentation [4]. As can be seen in Table 3.9,

the minimum and maximum values for the MVs and MOs, are all constrained with average softness (1). The QP solver is therefore allowed to violate these soft constraints, if necessary.

- 0 - No violation allowed (hard constraint)
- 0.05 - Very small violation allowed (nearly hard)
- 0.2 - Small violation allowed (quite hard)
- 1 - Average softness
- 5 - Greater-than-average violation allowed (quite soft)
- 20 - Large violation allowed (very soft)

Table 3.9: Input and Output Constraints on MVs and MOs

Input and Output Constraints						
Plant Inputs	**Channel**	**Type**	**Min**	**Max**	**RateMin**	**RateMax**
	u(1)	MV	-1500 $[kg]$	1500 $[kg]$	-81 $[kg/s]$	81 $[kg/s]$
	u(2)	MV	-2000 $[kg]$	2000 $[kg]$	-410 $[kg/s]$	410 $[kg/s]$
Plant Outputs	y(1)	MO	0 $[m]$	25 $[m]$		
	y(2)	MO	-0.002 $[rad]$	0.002 $[rad]$		

Table 3.10: Hard and soft contraints for MVs and MOs

Equal Constraint Relaxation (ECR)						
Plant Inputs	**Channel**	**Type**	**MinECR**	**MaxECR**	**RateMinECR**	**RateMaxECR**
	u(1)	MV	1	1	0	0
	u(2)	MV	1	1	0	0
Plant Outputs	y(1)	MO	1	1		
	y(2)	MO	1	1		

In Table 3.11, the dimensionless weights are given for the MVs, MV rates, and MOs. As already discussed, there is no MV target. Therefore, the weights for the MVs are set to zero, and the cost function from Equation 3.19 for MV tracking is not used. This is also the default setting of the toolbox, if there are no targets for the MVs [4]. For the tuning weights, the Mathworks documentation gives the following guidelines, listed below.

- 0.05 - Low priority, large tracking error acceptable
- 0.2 - Below-average priority
- 1 - Average priority - the default
- 5 - Above average priority
- 20 - High priority, small tracking error desired

For controlling the depth, the MV and MO weights are set to 1, which is the default value, leading to an equal and average priority for both tracking the MV rates and OV. The results from the MPC controller are described in Chapter 6, and there it is shown that these weights, in combination with the chosen constraints, lead to sufficient performance for the depth reference tracking, in terms of controller performance and energy consumption.

The weights used for controlling the pitch are adjusted. The rate weight $w_{i,2}^{\Delta_u}$ is set to 1000, which is quite high. This weight is used to penalize for aggressive control moves. Since the reference pitch signal is very small, minimizing the tracking error, in combination with the disturbance due to the drag-head, can lead to very aggressive control moves, required for keeping the tracking error as small as possible. Those aggressive control moves lead to a relatively high energy consumption. Therefore, it is chosen to prioritize energy consumption (i.e. less aggressive control moves) over minimizing the tracking error. The weight $w_{i,2}^{y}$ is therefore set to 10. A downside from using the MPC toolbox from Matlab, is that again a lot of manual input and tuning is required. Manual tuning of different parameters always leads to a trade-off between different KPIs, such as the controller KPIs and the energy consumption. This is also the case when using the PID controllers.

Table 3.11: Specified Weights for MVs and OVs

Input Weights (dimensionless)	**Channel**	**Type**	**Weight** $w_{i,j}^{u}$	**Rate Weight** $w_{i,j}^{\Delta u}$	**Target**
	u(1)	MV	0	1	nominal
	u(2)	MV	0	1000	nominal
Output Weights (dimensionless)	**Channel**	**Type**	**Weight** $w_{i,j}^{y}$		
	y(1)	MO	1		
	y(2)	MO	10		

The remaining manual input parameters for the MPC toolbox can be found in Table 3.12. The prediction horizon is chosen based on the output response for a realistic scenario in the MPC toolbox, which can also be seen in Figure 3.11. In this figure, a scenario is created (dark gray line) which is representable for the reference tracking during the time domain simulation. The internal plant is created by the MPC toolbox using the linear time-invariant state-space representation. For the depth output, a step in z-direction of 0.1 meters in 1 second is a realistic scenario, since it is assumed that the maximum vertical speed for the ALERD is $0.1m/s$. For the pitch angle, the created scenario is equal to the reference signal, which is a pitch angle of zero at all times. It can be seen that a prediction horizon of 150 seconds is sufficient, to capture the result of a change in MV on the MO.

From Figure 3.11, it is also clear to see that the MD from Figure 3.10 (draghead resistance, leading to a trimming moment), has a direct result on the pitch angle. Although the trim mass is changed by the controller to counteract this MD, a small pitch angle occurs, which can be considered negligible. More aggressive control actions can lead to potential smaller pitch angles, but can increase the required energy significantly. According to Figure 3.11, the pitch angle is $\approx 0.003rad$, which is $\approx 0.2^{o}$.

The control horizon is chosen to be significantly smaller compared to the prediction horizon, but large enough to ensure sufficient controller performance, while keeping the computational time low. In Chapter 6, it can be seen that the internal plant input and output response are a good representation and work sufficiently for the complete time-domain simulation, tracking the reference depth and pitch angle, and taking into account the disturbance of the draghead. The behavior of the inputs (MVs and MD) and outputs (MO) from Figure 3.10 and 3.11 show similar behavior when tracking the complete reference signals for the depth and pitch angle.

Since the dynamics of ballast water pumps and ships in general are in the order of seconds, it is chosen to have a controller sample time of $T_s = 1$.

The final results of using the MPC controller for depth and pitch control, using the defined optimization problem above, can be found in Chapter 6. In that chapter, a comparison with the PID controllers will be made as well, taking into account the controller performance and the corresponding energy requirements.

Table 3.12: Remaining Input Parameters for MPC toolbox

Parameter	**Name**	**Value**	**Unit**
p	Prediction Horizon	150	s
m	Control Horizon	25	s
T_s	Controller Sample Time	1	s

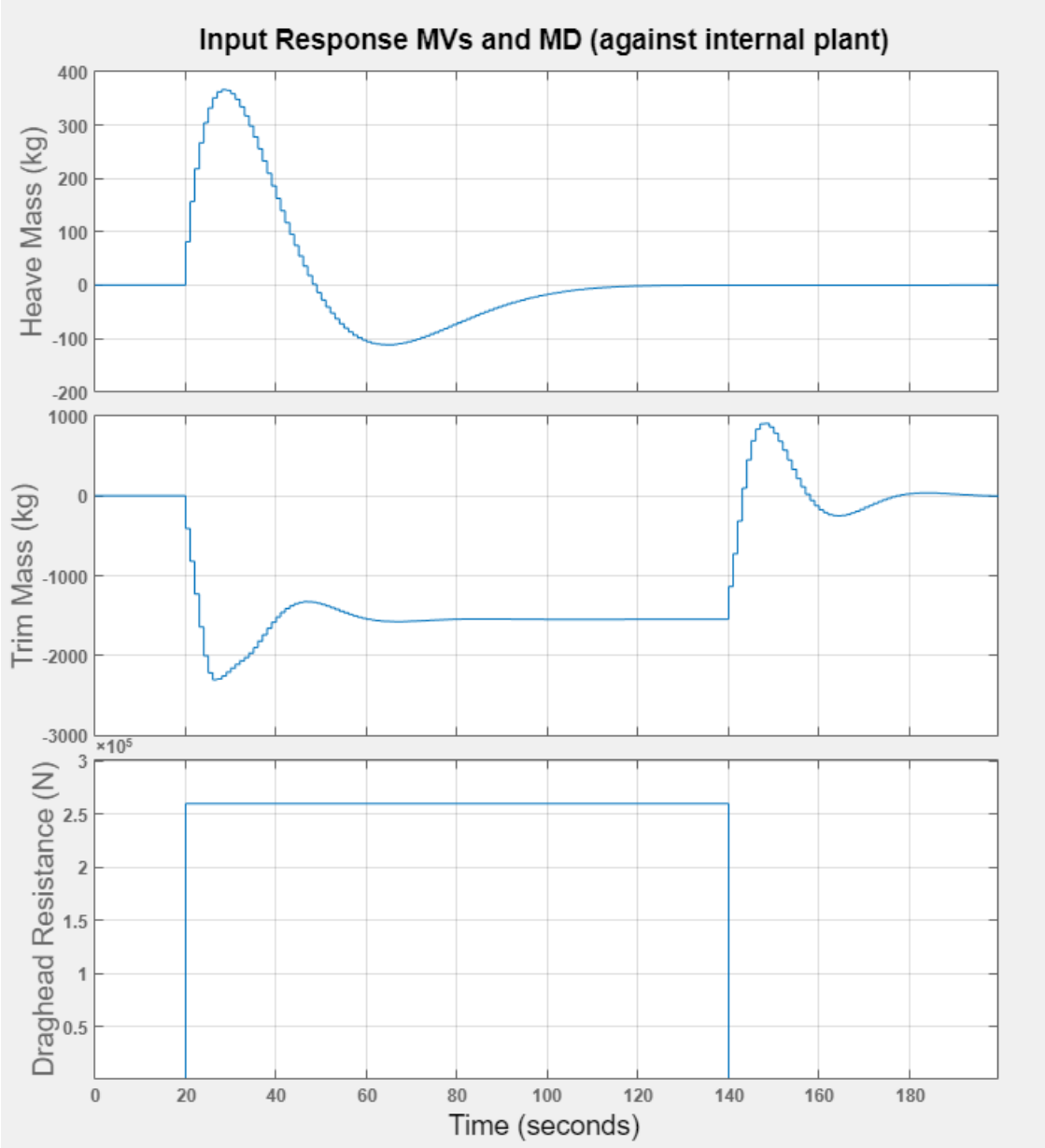

Figure 3.10: Overview of the MPC toolbox interface with input response from MVs and MD

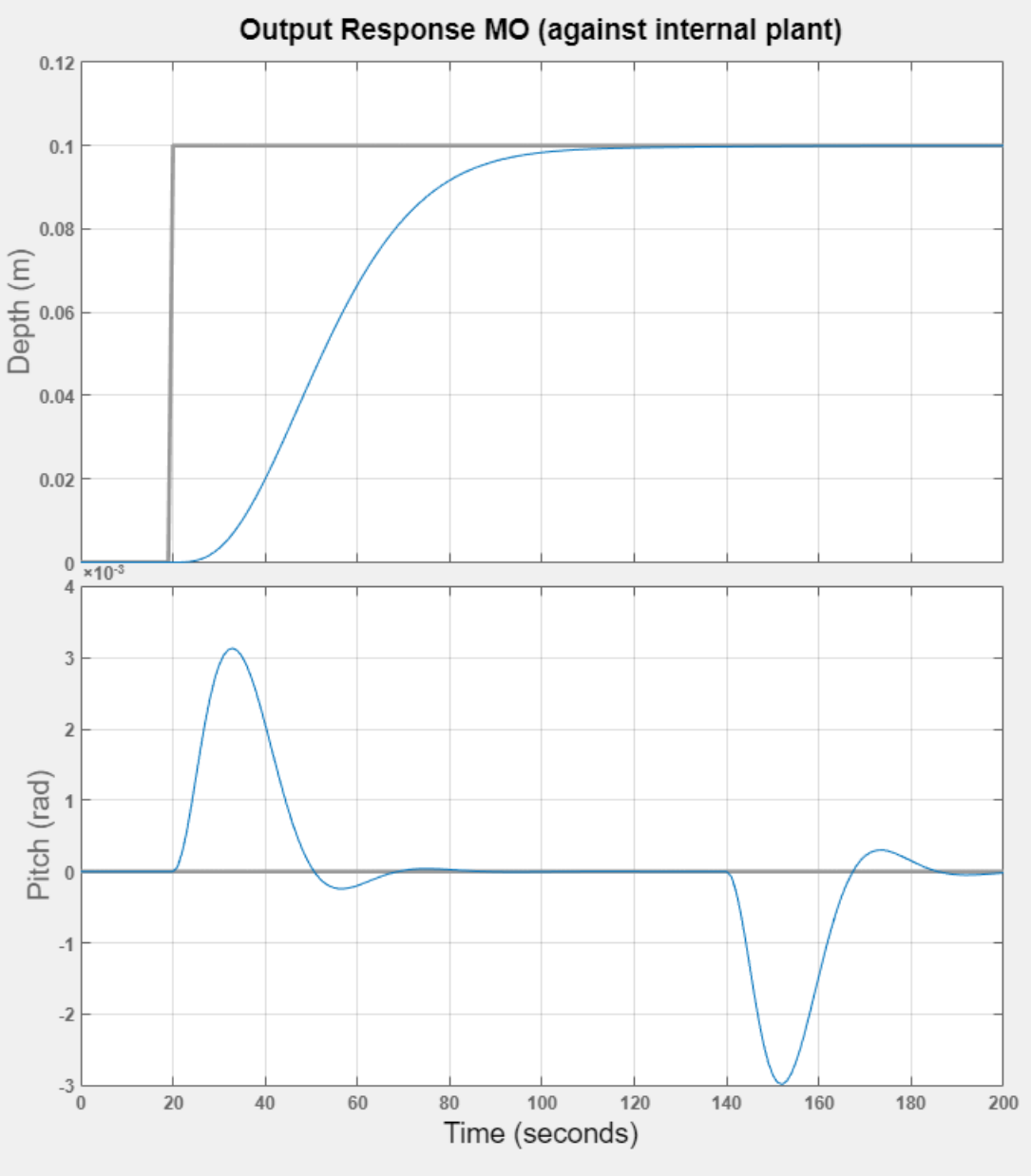

Figure 3.11: Overview of the MPC toolbox interface with output response from MOs

4

Energy Assessment

In this chapter, the required control forces and moments to achieve the control objectives, defined in Chapter 3, are translated into the required power and corresponding energy consumption. This is done by using equations for the actual physical systems. For the ballast tank system, two different systems are compared, which are the ballast water pump and a compressed air system. The required energy for achieving the control objectives for depth and pitch control will in the end contribute to the assessment of the ALERD as a cost-effective solution for coastal replenishment along the Dutch coast-line.

4.1. Ballast Water Pumps

The required mass flow for the ballast tanks, used for depth- and pitch control, and to compensate the weight in the hopper, can be used to calculate the required pump power and corresponding energy consumption. The required additional water mass that needs to be added to or removed from the tank is the output from the used controller for depth and pitch control (see Chapter 3). When the tanks need to be emptied, pumps are used, and if they need to be filled, flooding holes are opened. Therefore, only the negative mass flow (i.e. water removed from the tanks) is taken into account when calculating the pump power.

To calculate the engine power to drive the pump, Equation 4.1 can be used, with $\dot{V}_{pump}$ the volume flow in m^3/s and η_{pump} the pump efficiency [32]. Values for the pump efficiency for centrifugal pumps vary between 0.6 - 0.9 and are dependent on the pressure head, according to [32].

$$P_{B,pump} = \frac{\dot{V}_{pump} \cdot \Delta p^{++}_{pump}}{\eta_{pump}} \tag{4.1}$$

The volume flow for the tanks is calculated in Simulink using the output from the motion controllers. The output is the amount of mass that needs to be added or removed from the tanks at each time step during the simulation. Taking the time-derivative of this mass at each time step gives the required mass flow ($\dot{m}$) at each time step. The mass flow can be translated into volume flow and used in Equation 4.1.

Δp^{++}_{pump} is defined in [32] as the total pressure head, which includes the static pressure head, the dynamic pressure head, and the head caused by a height difference in the pipe-flow system itself. The total pressure head can be calculated using Equation 4.2. In this equation, the system pressure impedance is calculated using the Bernoulli equation for the pressure and suction line. The system impedance is the load as experienced by the pump. Using the Bernoulli equation, the pump pressure rise must be equal to the system impedance, which can be seen in Equation 4.4. A schematic overview of the pipeline system including the pump can be found in Figure 4.1.

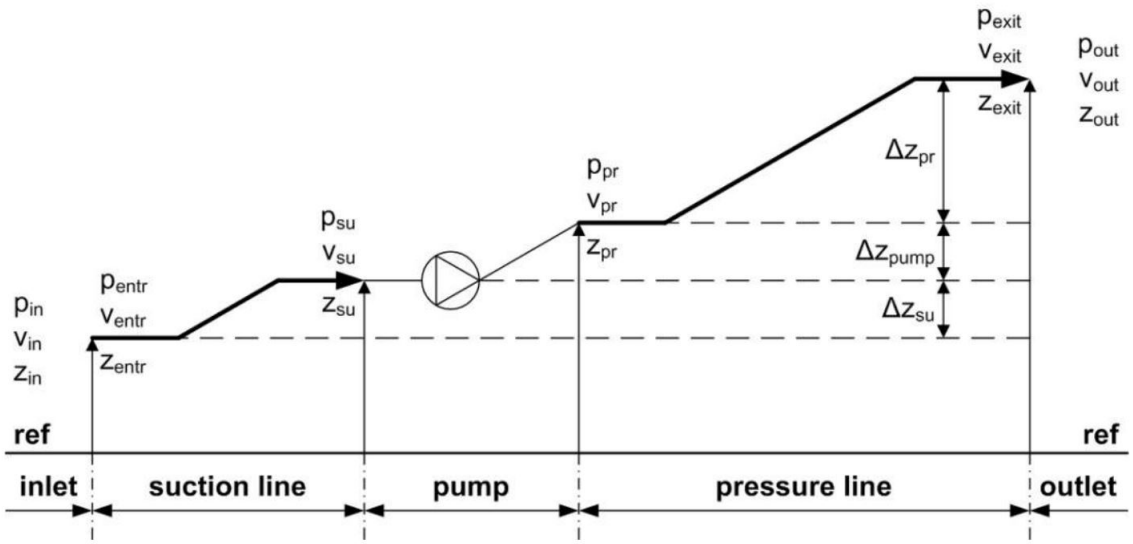

Figure 4.1: Pump in pipeline system [32]

$$\Delta p_{system}^{++} \overset{\text{def}}{=} p_{out} - p_{in} + \frac{1}{2}\rho(v_{out}^2 - v_{in}^2) + \rho g(z_{out} - z_{in}) + \Delta p_{loss,pr} + \Delta p_{loss,su} \tag{4.2}$$

$$\Delta p_{pump}^{++} \overset{\text{def}}{=} p_{pr}^{++} - p_{su}^{++} \overset{\text{def}}{=} (p_{pr} - p_{su}) + \frac{1}{2}\rho(v_{pr}^2 - v_{su}^2) + \rho g(z_{pr} - z_{su}) \tag{4.3}$$

$$\Delta p_{system}^{++} = \Delta p_{pump}^{++} \tag{4.4}$$

Using Equation 4.2, the pump must compensate the pressure difference between the in- and outlet, the height difference in the system, and the dissipative losses. In this figure, the pressure p, height z and velocity v at different locations in the system are indicated.

In Equation 4.2, $\Delta p_{loss,pr}$, and $\Delta p_{loss,su}$ are the dissipative losses in the system due to friction. The total dissipative loss in the system can be calculated using Equation 4.5. ζ is dependent on the flow (laminar or turbulent) and the number of valves, bends, pipe lengths, and other appendages within the system. Without the detailed knowledge of the system, it can be assumed that for ships, the value of ζ is between 10 - 100, according to [32]. The flow velocity can be calculated using Equation 4.6, with the volume flow $\dot{V}_{pump}$ and the pipe diameter d_{pipe}.

$$\Delta p_{loss,pr} + \Delta p_{loss,su} = \Delta p_{loss} = \zeta \frac{1}{2}\rho v^2 \tag{4.5}$$

$$v = \frac{\dot{V}_{pump}}{\frac{\pi}{4} \cdot d_{pipe}^2} \tag{4.6}$$

If the required pump power for each time step in the simulation is known, the total energy requirement in kJ can be calculated with $E = P \cdot t$, where t is equal to the total simulated time. The energy in kJ is translated into kWh with a conversion factor, which is shown in Equation 4.7, since this is a common unit to compare the energy consumption from different systems.

$$\begin{aligned} 1[kWh] &= 3600[kJ] = 3.6[MJ] \\ 1[kJ] &= 0.0002778[kWh] \end{aligned} \tag{4.7}$$

The required pump power and energy consumption are calculated using Simulink and the Matlab function pump.m, which can be found in the overview of the Simulink model in Figure 2.10. In the upcoming two sections, the difference between open and closed tank systems will be discussed.

4.1.1. Open Systems

The depth control tank (DCT) and main ballast tank (MBT) are open systems. Seawater is pumped out of the tank to the sea, or added to the tank by opening flooding holes, to compensate for weight changes. Using Figure 4.1, Equation 4.2 can be simplified for the two tank systems.

If it is assumed that within the system, there are no height differences, the following expression can be established; $z_{in} = z_{entr} = z_{su} = z_{pr} = z_{exit} = z_{out}$. For an open system, such as a ballast system, the fluid velocities v_{in} and v_{out} are assumed to be zero. v_{in} is the velocity of the fluid in the sea, and v_{out} is the (final) velocity of the fluid in the ballast tank. There is an energy loss due to the exit speed (v_{exit}), which can be seen as a dissipative, irreversible loss, since this kinetic energy loss cannot be recovered. This loss is included in $\Delta p_{loss,pr}$. Furthermore, it is assumed that the flow velocities within the system are equal, leading to the expression v_{su} = v_{pr}. Using the assumptions described above, the pump must overcome the pressure differences between in- and outlet of the system, and the dissipative losses of the suction and pressure side. The pressure difference is depth dependent since the ALERD is used as an underwater vehicle and atmospheric tanks are used. The outlet pressure p_{out} is the local (atmospheric) pressure in the tanks, and the inlet pressure p_{in} is the hydrostatic pressure, which is time-varying and dependent on the actual depth of the ALERD. The depth is measured using the position of CO in the body-fixed reference frame $\{b\}$ with respect to the inertial frame $\{n\}$. It is assumed that the pump inlet will be on the bottom of the hull. The inlet pressure will therefore be calculated at the location $z + 0.5 \cdot D$, where D is the height of the ALERD.

With the used assumptions, Equation 4.2 can be reduced to Equation 4.8.

$$\Delta p_{system}^{++} \overset{\text{def}}{=} p_{out} - p_{in} + \Delta p_{loss,pr} + \Delta p_{loss,su} \tag{4.8}$$

4.1.2. Closed Systems

The trim tank system is a closed system, using two interconnected tanks. Using Figure 4.1 for a closed system, the following definitions can be made.

- $v_{in} = v_{out}$
- $p_{in} = p_{out}$
- $z_{in} = z_{out}$

Equation 4.2 therefore reduces to Equation 4.9. In a closed system, such as a trim tank system, only dissipative losses in the system need to be compensated by the pump [32].

$$\Delta p_{system}^{++} = \Delta p_{loss,pr} + \Delta p_{loss,su} = \Delta p_{loss} \tag{4.9}$$

Height differences will play a role if the ALERD has a trim angle. In the simulation model, it is assumed that the center of the fore and aft tank are located 30 meter fore and aft of CO (=CB). A pump is placed in this system to pump water from one tank to another. Considering the distance between the tanks and the potential height differences in the system when the ALERD has a trim angle, there may arise an additional static pressure head which the pump needs to overcome. However, since one of the control objectives in the simulation model is that the trim angle must be kept zero at all times, this potential height difference is not taken into account. The control objective of keeping the trim angle at zero degrees is seen as a valid assumption if the operational area is the Dutch North-Sea coast, because of the restricted depth of 20 - 25 meters and the length of the ALERD of 80 meters.

4.1.3. Constraints and Input Parameters

In Chapter 3, the controller constraints are defined. The controller constraints are based on the maximum volume flow that is allowed within the pipe-flow system, and can be found in Table 3.7. The maximum volume flow is directly based on the output of the motion controllers, and used as input to calculate the required power for the pumps, and the corresponding energy consumption. This will also be explained in Chapter 6, where the results of the time-domain simulation are described, including the corresponding energy requirements for the pumps.

Based on the controller constraints, and to be able to calculate the required power and energy consumption, a pipe diameter is defined for the main ballast tank, the trim tank system, and the depth control tank. The pipe diameters are determined, based on the expected volume flow. From Table 3.7, it can be seen that if the expected volume flow is high, the pipe diameter must be chosen high enough,

since the corresponding maximum flow velocity in the pipes is a hard constraint. The chosen values for the pipe diameters and the corresponding maximum mass flow rates can be found in Table 4.1.

Table 4.1: Pipe diameters for the different tank systems

	Pipe Diameter [m]	**Maximum Mass Flow Rate [kg/s]**
MBT	0.5	707
DCT	0.2	81
TT	0.4	410

4.2. Compressed Air System

Using compressed air instead of pumps is another way of removing ballast water from the tanks. In case of the ALERD, only the main ballast tank and depth control tank can be emptied using compressed air, since the trim tank system is a closed system using pumps to move water around. In order to compare the energy requirements for emptying the tanks, a compressed air system is included in the simulation model. Compressed air is stored under high pressure in air bottles and stored onboard the ALERD. Compressed air bottles can be filled using compressors, which need to be done onshore, since it is expected that the ALERD will not surface during its operations and does not use a snorkel for fresh air supply.

Atlas Copco is a leading supplier in industrial solutions such as compressors and compressed air installations. Information is provided by Atlas Copco to C-Job regarding the required power for filling compressed air bottles. In Table 4.2 a calculation is made for the amount of bottles required to empty the MBTs once. According to the information provided by Atlas Copco, each bottle has a useful volume of 10 m3 if air is stored at a pressure of 300 bar. Using the total volume of the main ballast tanks, at least 202 compressed air bottles are needed to empty the main ballast tanks once. However, since it is assumed there will be multiple dredging and discharging cycles before heading back to the harbor, the number of bottles most be doubled or tripled, depending on the number of dredging cycles.

In Table 4.3 the required power and time to fill one compressed air bottle from 100 to 300 bar is given. It takes 12 minutes to fill one compressed air bottle from 100 to 300 bar, which requires 16 kW of power, according to information provided by Atlas Copco.

Table 4.2: Compressed Air System Characteristics MBT

Volume Air Compression Bottle	0.05 m^3
Volume Air Compression Bottle @ 300 bar	15 m^3
Useful Volume @ 300 bar	10 m^3
Volume MBT	2015 m^3
Required bottles for MBT	202 [-]

Table 4.3: Energy Requirement Compressed Air System

Required Power (100 to 300 bar)	16 kW
Filling Time One Bottle	12 min

The information above is implemented in the Matlab file CompressedAir.m, which can also be found in the Simulink overview from Figure 2.10.

4.2.1. Power and Energy Calculation Compressed Air System

The required power and energy consumption, using a compressed air system, is calculated for the MBT and DCT. The MBT is independent of the motion controllers, due to the assumption that the weight difference in the hopper is compensated instantaneously, leading to no additional heave forces (see Chapter 3 for the detailed explanation). The trim tank is not included, since only pumps can be used.

To calculate the required power and energy consumption for the DCT, the volume flow $\dot{V}$ is used as input in the function CompressedAir.m. The volume flow $\dot{V}$ is based on the output of the motion

controller for the depth, and also used to calculate the power and energy of the pump system. It is assumed that the volume flow of water going out from the tanks must be equal to the volume flow of air coming into the tanks. Therefore, the total volume flow during the entire simulation is summed up (integrated) to calculate the total required volume of air, needed to empty the DCT. This volume can be transformed to the number of bottles required for the DCT. The required amount of bottles can be multiplied by the required power to fill one bottle, to calculate the total amount of required power. Using the basic equation $E = P \cdot t$, the time to fill one bottle can be used, in combination with the required power to fill one bottle, to calculate the total energy consumption for filling all the required bottles.

It is important to note that the required amount of bottles for a compressed air system is based on the output of the motion controller and the applied constraints. The mass flow rate is a constraint, based on the maximum allowable fluid velocity in the pipes. The maximum allowable fluid velocity is also applicable for the compressed air system, since the water will be pushed out of the tank's trough pipes, similar as for the pumps. However, physical constraints of the compressed air system are not taken into account by the controllers. A physical constraint of the compressed air system is for instance the amount of space onboard, reserved for the compressed air bottles, instead of a maximum volume flow rate.

4.3. Results and Comparison

As already mentioned in the previous section, the amount of required energy for the compressed air system is directly coupled with the pump system, and its physical constraints. However, a comparison can be made, using the calculated amount of kWh for both the compressed air system and the centrifugal pump for one complete operational cycle. This will be done in Chapter 6 using the final result from the time-domain simulations, with the different motion controllers.

5

Validation

In this chapter, the developed simulation model will be validated. Due to the lack of existing data from the ALERD, it is not possible to compare the theoretical outcomes from the simulation model with experimental data, from for instance model tests. Therefore, a sanity check will be done here, to assess the outcomes based on common sense and engineering knowledge.

5.1. Sanity Check

Newton's Second Law

For the depth controller, using either the PID controllers or MPC, the required amount of mass can also be roughly estimated using Newton's Second Law from Equation 5.1, considering the pure heave motion.

The mass, in this case the displacement of the ALERD with in addition the added mass, is known. The acceleration can be determined as well, by time-differentiation of the signal for the vertical speed. By disregarding the other matrices in Equation 2.1, an indication of the order of magnitude of the required force can be given.

$$F = m \cdot a \tag{5.1}$$

The heave velocity can be time-differentiated to obtain the heave acceleration, which is done using results from the simulation model, and a maximum vertical acceleration of 0.012 m/s^2 is obtained. Using this acceleration and the mass of the ALERD, the required heave force and corresponding required mass in the DCT can be determined. With the maximum heave acceleration of 0.012 m/s^2, the displacement of 10830000 kg, and the added mass in heave of 9695900 kg, the required force can be calculated. The required corresponding mass is equal to 2500 kg, which needs to be added to the ALERD in order to achieve the maximum acceleration of 0.012 m/s^2.

The expected outcome of the motion controllers should therefore be in the order of magnitude of 2500 kg. Using the results from the next chapter, and Figures 6.6 and 6.19, it can be seen that for both the PID controller and MPC, the required mass that is added to the DCT is actually in the same order of magnitude (± 3200 kg and ± 1500 kg respectively). Therefore, it can be concluded that the output of the motion controllers show reasonable results. Since the calculated energy consumption is directly coupled to the outcome of the motion controllers, it can be said that these values are also reasonable.

Input Parameters

The basis for logical and reasonable outcomes of the simulation model are realistic input variables. For instance, the added mass is estimated using the assumptions of an ellipsoidal hull form. In previous studies done for the predecessor of the ALERD, the AUMD, information provided by MARIN is used to estimate the added mass in heave. In [2], it is mentioned that for submarines, the added mass in heave can be taken as 80% of the displacement as first approximation. The displacement of the ALERD is equal to 10830000 kg, and the calculated added mass in heave is 9695900 kg using the assumptions described in Chapter 2. This comes down to 89% of the total displacement, which is somewhat higher than the mentioned 80%, but it can still be seen as a reasonable result.

Internal Model Check

The final method that is used to validate the outcomes of the model is to check if the different internal relationships in the model show logical behavior.

The resulting motions during a changing condition, such as a change in mass of a tank, can be used to check the internal relationships. For instance, using the notation and positive directions from Figure 2.5, a mass addition in the forward trim tank should lead to a positive pitch angle, sending the nose of the hull down. Furthermore, a positive forward speed should lead to a positive change in x-direction. These tests do not necessarily say something about the final values for the outcomes, but can be used to validate the relationships and correct coupling between the used parameters within the model.

In Figure 5.1, the covered distance in x-direction is plotted, for the first part of the simulation. This part of the simulation covers the transit of the ALERD, from the harbor to the dredging site. The duration of the transit mode is based on the operational profile analysis made by C-Job [11], which is in more detail described in Chapter 3 and in Table 3.2. During the transit mode, the maximum speed of the ALERD is 8.5 knots, as can also be seen in Table 3.2 and in Figure 6.3. The transit mode takes approximately 1 hour (3480 seconds), so a covered distance close to 8.5 nautical miles is expected, if the equations of motion and the state-space model in x-direction are properly defined, taking into account the ship speed, modelled propellers to deliver the thrust force to achieve this ship speed, the linear damping in surge, and the calculated viscous resistance force.

From Figure 5.1, it can be seen that in one hour, a little more than 14 kilometers is traveled by the ALERD, which is approximately 7.5 nautical miles. This number is close to the expected 8.5 nautical miles. The deviation from this number can be explained by the fact that it takes a certain amount of time for the ALERD before the maximum speed of 8.5 knots is reached.

From this relatively simple test, it can be concluded that the results of the simulation model for, in this case the surge direction, show a reasonable and realistic behavior. The estimated linear surge damping, the added mass in surge direction, and the viscous resistance force contribute to realistic ship dynamics, and expected outcomes. The covered distance of 7.5 nautical miles is also in the same order of magnitude of the median transit distance, calculated in the operational profile analysis of conventional dredgers [11].

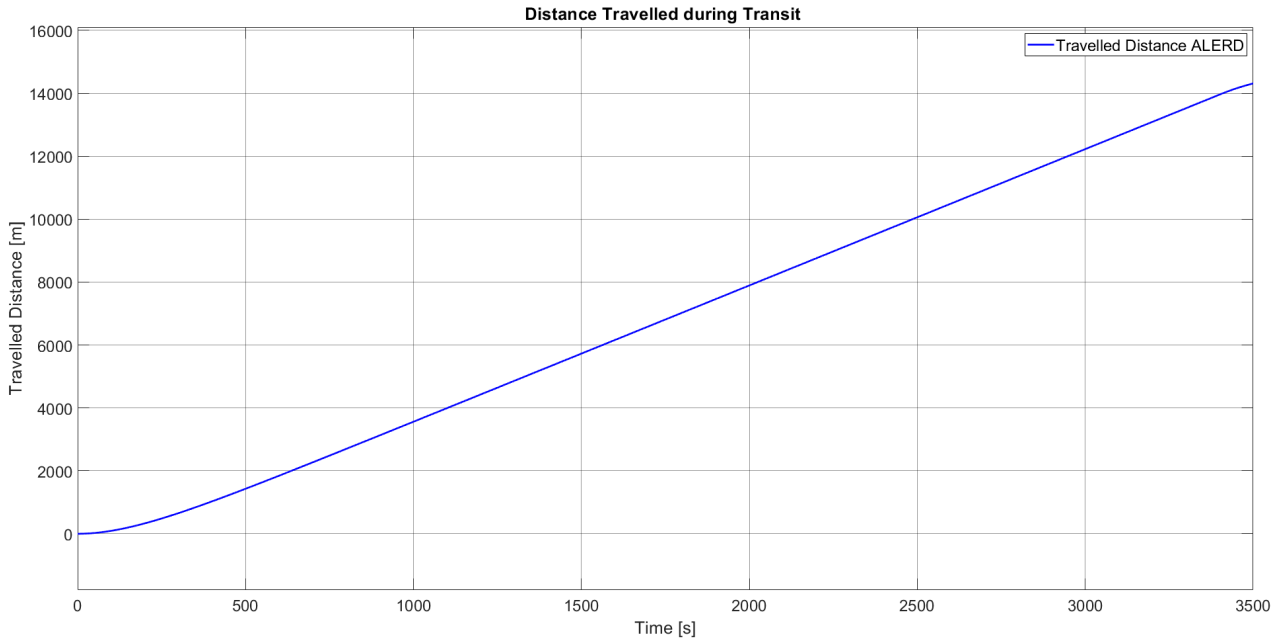

Figure 5.1: Travelled distance during transit mode

Using Figure 5.2 and Figure 5.3, the influence of trimming moments at the pitch angle can be determined. In Figure 5.2, it is clear to see that as soon as the draghead moment is applied, the sum of all the trimming moments becomes positive, and the balance of moments is disturbed. The resulting trimming moment has a positive sign, and according to Figure 2.5, this must result in a positive trim

angle θ as well. This effect is also clear to see in Figure 5.3. The maximum pitch angle is not reached instantaneously, but after some seconds, from which it can be concluded that the simulation model shows realistic behavior which is expected for the dynamics of large ships such as the ALERD. The resulting trimming moment is positive for approximately 5 seconds, after which the moved mass from the forward trim tank to the aft trim tank recovers the balance of moments. From this point, the pitch angle slowly converges to zero again. It must be noted that, although the maximum pitch angle looks quite high due to the scale of the plot, an angle of 0.1 degrees can still be considered negligible, taking into account the total length of the ALERD of 80 meters.

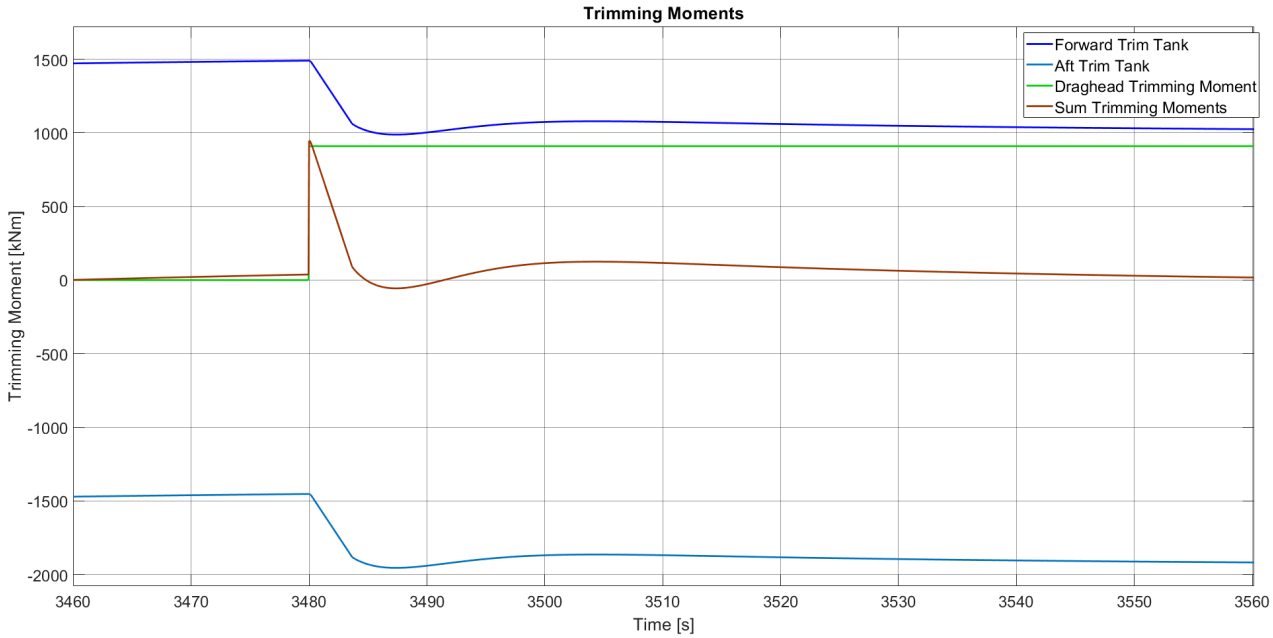

Figure 5.2: Travelled distance during transit mode

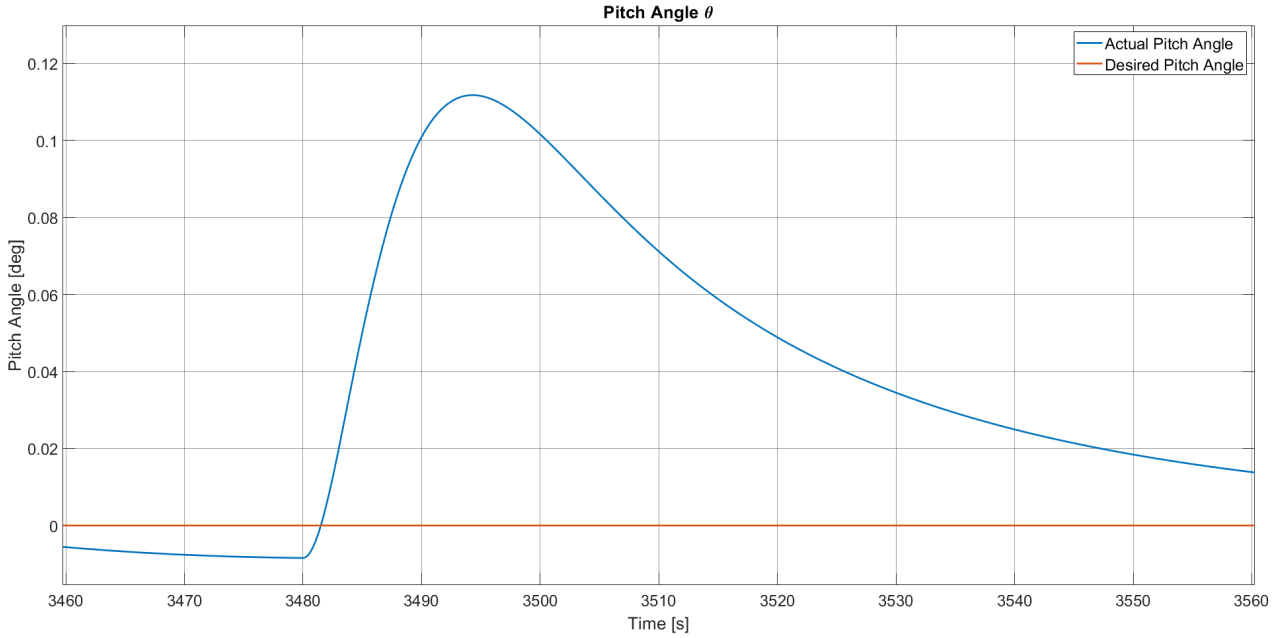

Figure 5.3: Change in pitch angle θ

5.2. Conclusion

In this section, the simulation model is validated using the best available options. Due to the lack of existing data of the ALERD, validation of the model with experiments such as scale model tests or CFD-analysis is not possible at this point. Therefore, a sanity check is performed, by using common sense and engineering knowledge to assess the outcomes of the model and to check whether the model behaves as expected, by checking the relationship between applied forces and resulting directions and their motions.

By making relatively easy calculations, the order of magnitude of the expected output can be determined. It is shown that the output of the PID controller and MPC are around this expected order of magnitude, and show therefore realistic behavior.

Furthermore, it can be concluded that within the simulation model, the internal connections and relationships between forces and motions behave as expected. The directions and orientation of the resulting motions from the ALERD due to disturbances or forces are in line with the definition according to Figure 2.5.

One of the important coefficients in the equations of motion, which is the added mass in heave, is checked using information provided by MARIN. The calculated value for the added mass is close to the approximation which MARIN has suggested.

Combining the findings from above, it can be concluded that the simulation model performs as expected, showing realistic behavior and reasonable outcomes. A more complete validation approach, such as comparison with experiments carried out in the literature, with experimental scale model tests, or with results from CFD-analysis, is a recommendation, given in more detail in Chapter 8.

6

Simulation Results

In this chapter, an overview of the results from the simulation model, using the different motion controllers, will be given. The motion control methods, described in Chapter 3, are compared with each other based on their performance, constraint handling, robustness and KPIs. The simulations are carried out using the generated references for the pitch angle, the depth, and the different disturbances from Chapter 3. The energy requirements for the reference tracking are calculated based on the output from the controllers and the used stabilizing systems, which are discussed in Chapter 4.

6.1. Performance PID Controllers

In this section, the outcomes from the simulations using two PID controllers for the pitch angle θ and the depth z will be discussed. The PID controllers are implemented in the simulation model using the standard PID blocks from the Simulink library. In these blocks, an automatic tuning function can be used, which automatically selects values for the proportional gain K_p, the derivative gain K_d, and the integral gain K_i. The controller constraints, defined in Chapter 3, are used to limit the controller output to make the simulations realistic. In Section 6.1.1, the results from the automatically tuned PID controllers are described. In Section 6.1.2, manual PID tuning is done, to be able to compare the results.

6.1.1. Automatically Tuned PID Controller

In Figure 6.1 and 6.2, the reference tracking for the depth and the pitch are plotted. The desired depth and pitch angle are based on the operational profile of the ALERD, and can also be found in Figure 3.1 and 3.2 in Chapter 3. The simulations are done taking into account the disturbances due to the dredging and discharging operations, which can be found in Figure 3.6 and 3.7 in Chapter 3.

As can be seen, the PID controllers try to ensure the reference signal for the depth and pitch is followed, by calculating the actuator input required to provide the control forces and moments. In Table 6.1, two key performance indicators (KPIs) of the controllers are listed, which are the overshoot and settling time of the actual depth. As can be seen in this table, the maximum overshoot of the actual depth with respect to the reference depth is 4 meters. Since the desired reference depth is 8 meters, an overshoot of around 4 meters leads to an actual depth of 12 meters, which is a maximum overshoot of 51%. Since the ALERD is an autonomous underwater vehicle, such large overshoots are unfavorable, especially when operating close to the seabed. The settling time is long, however, this number is based on the time it takes for the error between the actual depth and desired depth to go to zero. In reality, larger errors (0.01 - 0.1 meter) might be considered acceptable.

From the KPIs in Table 6.1, it can be concluded that the controller performance is not sufficient from a realistic point of view, since an overshoot of 4 meters at the desired water depth of 15 meters during dredging will lead to a collision with the seabed in reality, taking into account the maximum water depth of 21 meters and half the diameter of the ALERD. Therefore, manual tuning is necessary in order to improve the reference tracking, which will be done in Section 6.1.2.

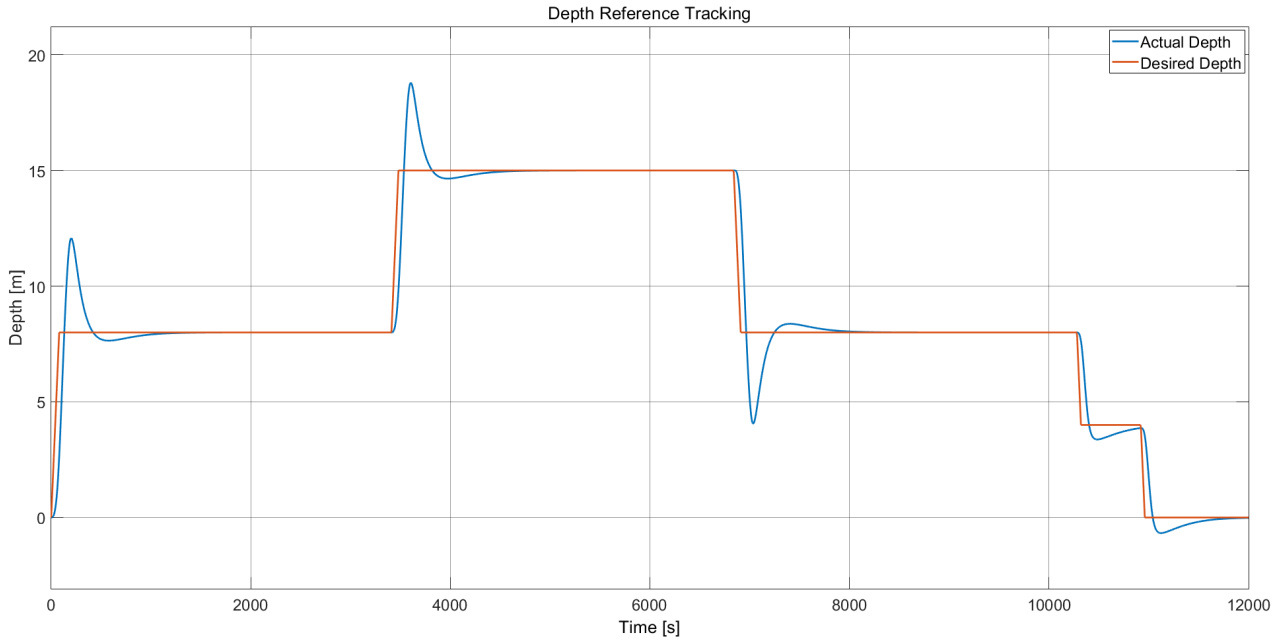

Figure 6.1: Reference tracking of the desired depth

Table 6.1: PID Controller Performance for the depth

Depth Controller Performance	
Maximum Overshoot [m]	4.08
Maximum Overshoot [%]	51
Settling Time [s]	1876

In Figure 6.2, the actual and desired pitch angle are plotted. The desired pitch angle is zero degrees at all times, due to the shallow water depth and length of the ALERD. As can be seen in this figure, the pitch is almost zero at all times, from which it can be concluded that the controller for the pitch angle works sufficient. The small deviations in the pitch angle are caused by the draghead trimming moment (Figure 3.7) and relatively fast changes in depth (Figure 6.1). A trim angle of 0.1^o leads to a vertical displacement of the front and aft of the ALERD of 7 cm, if the length of the ALERD is 80 meters. Furthermore, the trim angle quickly goes to zero after the deviations occur. Therefore, it can be concluded that the automatically tuned PID controller for the pitch works sufficiently, and manual tuning is not necessary.

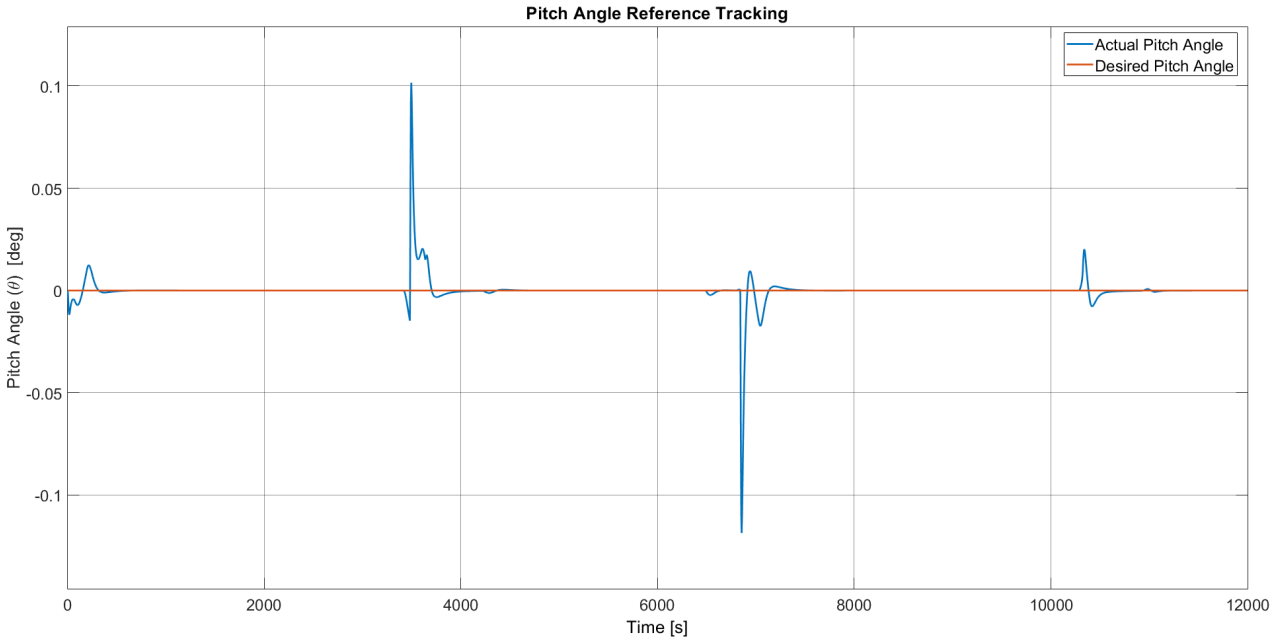

Figure 6.2: Reference tracking of the desired pitch

Table 6.2: Energy requirements pumps and compressed air system for depth and reference tracking

		MBT	DCT	TT
Pump System	Maximum Power [kW]	443	50	201
	Energy [kJ]	1469272	17155	1404
	Energy [kWh]	408	5	0.40
Compressed Air System	Maximum Power [kW]	3266	60	-
	Energy [kJ]	2351610	43270	-
	Energy [kWh]	653	12	-

Table 6.3: Comparison total energy requirements

	Total Power [kW]	Total Energy [MJ]	Total Energy [kWh]
Pump System	694	1488	413
Compressed Air System	3527	2396	666

In Table 6.2 and 6.3, the energy consumption is shown, required for tracking the desired depth and pitch reference signal, and for compensating the change of weight in the hopper, using the MBTs. A distinction is made between the pump system and the compressed air system, which are described in detail in Chapter 4. For the trim tank system, no values are included when using the compressed air system, since the trim tanks can only operate with pumps. Based on the results from Table 6.3, it can be concluded that the pump system is more favorable in terms of the energy consumption.

Since the results for the depth reference tracking are not satisfactory due to the large overshoot, manual tuning will be done in the next section, which can have an effect on both the controller performance, and on the energy requirements.

Speed Controller

The results of the speed controller can be found in Figure 6.3. It is clear to see that the corresponding speeds for the different operational modes from Table 3.2 are followed, such as the transit speed of 8.5 knots, the dredging speed of 1.8 knots, and the discharging speed of approximately zero knots. There is some overshoot in the speed due to the tuning of the controller.

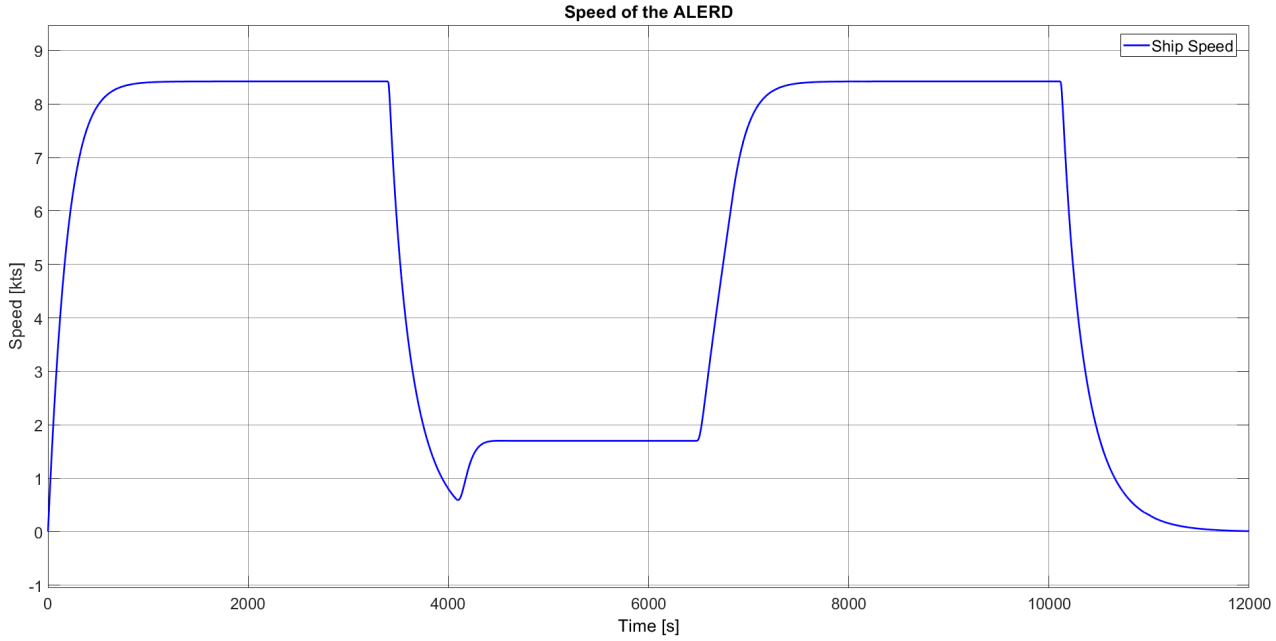

Figure 6.3: Speed control for the complete operational profile

As mentioned in Chapter 3, the speed controller is used to control the speed, corresponding to the different operational modes. The actual speed is used as input in the state-space representation. The speed is not used for energy calculations, since it does not contribute to the energy requirements for stability and buoyancy control. A prediction of the required power for the ALERD is already done in [10], prior to this research. Since the speed controller is only used to create a realistic, time-varying speed profile taking into account the ship dynamics, and the results from Figure 6.3 are satisfactory, only PID control is used for the speed. When MPC is used in the simulation model, the signal of the speed profile from Figure 6.3 is used, instead of using MPC to control the speed.

6.1.2. Manual Tuned PID Controller

In this section, the PID controller for the depth is manually tuned in order to get better results for both the controller performance and the energy consumption required for the depth reference tracking.

The performance of the PID controller for the pitch angle (Figure 3.2) is considered to be sufficient, and is therefore not tuned manually. Only small pitch angles occur, which can be considered negligible for the ALERD.

For the depth controller, manual tuning is done by varying the PID tuning parameters, K_p, K_i, K_d. The results can be found in Table 6.4. Different values for the tuning parameters are used to evaluate the performance of the controller in terms of the overshoot and settling time, and to evaluate the required energy consumption and maximum power. The overshoot in Table 6.4 is measured with respect to the dredging depth, which is 15 meters (see Figure 3.1). Dredging is done close to the seabed, meaning that a large overshoot while descending will lead to a collision with the seabed in reality. As noted in the previous section, the settling time is the time it takes for the error between the actual depth and the desired depth to converge to zero. The settling time is measured from the start of the simulation, at time $t = 0$, until the error is zero. It must be noted that the settling time can also be measured when the error is 2% to 5% with respect to the desired reference, which can lead to a significant decrease in settling time. However, it is chosen to use an error of zero, which also enables to see whether there will be a steady-state error.

The maximum power P_{max} and energy consumption E (in [MJ] and [kWh]) in this table are based on the pump system for the depth control system. In the previous section, it is concluded that the pump system requires less energy than the compressed air system. Both the pump system and the compressed air system use the required volume flow from the PID controllers as input for the calculations for the required power and energy, and therefore it can be concluded that the compressed air system will always require more energy than the pump system, regardless of the performance of the controller.

Therefore, it is chosen to use the energy requirements for the pump to compare the simulations with different tuning parameters.

In Table 6.4, 13 simulations are shown with varying tuning parameters for the PID controllers. Varying the PID tuning parameters can be done manually, or by using the tuning app, which is shown in Figure 6.4. In the tuning app, the PID values can be chosen automatically, or by adjusting the two sliders, indicated in orange. By changing the response time and the transient behavior, the performance of the controller changes accordingly. The automatically chosen PID parameters are also indicated in orange, and the corresponding tuned response is plotted with the blue line. The dashed blue line represents the current response of the controller. The PID values in Table 6.4 which have decimal numbers are generated using the tuning app and the sliders, where the other values are manual input.

In Table 6.4, simulation number 12 uses the automatically tuned PID parameters, described in the previous section.

For the other simulations, manual tuning is done using trial-and-error. The starting point are the automatically tuned parameters from simulation number 12. Using the theory behind PID control, described in Chapter 3, it is clear that using higher values for the tuning parameters, the controller will be more aggressive and faster, leading to higher overshoots and shorter settling times. Lower values will result in a slower, more robust controller, with a smaller overshoot and a longer settling time. This can also be seen in Table 6.4.

The simulations from Table 6.4 all have stable solutions, where the PID controller is able to track the reference signal for the depth (Figure 3.1), with varying performance in terms of speed, oscillatory behavior, overshoot, and settling time. Tuning parameters outside the range of values from Table 6.4 result in unstable behavior, and are not included. Therefore, it can be said that the table contains the range of possible tuning values for the controller which result in a stable solution.

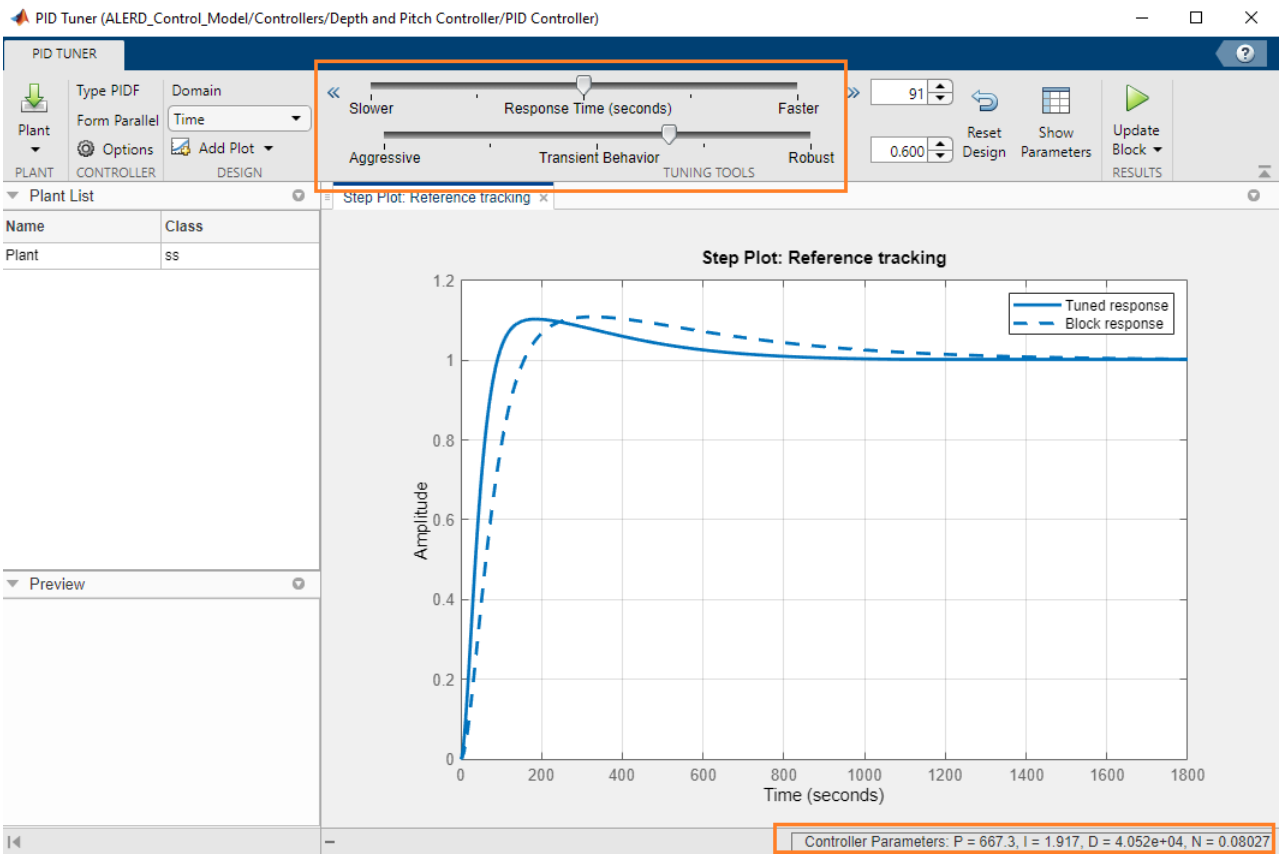

Figure 6.4: Simulink PID tuning app

Table 6.4: PID tuning parameters and corresponding maximum power and energy consumption

#	K_p	K_i	K_d	P_{max} [kW]	E [MJ]	E [kWh]	Overshoot [m]	Settling Time [s]
1	100	0.1	10000	44.36	1.74	0.48	0.29	Steady-State Error
2	250	0.25	15000	45.87	3.73	1.04	0.61	3410.15
3	250	0.5	15000	45.85	3.79	1.05	1.07	1846.45
4	197.91	0.23	12902.42	45.86	4.00	1.11	0.85	3410.00
5	175.56	0.18	18764.37	45.88	4.82	1.34	0.69	Steady-State Error
6	**356.4**	**0.7**	**21260.3**	**45.85**	**7.08**	**1.97**	**0.78**	**2128.80**
7	350	1.5	20000	45.85	7.27	2.02	1.70	1900.00
8	400	1	20000	45.85	7.73	2.15	1.17	1530.65
9	550	1.5	30000	46.45	12.39	3.44	1.73	1029.05
10	550	1.5	3000	43.56	6.12	1.70	2.83	Steady-State Error
11	700	1.5	30000	48.85	15.62	4.34	3.02	Steady-State Error
12	667.31	1.92	40516.68	49.91	17.16	4.77	3.79	418.80
13	700	2	40000	50.08	17.61	4.89	3.92	1800.00

From the results in Table 6.4, it can be concluded that a trade-off must be made between the required energy for the reference tracking and the controller performance in terms of overshoot and response time. Low energy consumption is often associated with poor performance of the controller, such as a slow response, a long settling time or a steady-state error. All these aspects are unfavorable in real life operations for underwater vehicles such as the ALERD. A fast responding controller, with a relatively short settling time, is often associated with a large overshoot, and a corresponding high energy consumption. Due to the definition of the settling time, in fact all settling times are too long, considering physical operations, however they are used to make a fair comparison between the different simulations. Furthermore, an overshoot of more than 0.5 meters can already be critical, since the ALERD will be operating close to the seabed autonomously. If safety factors must be taken into account, such as a minimum required distance between the hull and the seabed, most of the simulations show insufficient performance looking at the value for the overshoot. The first two simulations have promising results when looking at the overshoot and the energy requirements, but the response of the controller is too slow, resulting in a very long settling time or a steady-state error, which is also reached after a long time.

The simulation which looks the most promising is simulation number 6, shown in bold in Table 6.4. A clear trade-off is made between a relatively large settling time, but an overshoot which is relatively small, in combination with an average energy consumption, compared to the other simulations. The corresponding figures with plots of this simulation can be found in Section 6.2.1, where the results are described in more detail.

In general, it can be concluded that the PID controller for the depth is able to track the desired depth reference. From a realistic and operational point of view, the overshoot and settling time are too large, for most of the simulations. The corresponding required energy consumption cannot be minimized in combination with sufficient controller performance, which is the biggest downside of the controller. Therefore, a second control strategy is proposed, which is Model Predictive Control (MPC). MPC is discussed in more detail in Chapter 3, and the results of the MPC controller will be given in Section 6.2.2.

6.2. Results

In this section, a comparison will be made between the results using MPC and the manual tuned PID controller. The energy requirements for the three defined tank systems, the MBTs, DCT, and TTs, will be compared. The performance of the used controllers will be assessed based on the defined KPIs, in terms of overshoot, settling time and rise time.

6.2.1. Results Manual Tuned PID Controller

In Figure 6.5, the result of the manual tuned PID controller for the depth is shown, using the PID tuning parameters of simulation number 6 from Table 6.4. Compared with the automatically tuned PID controller from Figure 6.1, the overshoot has been decreased drastically. The KPIs of the controller

performance can be found in Table 6.5. The overshoot is decreased to 10%. The controller settings are adjusted, by making the response time slower. This results in a less aggressive controller, making the settling time somewhat higher (2129 seconds compared to 1876 seconds for the automatically tuned one). If small deviations from the desired depth (0.1 - 0.01 meters) are acceptable, the settling time decreases.

Looking at Figure 6.5, it is clear to see that the controller is relatively slow. For instance, the discharging depth at four meters at the end of the simulation is not reached at all due to the short discharging time in combination with the slow response of the controller. As described in Chapter 3, the actual depth of the ALERD is measured using the CO, which is located halfway the diameter of the ALERD. Since there is an overshoot at zero depth, the CO of the ALERD will be above the water surface at the end of the simulation using this reference depth in combination with the controller settings. In reality, zero depth of the CO means the ALERD is surfaced, which changes the buoyancy and stability characteristics of the ALERD. Since the surfaced condition is not included in the simulation model, nor in the equations of motion, this is only a theoretical result.

The results from the energy calculations can be found in Table 6.6. Due to the decoupled motions, the energy requirements for the trim tank system are not affected, since the controller for the pitch remains unchanged. The MBTs are not affected by the motion controllers, since these are only used to compensate for the change of weight in the hopper, and therefore the results for the energy consumption and required power do not change. By comparing the results in Table 6.2 and 6.6, it can be seen that the energy consumption for the DCT reduces. The manually tuned PID controller shows better performance in terms of overshoot, and in terms of energy consumption. In Table 6.7 the total energy requirements for both the pump system and compressed air system can be seen, which are decreased compared to the results from Section 6.1.1. As concluded in the previous section, the pump system requires less energy compared with the compressed air system. A detailed description of the calculation method for the power and energy requirements for the compressed air system is provided in Chapter 4.

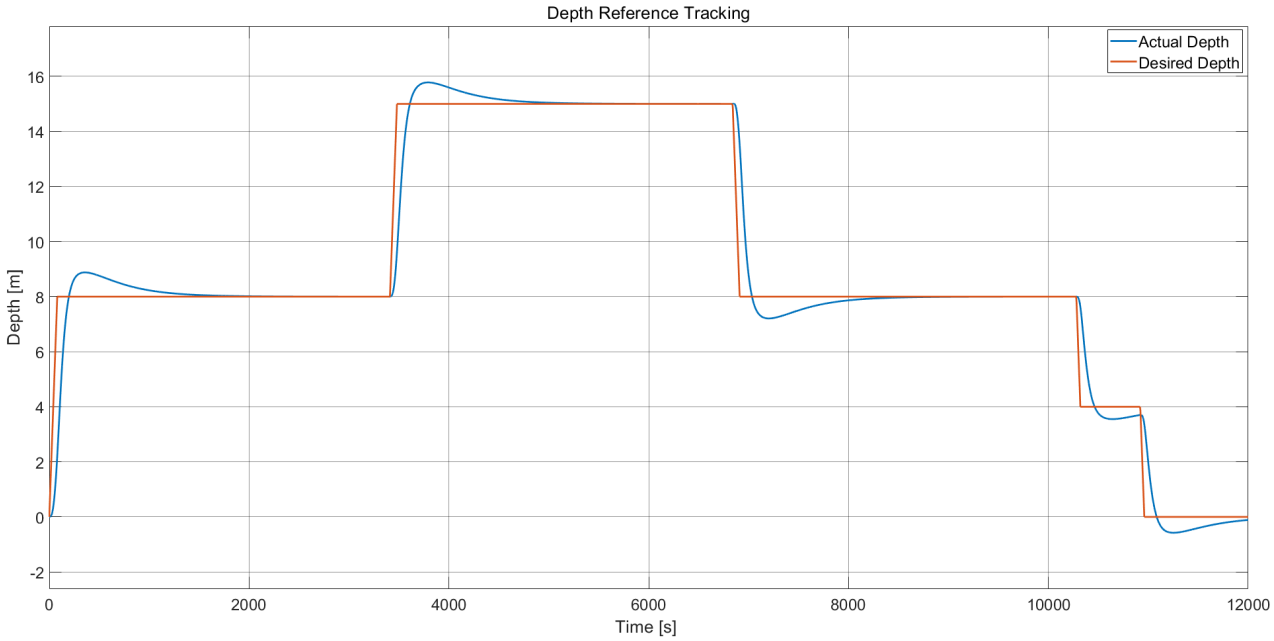

Figure 6.5: Reference tracking of the desired depth

Table 6.5: Manual tuned PID controller performance for the depth

Depth Controller Performance	
Maximum Overshoot [m]	0.879
Maximum Overshoot [%]	10.9875
Settling Time [s]	2129

Table 6.6: Energy Requirements for depth reference tracking with manual tuned PID controller

		MBT	DCT	TT
Pump System	Maximum Power [kW]	443	46	201
	Energy [kJ]	1469272	7077	1422
	Energy [kWh]	408	1.97	0.40
Compressed Air System	Maximum Power [kW]	3266	27	-
	Energy [kJ]	2351610	19209	-
	Energy [kWh]	653	5	-

Table 6.7: Comparison of the total energy requirements

	Total Power [kW]	Total Energy [MJ]	Total Energy [kWh]
Pump System	690	1478	410
Compressed Air System	3494	2374	659

Depth Control Tank

In this section, a chronological overview will be given towards the final results for the energy requirements, starting with the output of the PID controller for the depth.

In Figure 6.6, the output of the PID controller for the depth is plotted. It is chosen to have the required to be added or removed mass as output of the controller, since the physical constraints are given in terms of mass flow rate and flow velocity. In this way, the output of the PID controller can be constrained using a rate limiter, which is a standard block from the Simulink library. The mass that is added or removed from the DCT can easily be translated into a heave force, and used in the force vector $\boldsymbol{\tau}$ from the equations of motion (Equation 2.1). This is also explained in more detail in Section 3.4.

When comparing Figure 6.5 and 6.6, it is clear to see that if the desired depth is increased, mass must be added in the DCT. If there is an overshoot with respect to the desired depth, a negative mass is required, to ensure the actual depth converges to the desired depth. A negative mass (and thus a negative force) is an upward force, ensuring the ALERD will go up again or decelerates. It can be seen that since the controller is robust and relatively slow, the small overshoot requires a small negative force. The combination of the hydrodynamic forces from the (added) mass, linear damping, small Coriolis terms, and the additional heave force from the DCT, ensure the actual depth, which is the solution of the state-space model, shows a dynamic and realistic behavior of an underwater vehicle with relatively small velocities and accelerations. Due to the small vertical velocity, the mass that needs to be added or removed from the DCT is relatively small as well. For the ALERD, the maximum vertical velocity is chosen to be $0.1 m/s$, which is relatively small compared to (naval) submarines. Small velocities and corresponding accelerations ensure the corresponding energy requirements remain small as well, which will be elaborated on below.

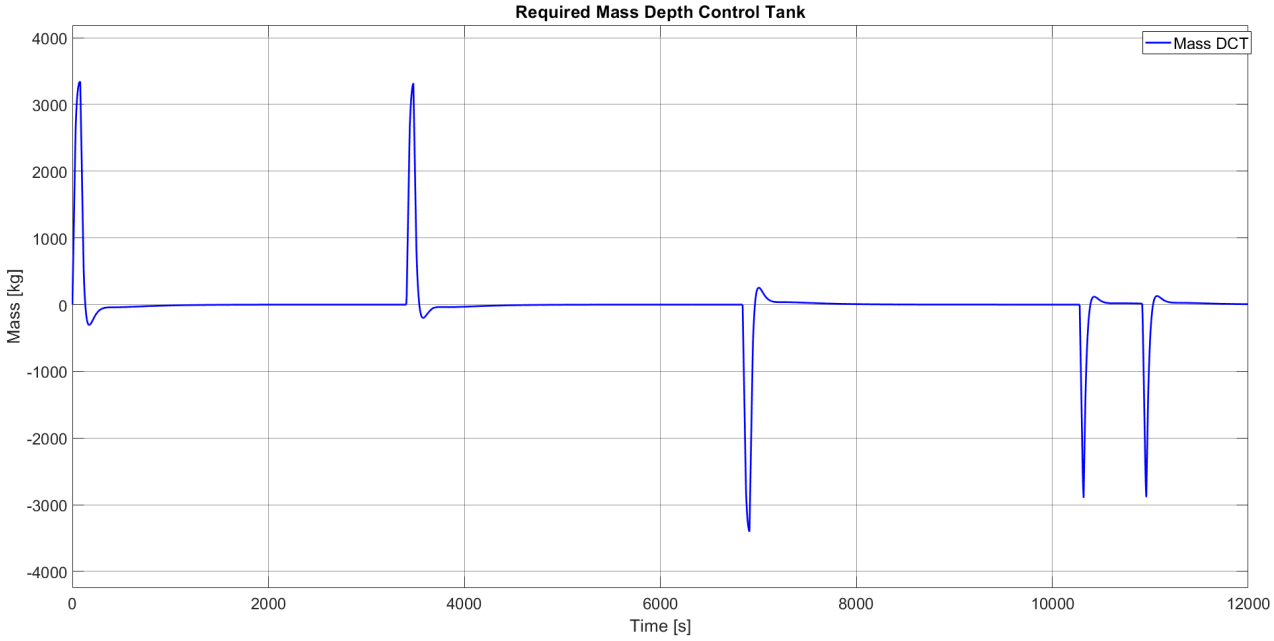

Figure 6.6: Required to be added or removed mass DCT

In Figure 6.7, the negative mass flow rate, corresponding to the removed mass from the tank from Figure 6.6, is plotted. It is assumed that, when calculating the required pump power, only the negative mass flow rate must be taken into account. A positive mass flow rate, which indicates that the tanks are being filled, is generated by opening flooding holes in the hull, and therefore does not contribute to the total energy requirements for the pump system or compressed air system. It is assumed that the maximum mass flow rate is similar for filling and emptying tanks, due to the maximum flow velocity in the system. An overview of the hard constraints can be found in Table 3.7. For the DCT, the pipe diameter is chosen to be $0.2m$. The corresponding maximum mass flow rate is $81kg/s$, which is used as hard constraint for the controller output. Looking at Figure 6.7, it can be seen that the controller does not violate the hard constraint, since the actual mass flow rate does not exceed the maximum value of $81kg/s$.

The mass flow rate is used as input for the required power and energy calculations. The Simulink model is structured in such a way, that the output from the PID controller (required mass in the DCT) is used as input in the Matlab function ALERD.m (see also Chapter 2 for an overview of the Matlab functions), translated into a heave force and implemented in the force vector $\boldsymbol{\tau}$. The state-space model is solved using the force vector $\boldsymbol{\tau}$. This means that the functions used for the energy calculations are separated from the state-space model, and are only dependent on the output of the PID controller, without directly influencing the state-space model.

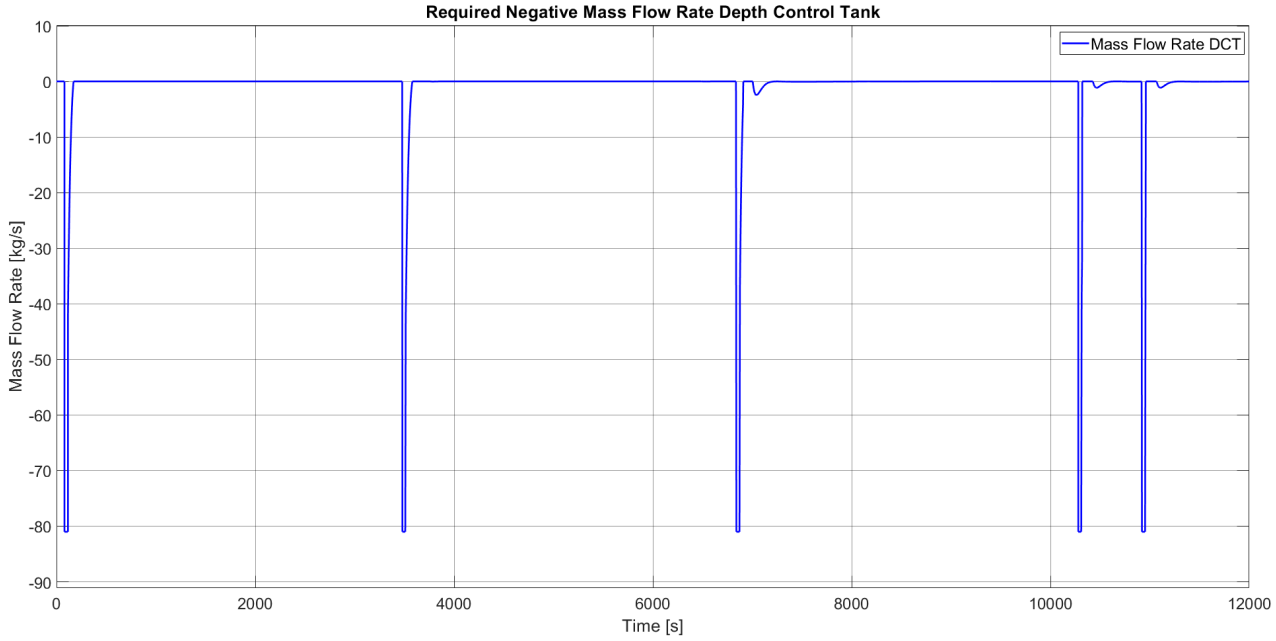

Figure 6.7: Negative mass flow rate DCT

The required negative mass flow rate from Figure 6.7 must be delivered by the pump. To deliver this mass flow rate, power is needed. The pump power is calculated using Equation 4.1, which can be found in Chapter 4.

In Figure 6.8, the required pump power corresponding to the mass flow rate can be found. It is assumed that the required power as well as the required mass flow rate can be delivered instantaneously when it is required. In reality, delays may occur in delivering the mass flow rates, as well as the required pump power, since the pumps are driven using engines or electric engines. However, the characteristics and modelling of the physical systems used to deliver the required power for the pumps are out of scope of this research and thus not considered.

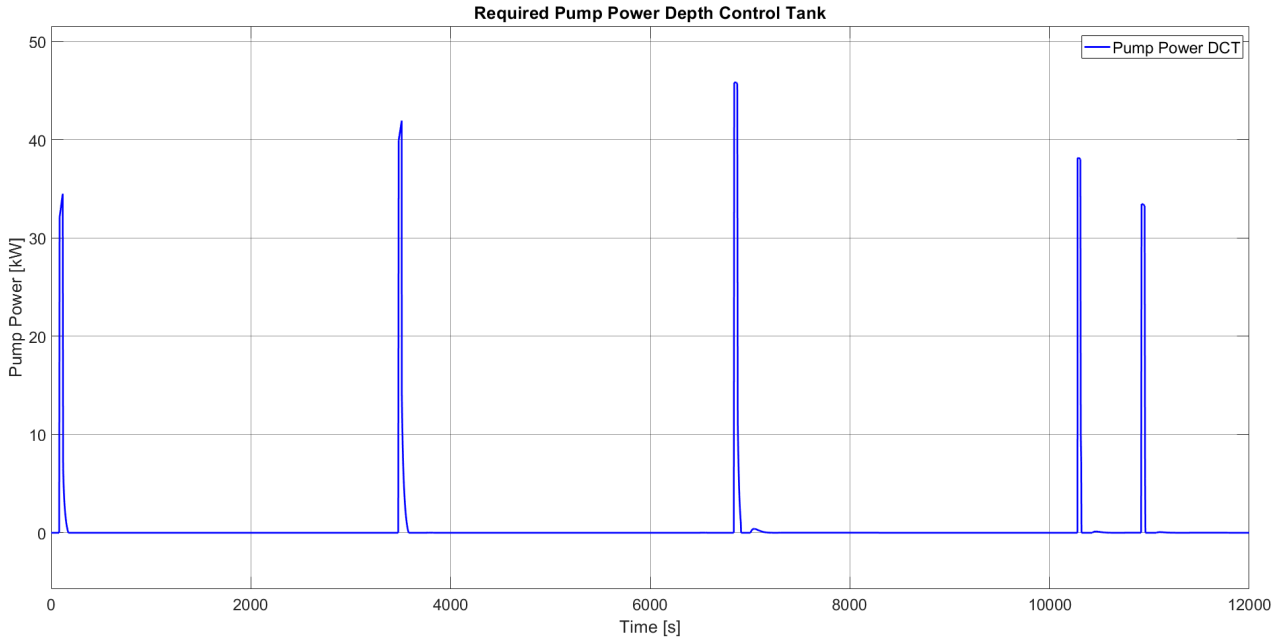

Figure 6.8: Pump Power DCT

With the required power for the pumps, the total energy consumption can be calculated. This can

be done by integrating the pump power over the total simulation time, which is essentially using the equation $E = P \cdot t$. The energy can be expressed in Joule or kWh, and a plot of the total amount of kWh required for the DCT can be seen in Figure 6.9. In this figure, a comparison is made between the pump system and the compressed air system. A detailed description of the power and energy calculations for the compressed air system, as well as the conversion from Joule to kWh, can be found in Chapter 4.

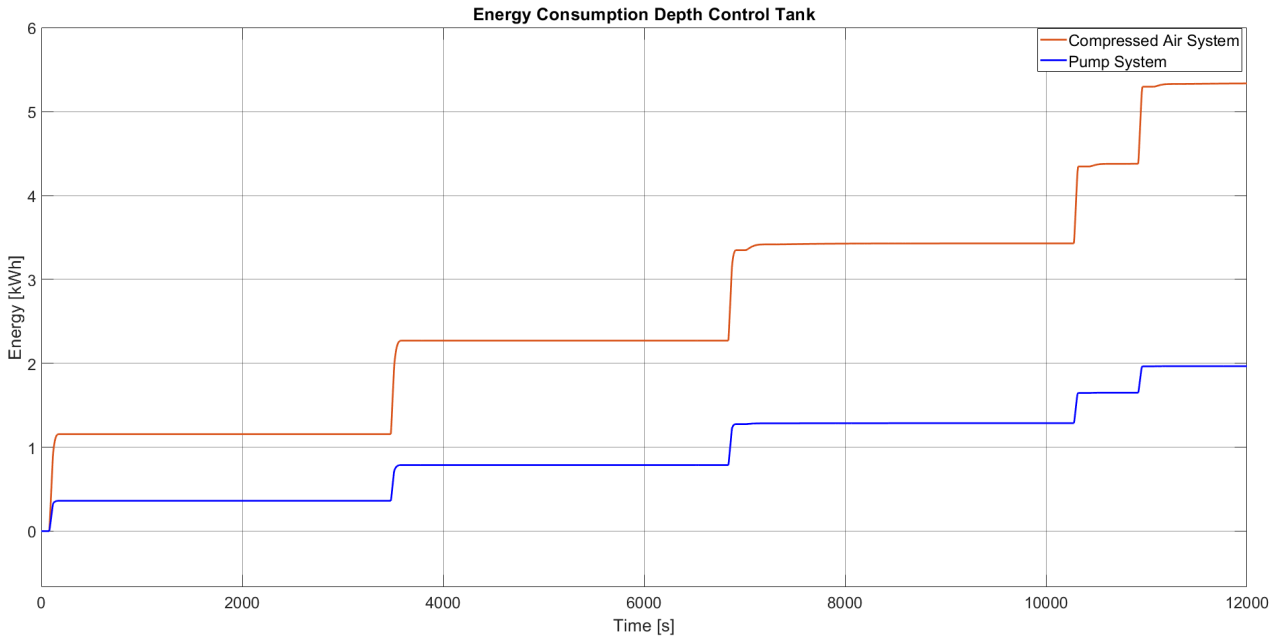

Figure 6.9: Comparison Energy Consumption Depth Control Tank

The results from Figures 6.8 and 6.9 can also be found in Table 6.6.

Main Ballast Tank

In Figure 6.10, the change in hopper mass and the change in main ballast mass are plotted. As already mentioned in Chapter 3, when the hopper is filled with the soil mixture, the MBTs are emptied. It is assumed that this is done with the same mass flow rate and at the same time instant. This assumption ensures that the weight difference between the MBTs and the hopper during the dredging and discharging operation is zero at all times, which is clearly shown in Figure 6.10. In this way, no additional heave forces are generated, and no additional compensation is required. Therefore, the DCT is used only for the required changes in depth, and the MBTs are used only to compensate for the changes of mass in the hopper. As mentioned before, the MBTs are not influenced by the motion controllers. The tank arrangement can be found in Figure 3.9. As mentioned in Chapter 3, it is expected that, to reduce the free-surface effect, the main ballast tank will be divided in multiple compartments.

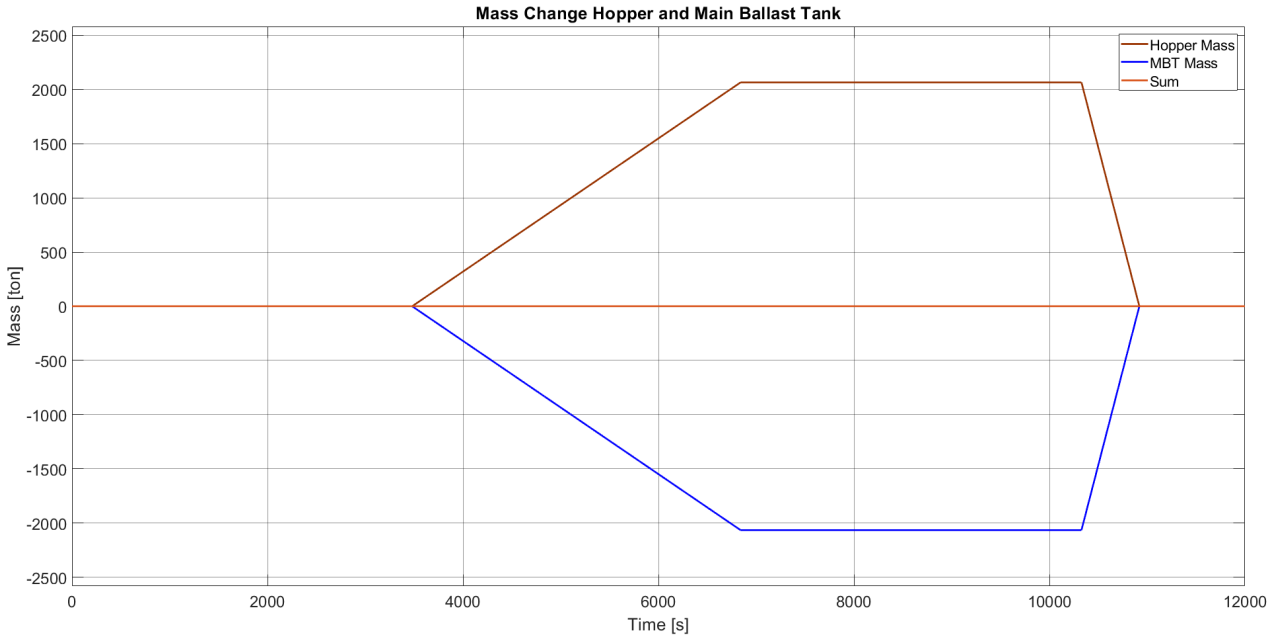

Figure 6.10: Mass change in the hopper and MBT

In Figure 6.11, the mass flow rate corresponding to the required mass in the MBTs from Figure 6.10 can be seen. The negative mass flow rate contributes to the required pump power and total energy requirement for emptying the MBTs. Since the mass in the MBTs decreases linearly, the negative mass flow rate is constant. The required mass flow rate is around $615kg/s$, and using Table 3.7, a pipe diameter of 0.5 meter is required. The positive mass flow rate during the discharging operation is much higher. For now, it is assumed that when opening flooding holes, this mass flow is achievable. Since it does not contribute to the required pump power and energy consumption, this is seen as a valid assumption.

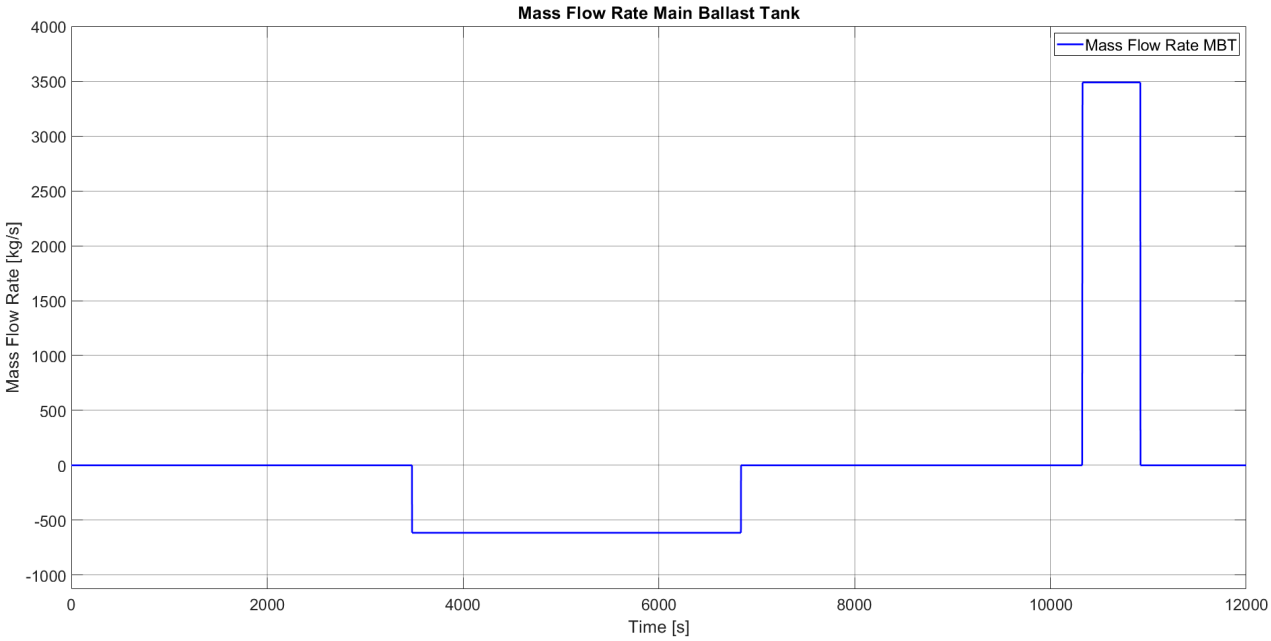

Figure 6.11: Mass flow rate MBT

In Figure 6.12, the final energy consumption for the pump system and the compressed air system is plotted. To calculate the energy in kWh, the same steps are taken as for the DCT. The pump power

is calculated using the mass flow rate, and the corresponding energy is calculated by integrating the power over time. As for the DCT, it is clear to see from Figure 6.12 that a pump system is more favorable in terms of energy consumption.

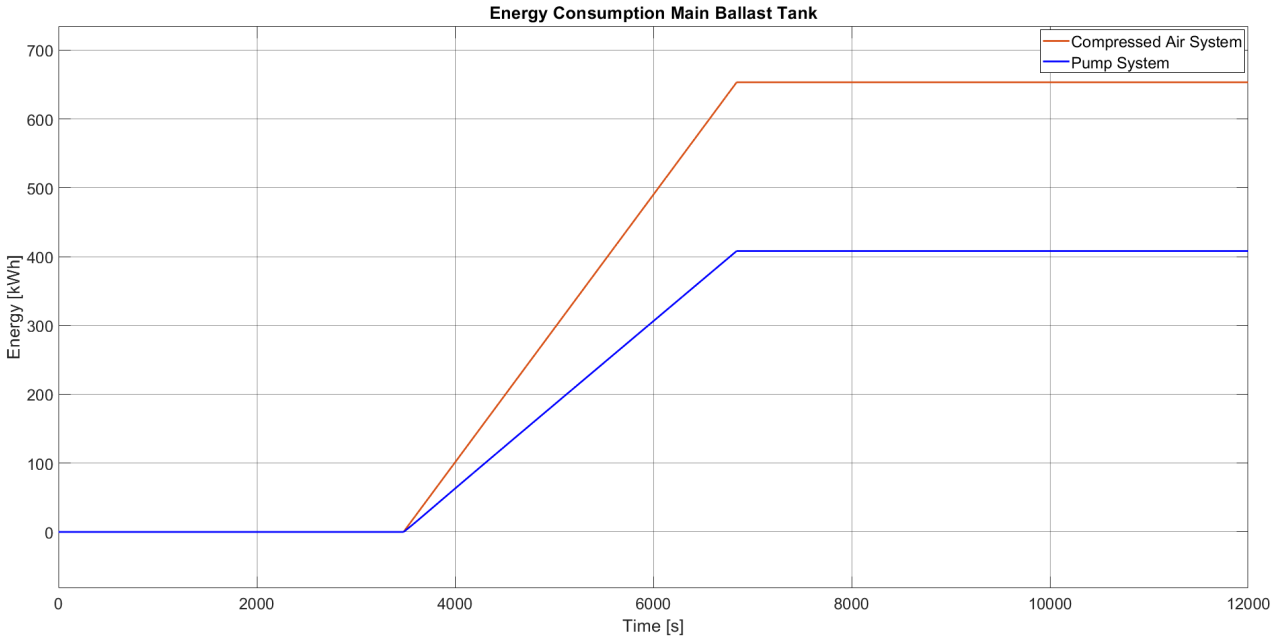

Figure 6.12: Comparison Energy Consumption Main Ballast Tanks

Trim Tank System

In Figure 6.13, the trimming moments acting on the ALERD during the complete time domain simulation are shown. Indicated in orange is the trimming moment during the dredging operation due to the draghead, see also Figure 3.7. Two trim tanks, located fore and aft in the hull of the ALERD, are used to compensate for this moment. As can be seen in Figure 6.13, the trim tanks are also used to compensate for trim angles occurring due to a relatively fast change in depth. The individual motions in 6 DoF are almost completely decoupled, apart from some small off-diagonal terms in the Coriolis-centripetal matrix from Equation 2.25 and 2.32. Therefore, small changes in the pitch angle can be observed, which are generated due to a rapid change in depth. The direction of the positive moment is clockwise, and can be seen in Figure 2.5 from Chapter 2. The trimming moment of the draghead is therefore positive, moving the front of the ALERD towards the seafloor. It is clear to see that when the draghead moment is acting on the ALERD, water is flown from the forward trim tank to the aft trim tank, to compensate for the positive trimming moment.

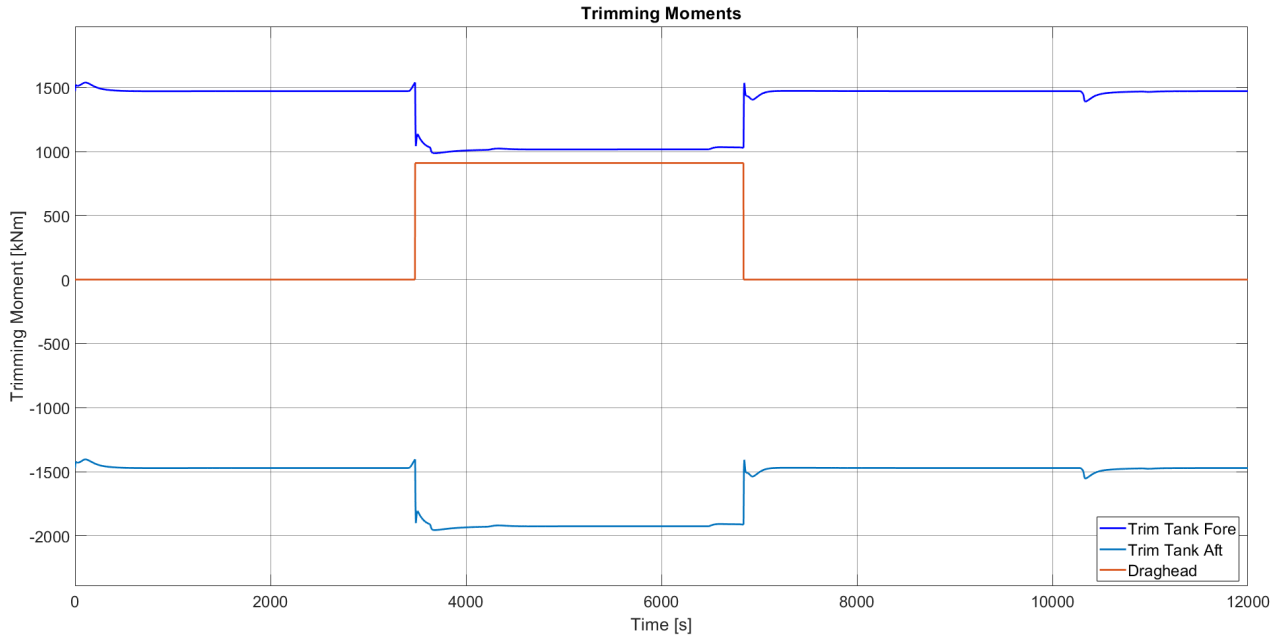

Figure 6.13: Trimming Moments

In Figure 6.14, the total trim mass, as well as the mass in the forward and aft trim tanks is plotted. It can be seen that both trim tanks start with an initial amount of mass of 5000 kg, and that the total trim mass is 10000 kg. This number was chosen arbitrarily, and is part of the displacement of the ALERD. The combined mass of the two trim tanks remains constant at all times, since it is a closed system. Therefore, using the trim tanks does not result in a change of displacement of the ALERD and no additional heave forces are required.

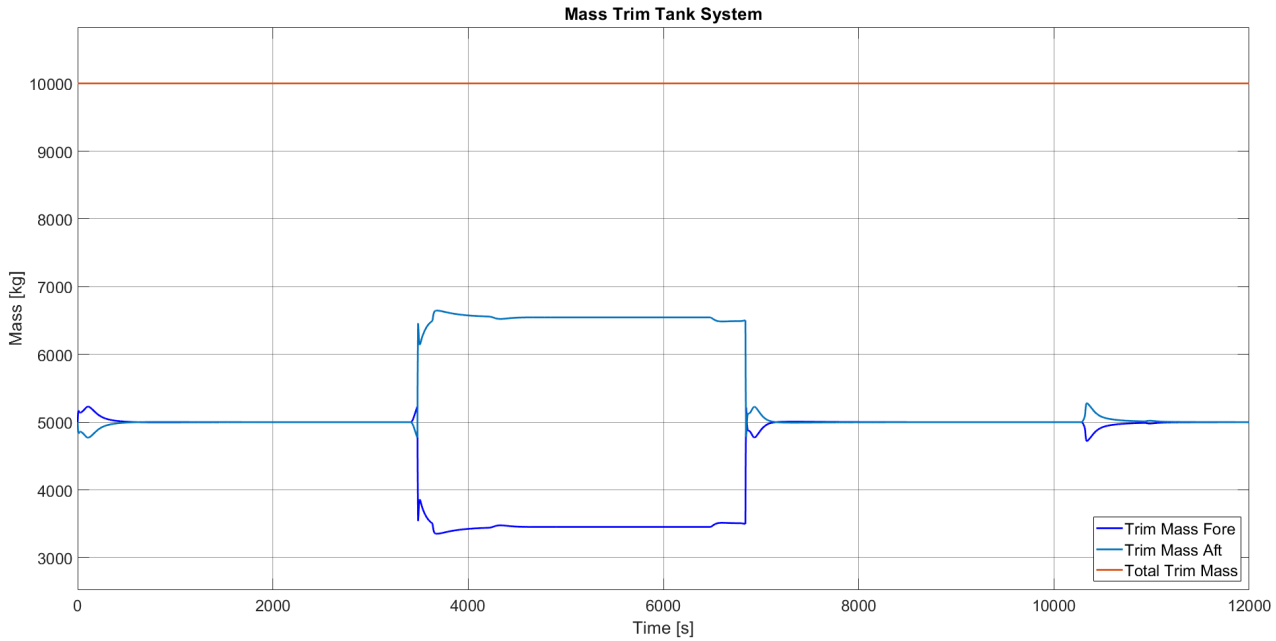

Figure 6.14: Mass in the trim tank system

In Figure 6.15 the mass flow of the forward trim tank can be found. Since the two mass flow peaks are difficult to read, due to the scale of the x-axis, Figure 6.16 is provided. This figure is zoomed in on one of the peaks. It is chosen to use a pipe diameter of 0.4 meters for the trim tank system, which has a hard constraint for the mass flow rate of $410 kg/s$. It is clear to see in Figure 6.16 that this constraint

is not violated by the controller. Similar as for the DCT and MBTs, it is assumed that the required mass flow can be delivered (almost) instantaneously by the pump.

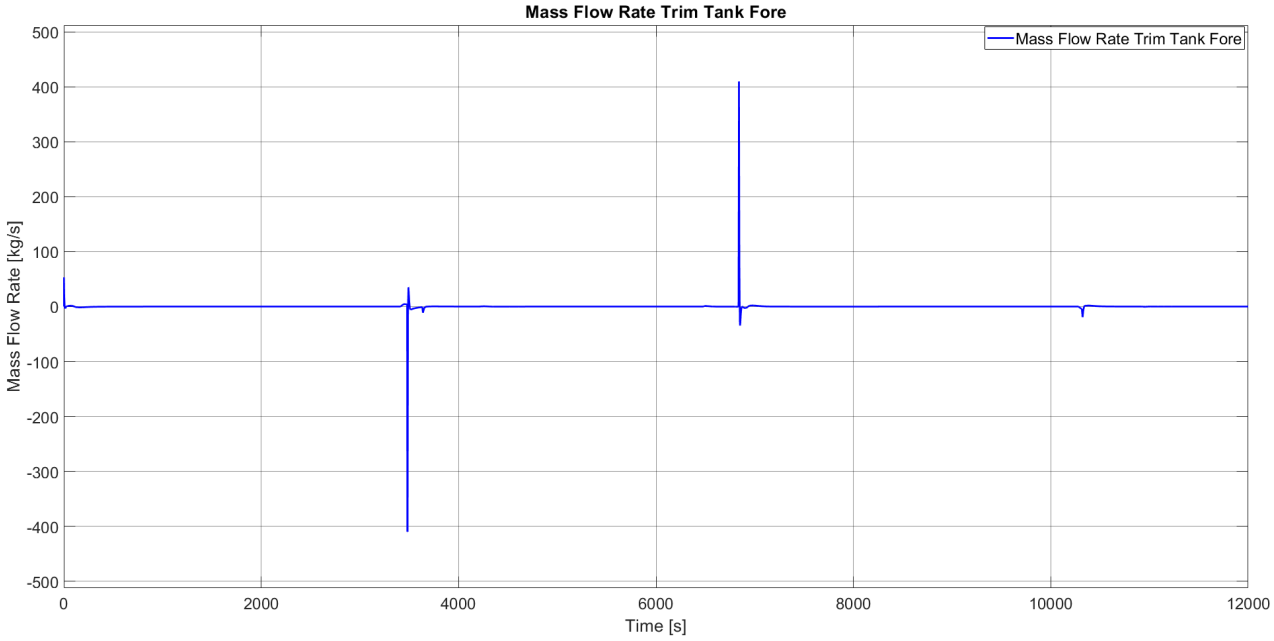

Figure 6.15: Mass flow rate in the forward trim tank

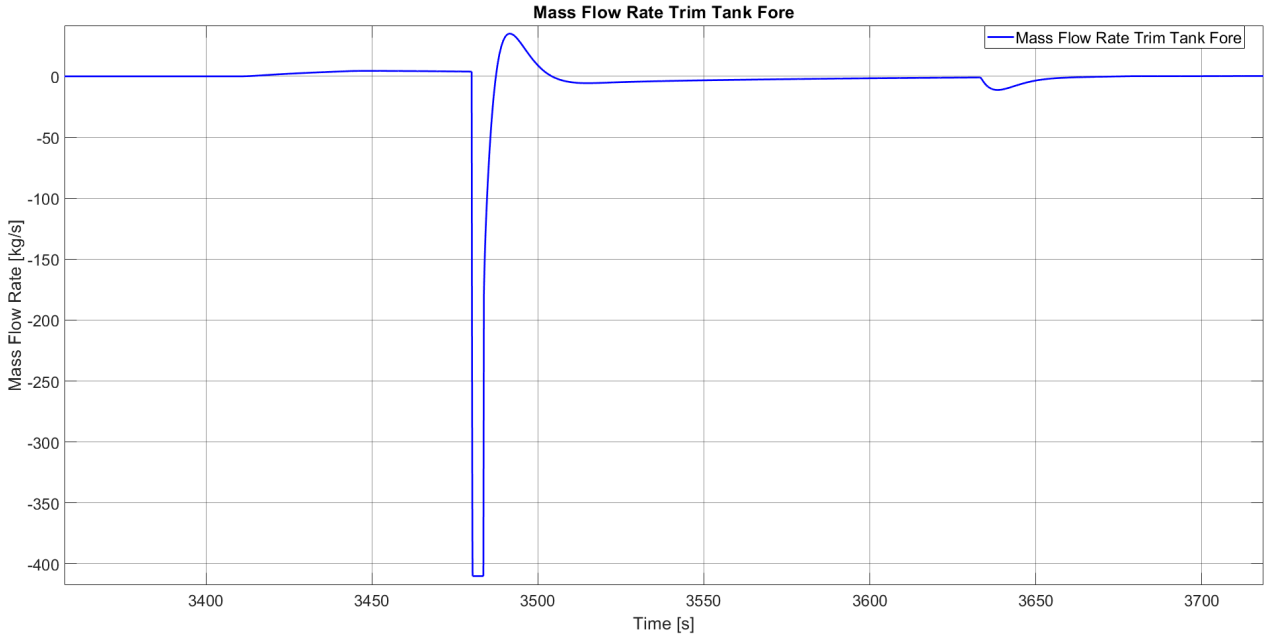

Figure 6.16: Detailed mass flow rate in the forward trim tank

In the trim tank system, a pump is used to move water around from the forward to the aft tank, and vice versa. Both the negative and positive mass flow rates must be delivered by the pump. Therefore, the absolute value of the mass flow rate over time from Figure 6.15 is used as input for calculating the trim tank power. The calculated power for the absolute mass flow is integrated over time, and the energy requirement is calculated both in Joule and kWh.

The required energy in kWh can be found in Figure 6.17. All the values described above can also be found in Table 6.6. Since the trim tank system is a closed system, where ballast water is moved

around, compressed air cannot be used. Therefore, only values for the pump system are included in Table 6.6.

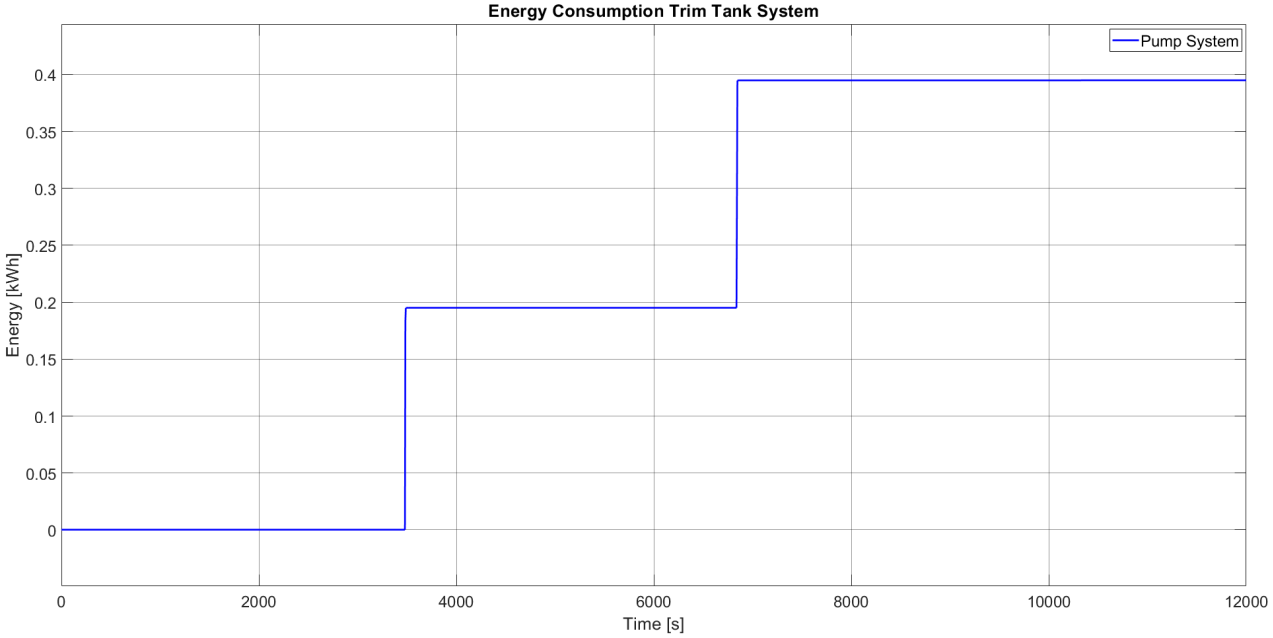

Figure 6.17: Energy Consumption Trim Tank System

6.2.2. Results MPC Controller

In this section, the results from the MPC controller for the depth and the pitch angle will be described. The MPC toolbox is used to define the MPC cost function. The used input values for the different input parameters can be found in Section 3.6.2 in Chapter 3. One MPC controller is designed to control the depth and the pitch angle.

Depth Control Tank

In Figure 6.18, the result of the MPC controller for the depth can be seen. It is clear to see that the reference signal of the desired depth is closely followed. Almost no overshoot can be recognized, unlike the results of the PID controller for the depth from Figure 6.5. The energy requirements for the reference tracking can be found in Table 6.9, and the controller performance can be found in Table 6.8. From Table 6.8, it can be concluded that the MPC controller shows robust behavior, with an almost negligible overshoot, and short settling time.

Another KPI for motion controllers is the rise time. The rise time can be defined as the time it takes for the controller to reach its maximum point. In this case, using Figures 6.5 and 6.18, the rise time is defined as the time it takes for the controller to reach the desired value for the depth for the first time. With the MPC controller, it takes 286 seconds before the actual depth reaches the desired reference depth for the first time in the simulation, while the PID controller needs 200 seconds. From this time, it can be concluded that the MPC controller reacts somewhat slower. Besides this rise time, the MPC controller outperforms the PID controller based on the KPIs from Table 6.8, considering the settling time and overshoot, and the corresponding energy requirements.

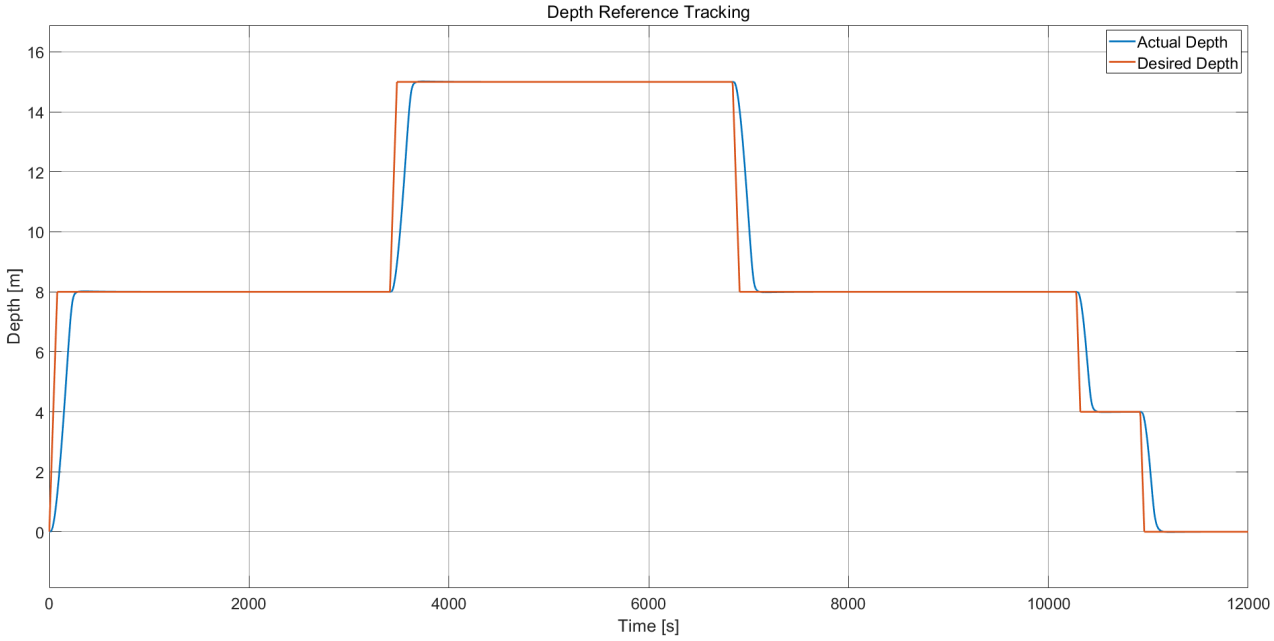

Figure 6.18: Depth Reference Tracking MPC Controller

Table 6.8: Manual tuned PID controller performance for the depth

Depth Controller Performance	
Maximum Overshoot [m]	0.0154
Maximum Overshoot [%]	0.1 %
Settling Time [s]	620

The required energy and maximum power for the DCT, using the MPC controller, can be seen in Table 6.9. These values can also be found in Figures 6.19, 6.20, 6.21, and 6.22. Similar as for the results from the PID controllers, the output from the MPC controller is the required mass in the DCT. This mass is differentiated to get the required mass flow, over the complete simulation time. The mass flow rate is used as input to calculate the required pump power, for both the pump system and the compressed air system. The required power is integrated over time to calculate the total amount of energy, required for the reference tracking. The figures will be explained in more detail below.

Table 6.9: MPC Energy requirements for DCT

		DCT
Pump System	Maximum Power [kW]	47
	Energy [kJ]	5314
	Energy [kWh]	1.47
Compressed Air System	Maximum Power [kW]	23
	Energy [kJ]	16752
	Energy [kWh]	4.7

In Figure 6.19, the required mass to be added or removed from the DCT can be seen. Similar as for the situation with the PID controller, mass can be added or removed from the tank in order to generate the required heave forces in upward or downward direction. Different compared to Figure 6.6 from the PID controller is the maximum added (and removed) mass from the tank, as well as the larger peaks in negative mass (e.g. larger upward forces). These larger upward heave forces, in combination with the linear damping in heave direction, force the ALERD to slow down faster compared to the PID controller, resulting in almost no overshoot. Although no hard constraints are put on the minimum and maximum mass, the optimal solution of the controller is to constrain the mass on $+/-1500kg$, also taking into

account the energy consumption. The mass is differentiated to obtain the required mass flow during the complete simulation.

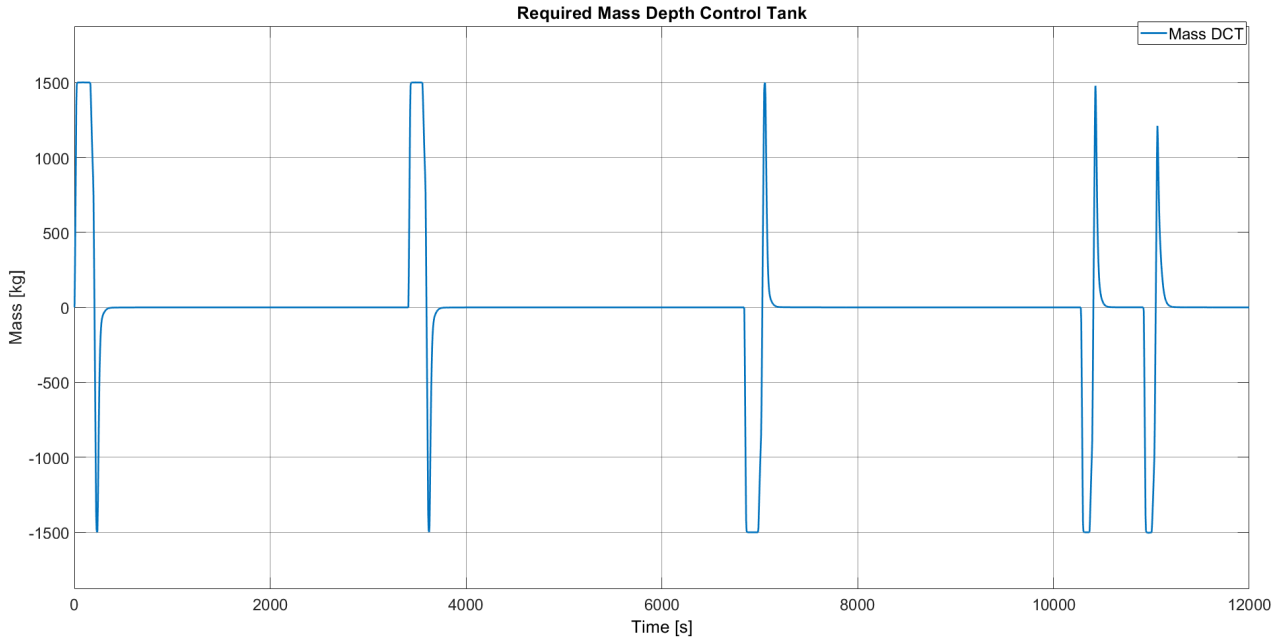

Figure 6.19: Required mass DCT

In Figure 6.20, the required negative mass flow is plotted, used for calculating the required pump power. The required pump power can be found in Figure 6.21. The corresponding energy requirements for the pumps in kWh can be found in Figure 6.22. A detailed comparison of the results from both the MPC and PID controllers, and the corresponding energy requirements, will be made in Section 6.3.

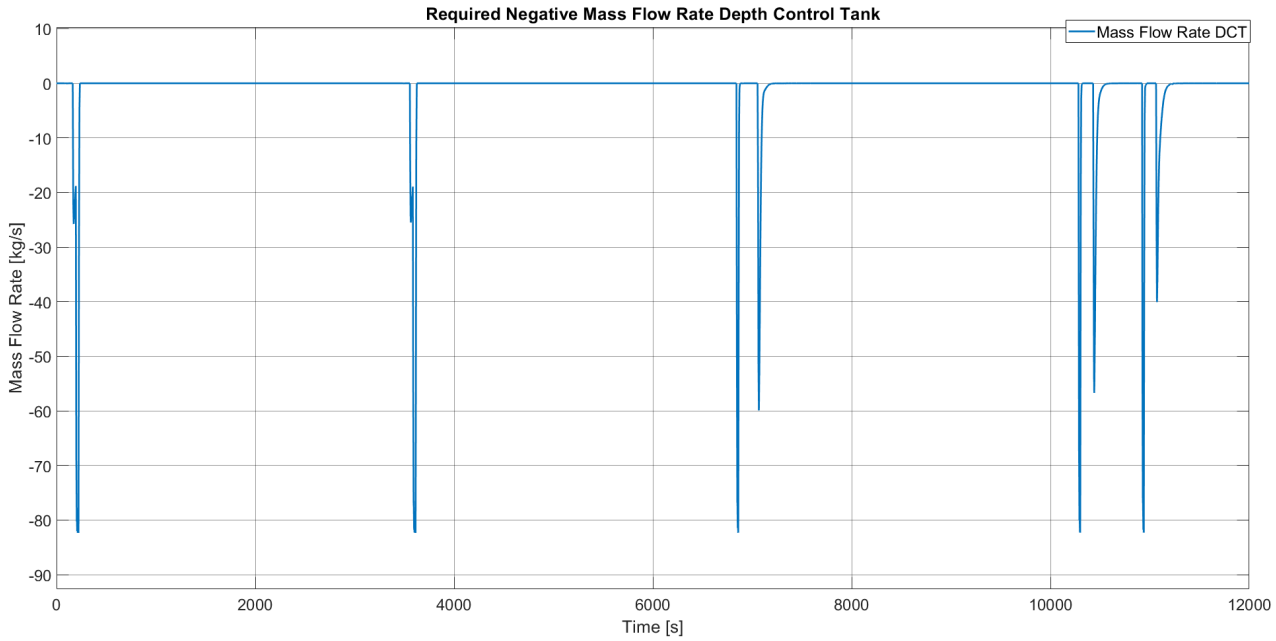

Figure 6.20: Required mass flow DCT

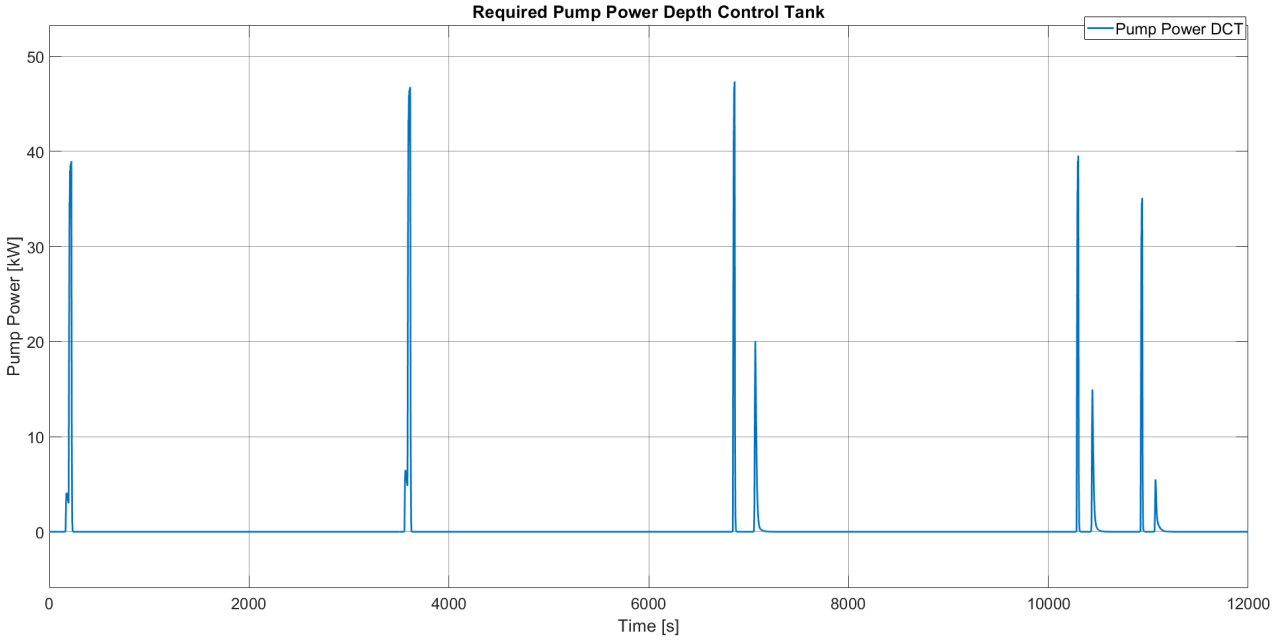

Figure 6.21: Required pump power DCT

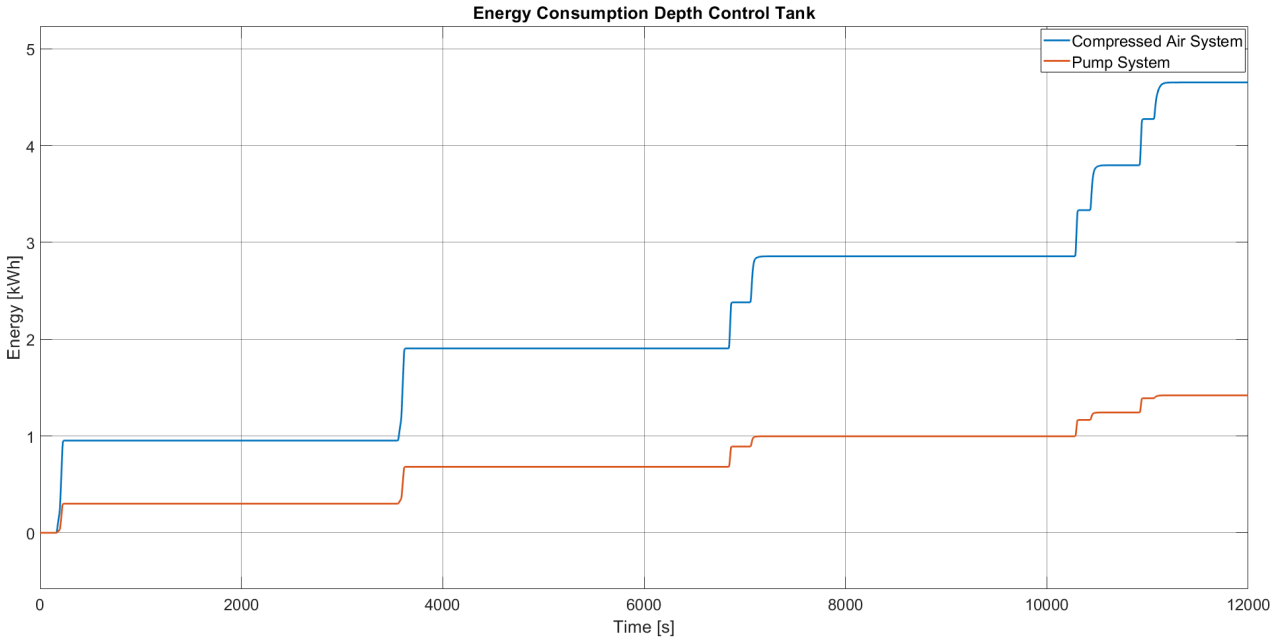

Figure 6.22: Depth Reference Tracking MPC Controller

Trim Tank System

In Table 6.10, the energy requirements, corresponding to the pitch angle reference tracking using the MPC controller, can be found. In Figure 6.23, the result of the MPC controller for the pitch angle θ is plotted. Similar as for the PID controller, the reference for the pitch angle is zero degrees at all times. From Figure 6.23 it can be seen that small deviations occur, with a maximum deviation of $\approx 0.25^o$. Using the length of the ALERD of 80 meters, a trim angle will result in a height difference of 17 centimeters, with respect to the CO. This difference can be considered negligible. Comparing Figure 6.23 with the results of the PID controller for the pitch in Figure 3.2, it can be concluded that the deviations from the reference signal are higher for the MPC controller. The peak values occur at approximately the same time instant, which is the moment when the dredging operation starts and ends. A detailed comparison

between the results from the PID controller and the MPC controller will be made in Section 6.3.

Table 6.10: MPC Energy requirements for the trim tank system

		TT
Pump System	Maximum Power [kW]	100
	Energy [kJ]	929
	Energy [kWh]	0.26

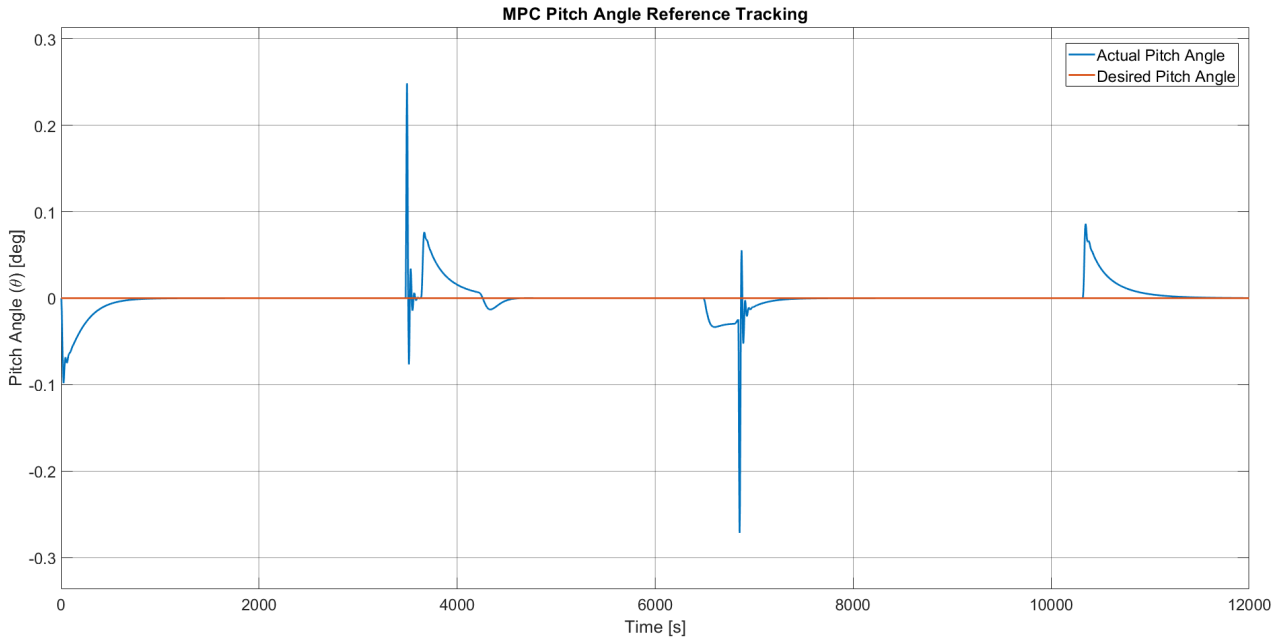

Figure 6.23: Pitch Reference Tracking MPC Controller

In Figures 6.24, 6.25, 6.26, and 6.27, the trimming moments, the mass in the forward trim tank, the mass flow for the forward trim tank, and the corresponding energy requirement for the pump can be found, respectively. The approach to calculate the energy requirements for the trim tank system, in kW, kJ and kWh, are similar as described in Section 6.2.1, and will not be repeated here.

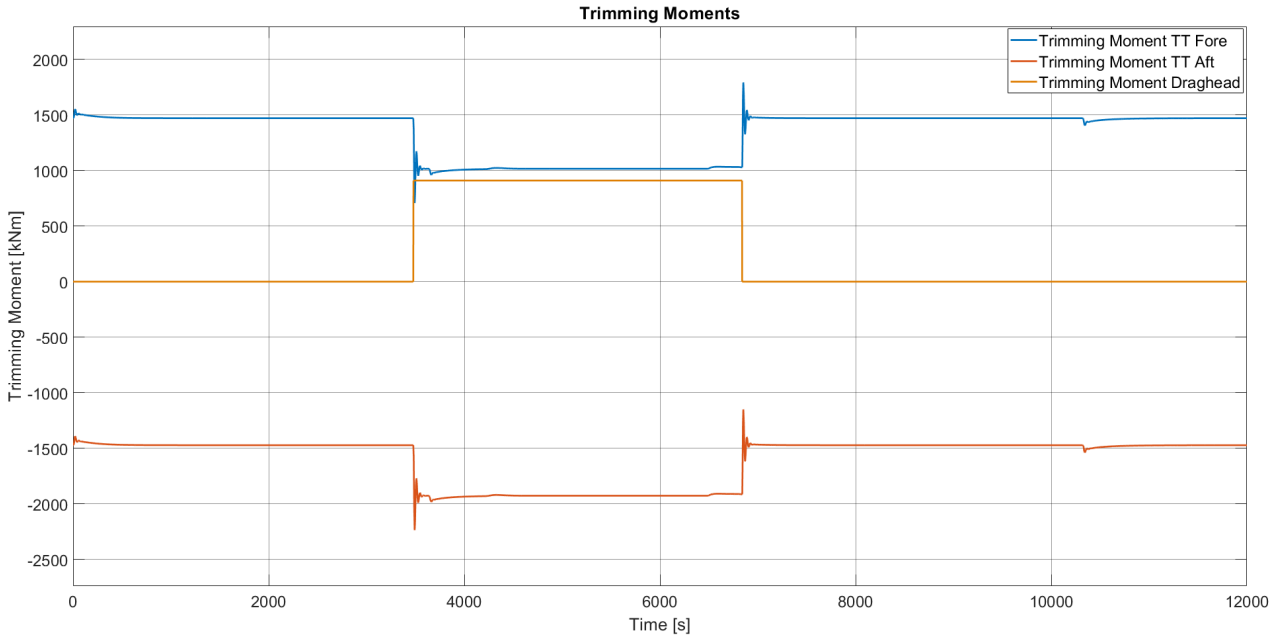

Figure 6.24: Trimming moments MPC Controller

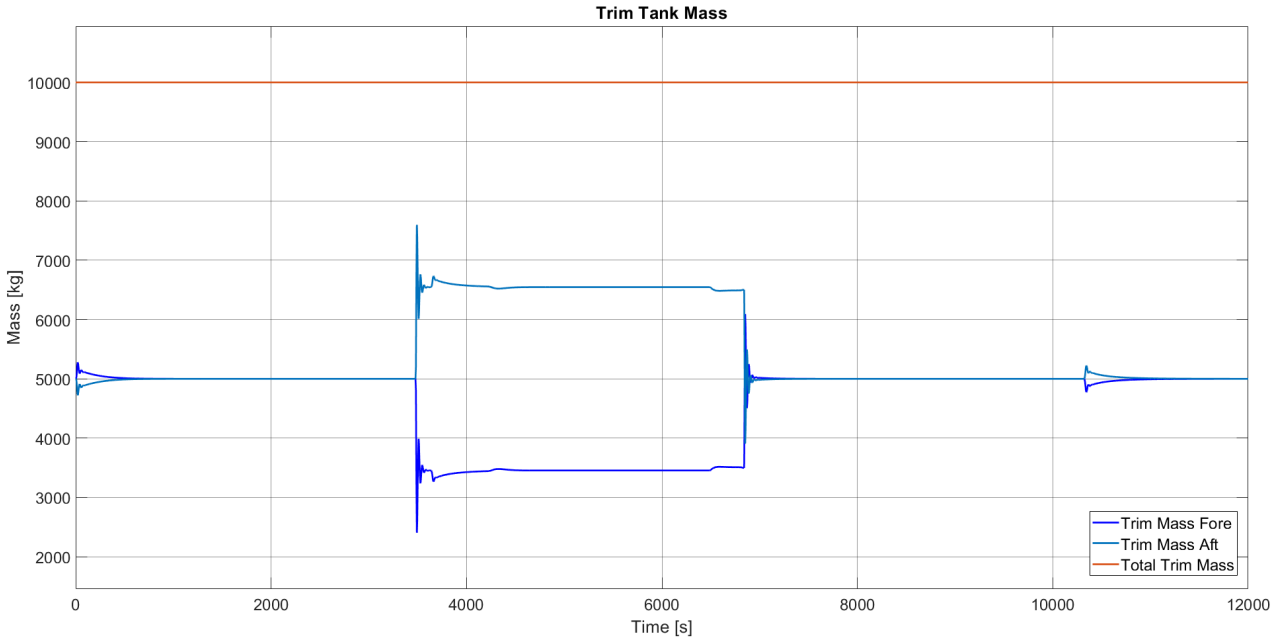

Figure 6.25: Ballast mass in trim tank system

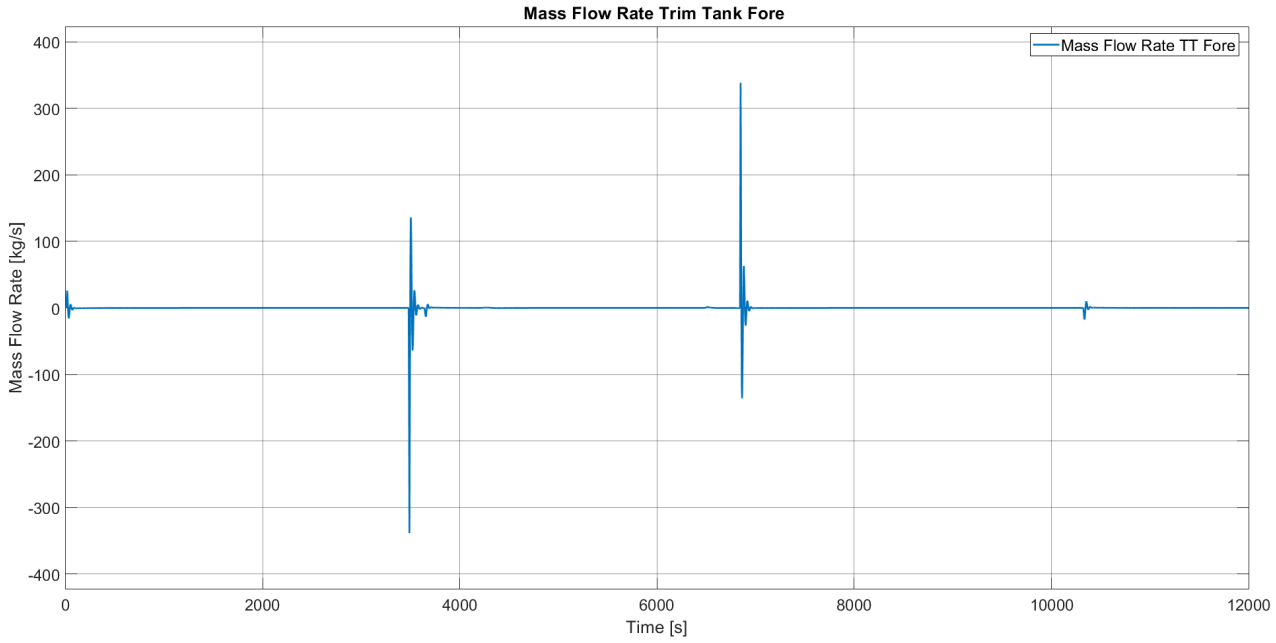

Figure 6.26: Required mass flow trim tank fore

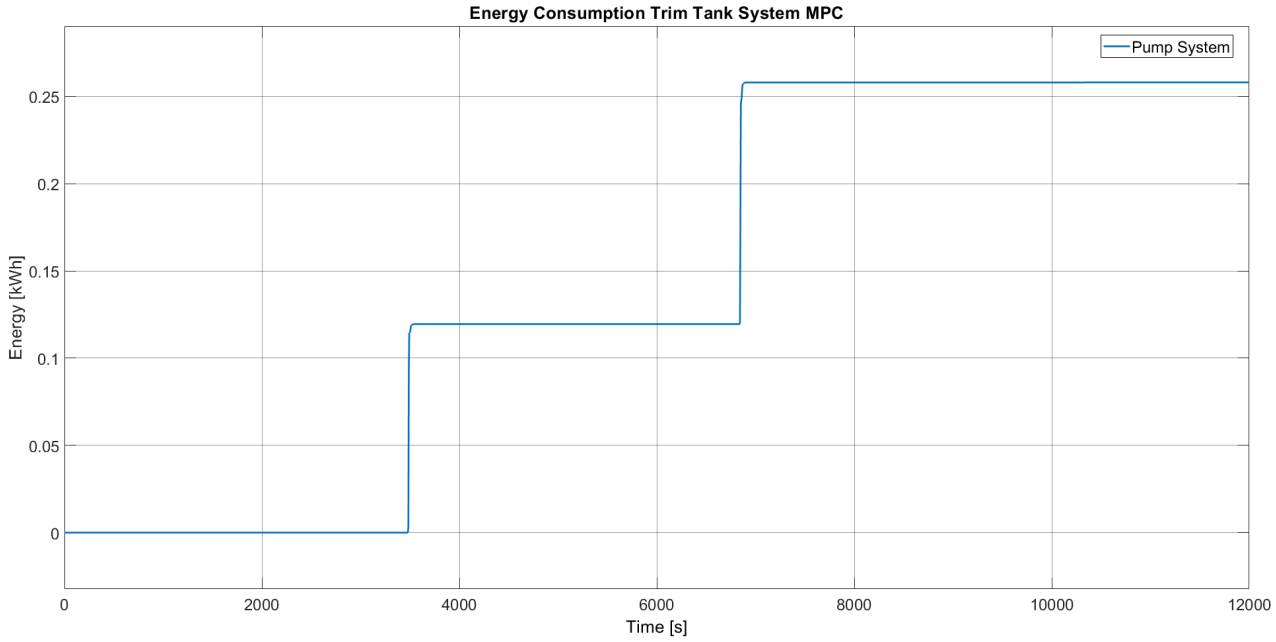

Figure 6.27: Energy consumption for the trim tank system

6.3. Comparison and Conclusion

In this section, the results from the MPC and PID controllers for the depth and pitch angle will be compared, looking at both the controller performance and energy requirements. In Table 6.11, the results from the PID controllers and MPC are compared. It is clear to see that MPC shows the overall best performance, based on both the energy requirements for the depth and pitch reference tracking, as well as on controller performance KPIs such as the overshoot and settling time.

Table 6.11: Comparison MPC and PID controllers

		PID	MPC	Difference
Depth Control	**Maximum Power [kW]**	46	47	+2%
	Energy [kWh]	1.98	1.47	-26%
	Overshoot [m]	0.879	0.0154	-98%
	Settling Time [s]	2129	620	-70%
	Rise Time [s]	200	286	+43%
Pitch Control	**Maximum Power [kW]**	201	100	-50%
	Energy [kWh]	0.40	0.26	-35%
	Maximum Deviation [deg]	0.12	0.27	+131%

The PID controller has a faster rise-time when controlling the depth, indicating that the controller response is faster. However, this results in a significant overshoot, compared to the MPC controller. The MPC controller has the best controller performance, while minimizing the corresponding energy requirements. The MPC controller outperforms the PID controller with reference tracking of the desired depth signal, which can be concluded when comparing Figure 6.5 with Figure 6.18. Those two figures are combined in Figure 6.28.

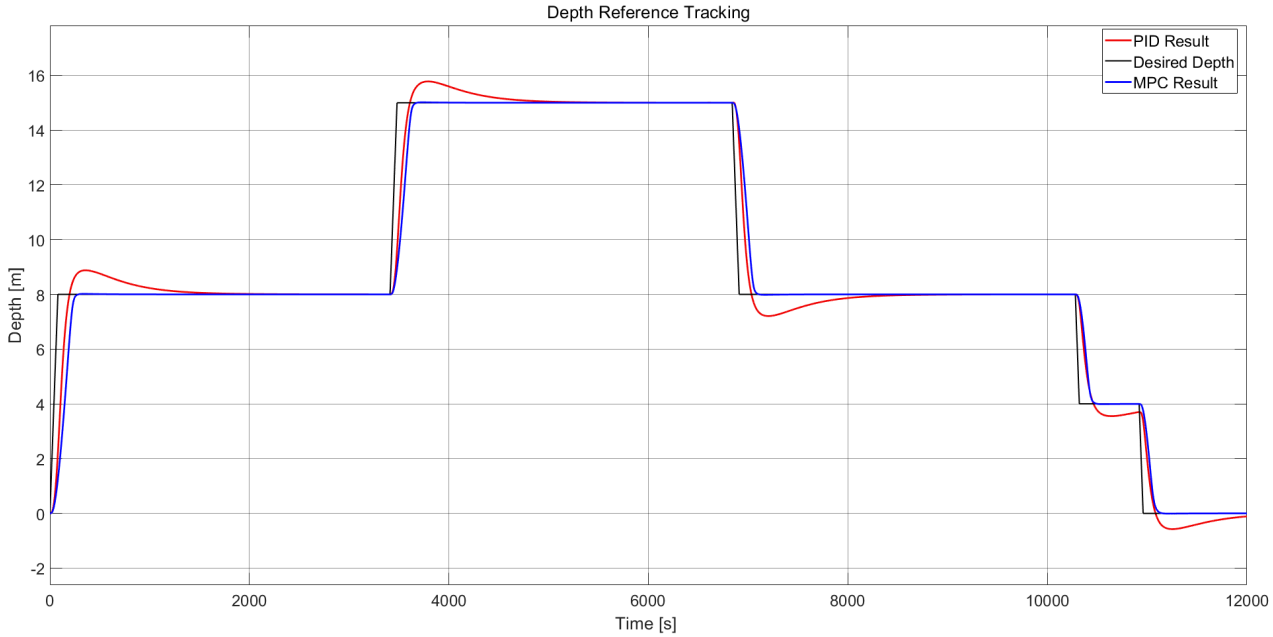

Figure 6.28: Comparison PID and MPC for depth control

The performance of the reference tracking can be explained looking at Figure 6.29, where Figure 6.6 and 6.19 are combined. The MPC controller requires more negative mass, i.e. ballast mass removed from the tanks. Removed ballast mass leads to a negative upward force, which decelerates the ALERD during the descending phase, leading to a smaller vertical velocity. If the ALERD is rising, the controller requires at a certain moment more added ballast mass in the tanks, which again decelerates the motion, reducing the overshoot of the desired signal. The vertical movement during the descending (or ascending) is slowed down more aggressively by the MPC controller, leading to almost no overshoot, while optimizing the control outputs. This combination leads to almost perfect reference tracking, while at the same time minimizing the energy requirements, since the minima and maxima of the required mass are lower, and the duration of the maximum mass flow rate is shorter.

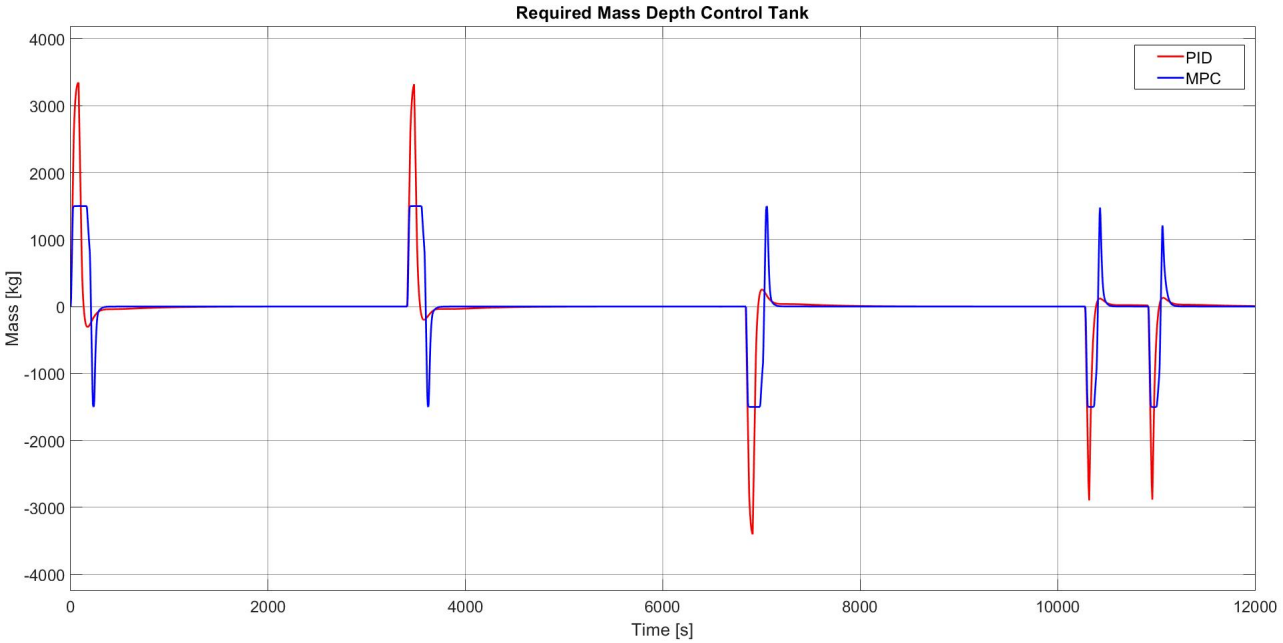

Figure 6.29: Comparison of the required DCT mass for PID and MPC

The effect of the added and removed mass in the DCT on the vertical heave velocity w can be seen in Figure 6.30. The vertical velocity for the PID controller is higher and for a longer period during the peaks, which lead to the overshoot of the desired depth. For the MPC controller, this velocity is smaller, due to the ”braking” effect of the mass in the DCT. Therefore, the output of the MPC controller enables the ALERD to perform a better reference tracking, compared with the PID controller.

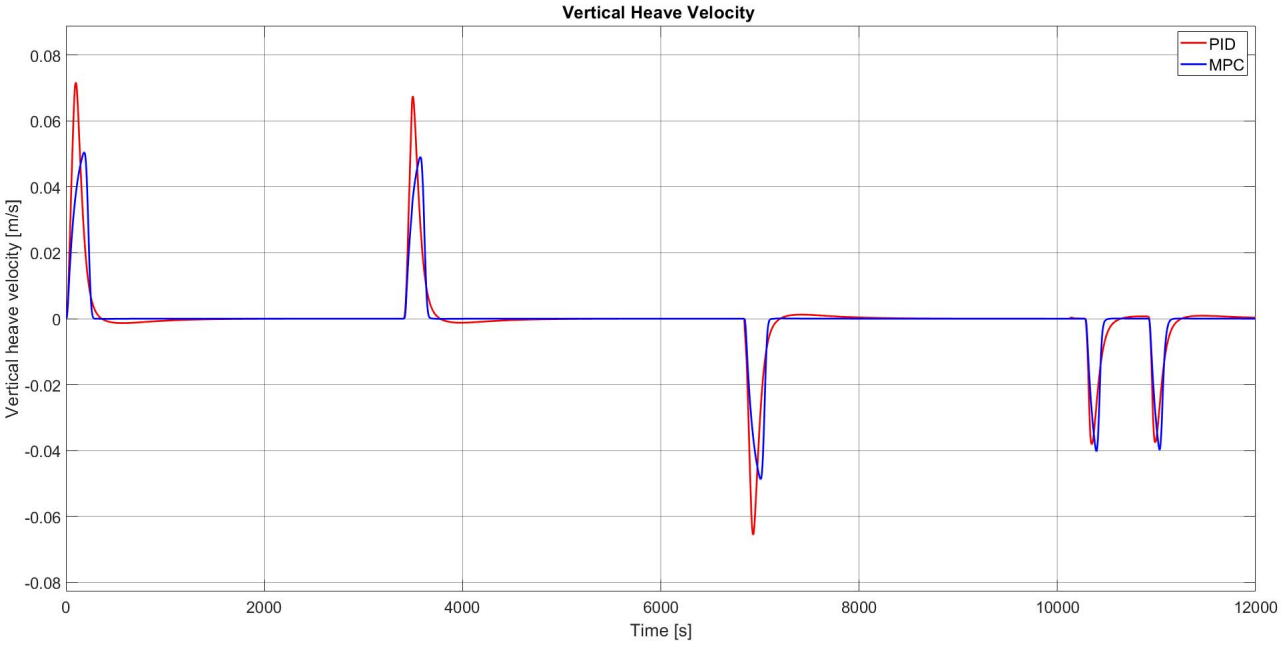

Figure 6.30: Comparison of the heave velocity for PID and MPC

The decrease in energy requirements using MPC is shown in Figure 6.31. The MPC optimizes the control effort, by decreasing the duration of the maximum mass flow rate. If the maximum mass flow rate is required for a shorter period of time, the corresponding maximum power and thus the required energy decreases, which can be concluded from Figure 6.31, where it is shown that using MPC decreases the required energy for depth control.

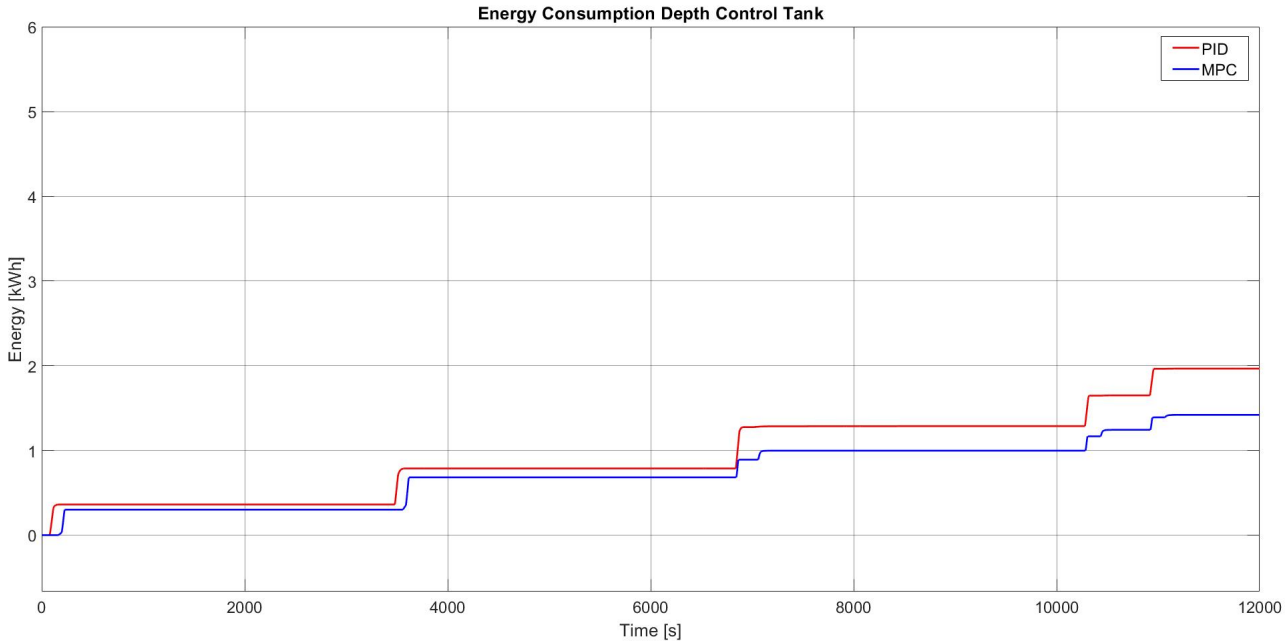

Figure 6.31: Comparison of the DCT energy consumption for PID and MPC

When comparing the results for the pitch controller, it can be seen from Table 6.11 that the energy requirements are almost twice as low for the MPC controller. The maximum deviation from the reference signal, i.e. the ”overshoot” in pitch angle, is larger for the MPC controller, which is shown in Figure 6.32. However, both maximum deviations are small, and can be considered negligible. Furthermore, the angles are so small and occurring at small-time intervals, it is questionable whether these small deviations in pitch angle occur in reality. Especially taking into account all the environmental disturbances, and imperfect loading conditions of the hopper, which occur in real life.

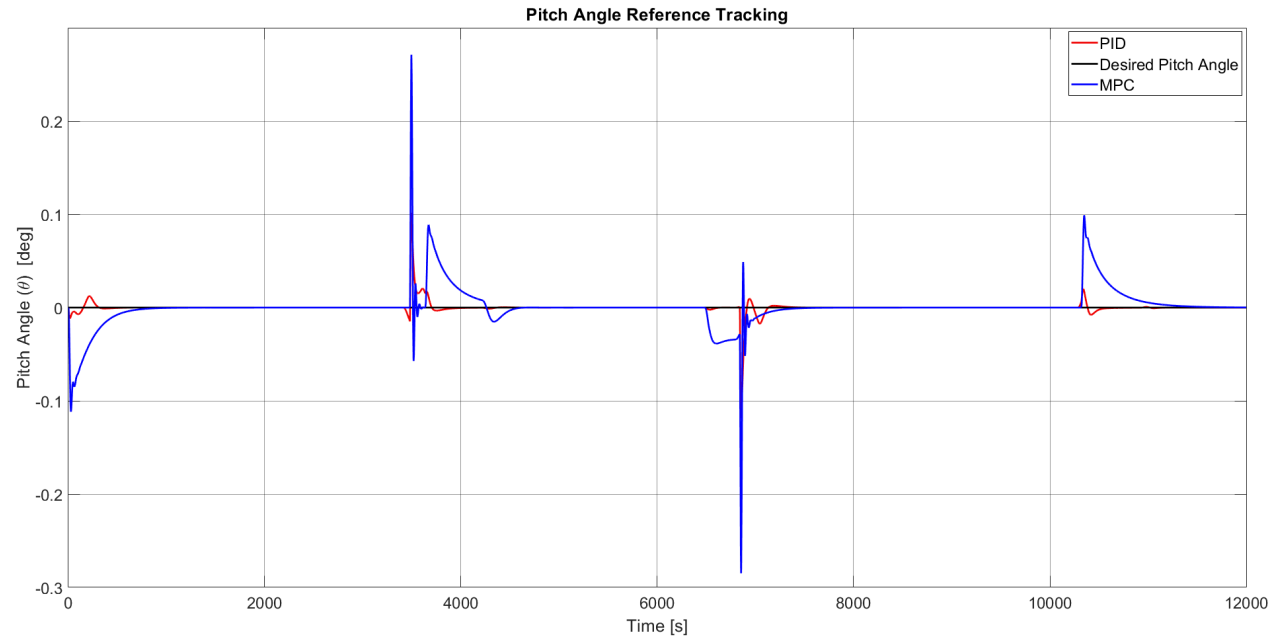

Figure 6.32: Comparison PID and MPC for pitch control

The energy consumption is minimized using MPC, which can be explained looking at the required mass flow rate from Figure 6.33 and the corresponding energy requirements, shown in Figure 6.34. The peaks of the maximum values for the mass flow rate are smaller using MPC, and therefore decreases

the energy consumption. By changing the weights in the cost-function, reference tracking could be prioritized more, leading to more aggressive control moves and a higher energy consumption. Since the maximum deviation for MPC is considered to be negligible, it can be concluded that the current designed MPC controller shows sufficient performance, reducing the required energy while having a negligible deviation in the pitch angle.

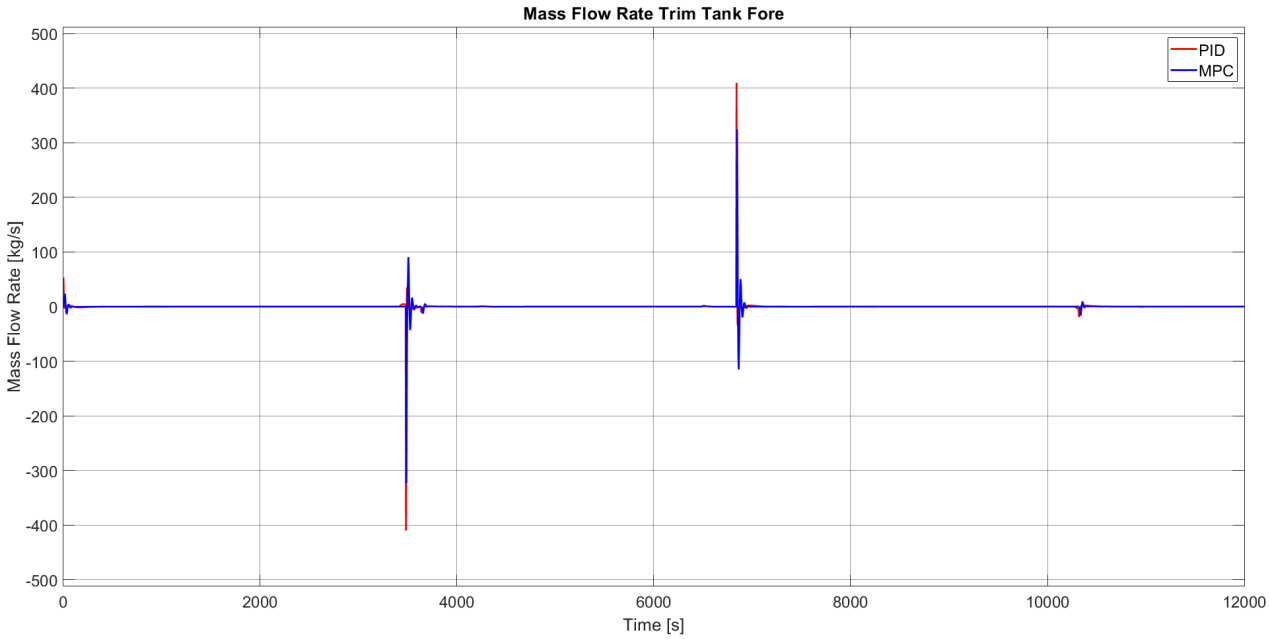

Figure 6.33: Comparison of the required TT mass flow rate for PID and MPC

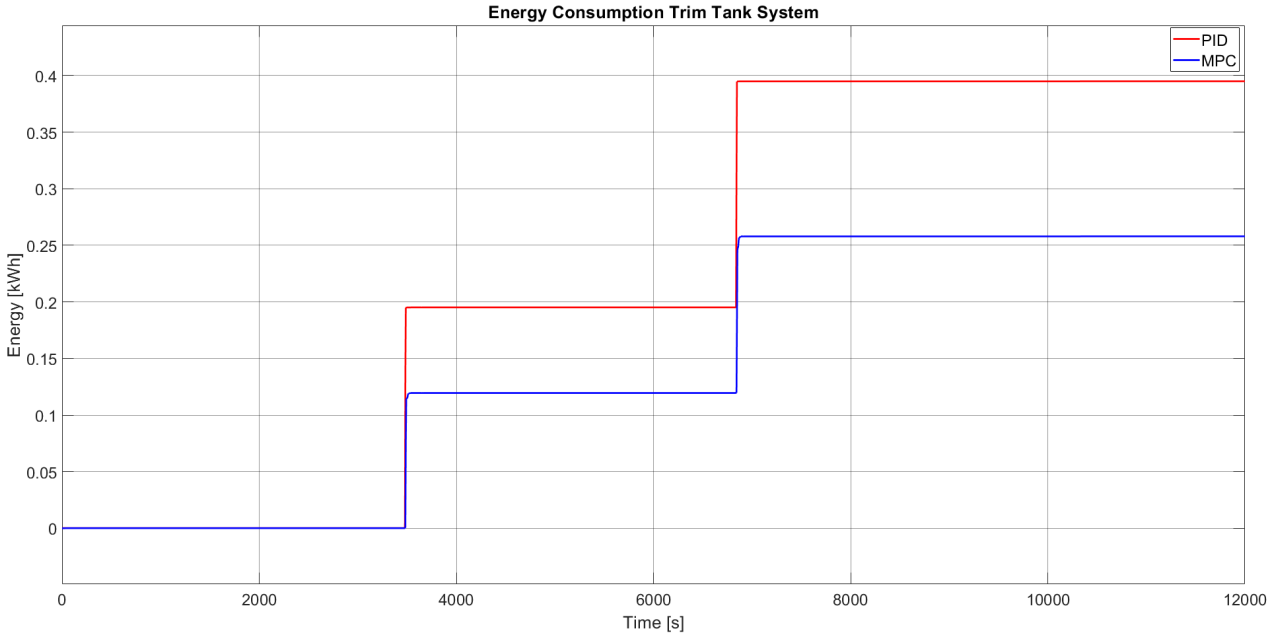

Figure 6.34: Comparison of the TT energy consumption for PID and MPC

Based on the comparison made in this section, it can be concluded that the MPC controller is outperforming the PID controllers. In Table 6.11, it is clear to see that MPC has the better overall performance, looking at the different KPIs. It shows better controller performance, while minimizing the control effort, which directly influences the energy requirements for the physical systems. In Chapter

7, it will be shown how both controllers are performing when taking into account uncertainty in input parameters of the simulation model. Based on the comparison in this section, and the results from the Monte Carlo Simulations, a final conclusion can be made for which controller is the best choice for controlling an underwater vehicle, which is mathematically modelled in a time-domain simulation model.

6.3.1. Comparison ALERD and Conventional Dredger

With the outcomes of the simulation model using MPC for the energy requirements of the DCT and TT, and the energy requirements for the MBT, the amount of energy per cubic meter soil mixture can be calculated and compared with a conventional dredger for the operational profile defined in Chapter 3.

In [10], a comparison is made between the total energy requirements for a conventional dredger and the ALERD. A conventional TSHD is used as reference ship to compare with, which can be found in Figure 6.35. This dredger is designed by C-Job, so the energy requirements for propulsion, dredging, and discharging are already known. Originally, the hopper of the reference dredger from Figure 6.35 has a capacity of 3600 cubic meters. The general arrangement plan, as well as the original dimensions of the dredger, can be found in Appendix **??**. The required power for transit, dredging, and discharging from the reference dredger is scaled to a hopper capacity of 2500 cubic meters, since this corresponds to the hopper capacity of the ALERD used in [10].

Figure 6.35: Conventional dredger used as reference ship

In Table 6.12, the results of the comparison can be seen. For the ALERD and the conventional hopper, the dredging depth, the operational profile, and the hopper volume are similar. The operational profile used in this research and defined in Chapter 3 is based on the previous studies ([10], [11]) and can be considered similar to the operational profile used to determine the energy requirements for the conventional dredger. There is however a small difference in total duration of the operational profile, due to the reduced transit speed of the ALERD of 8.5 knots used in this research.

In Table 6.12, it can be seen that there is a clear decrease in energy consumption, comparing the conventional dredger and the ALERD. The results in Table 6.12 are based on a similar operational profile for both vessels, which is one complete dredging cycle, including transit, dredging, and discharging. In [10], the energy requirement for a compressed air system used to empty the tanks during the dredging and discharging operation is included, which is equal to $0.16kWh/m^3$. This however is seen as a rough first estimation, without detailed analysis of the compressed air system and time-domain simulations using motion control. Therefore, this contribution of $0.16kWh/m^3$ is subtracted from the total energy consumption, resulting in an energy requirement of $1.09kWh/m^3$. The energy requirements for stability and buoyancy control, which are a result of this research, are added to this energy requirement

to obtain the total energy requirements again.

Table 6.12: Comparison energy requirements for conventional dredger and the ALERD [10]

	Conventional Dredger	ALERD	Unit
Hopper volume	2500	2500	m^3
Required power for transit	2074	660	kW
Required power for dredging	5899	1970	kW
Required power for discharging	2849	1050	kW
Total duration	155	163	min
Total energy consumption	3.75	1.25	kWh/m^3

In Table 6.13, the results for the different tank systems using a ballast water pump system are listed. These values are the result of using MPC for controlling the depth and pitch angle. In this research, the used hopper volume is equal to 2360 cubic meters (instead of the 2500 cubic meters used in the comparison), which is based on a previous study [17]. Besides the difference in hopper volume, the comparison is made as fair as possible, using the similar operational profile for one complete dredging cycle. From Table 6.13 it can be seen that the required energy for stability and buoyancy control for the specific operational profile defined in Chapter 3 is equal to $0.17kWh/m^3$, leading to a total energy consumption of $1.26kWh/m^3$ for the ALERD. It can be concluded that for this specific operational profile, the required energy for stability and buoyancy has a contribution of 16% of the total energy consumption for the ALERD.

Table 6.13: Energy consumption for the ALERD

	ALERD	Unit
Hopper volume	2360	m^3
MBT energy consumption	408	kWh
DCT energy consumption	1.47	kWh
TT energy consumption	0.26	kWh
Energy consumption stability and buoyancy control	0.17	kWh/m^3
Total energy consumption ALERD	1.26	kWh/m^3

Using the results from Table 6.12 and 6.13, a comparison can be made between the conventional dredger and the ALERD for this specific operational profile. The results of the comparison can also be found in Table 6.14. It can be seen that, using the results from this chapter, 66.4% of energy is saved compared to a conventional dredger.

Table 6.14: Energy requirements ALERD vs conventional dredger

	Conventional Dredger	ALERD	Difference
Total Energy Requirements	3.75 kWh/m^3	1.26 kWh/m^3	-66.4 %

Based on the results in Table 6.14, it can be concluded that submerged dredging is more energy efficient compared with conventional dredging, considering the defined operational profile, which is similar for both the conventional dredger and the ALERD. However, it must be noted that the results in this research are calculated assuming perfect loading and unloading conditions of the hopper, and without taking into account environmental disturbances. It is expected that adding these additional disturbances can lead to an increase in energy requirements.

Nevertheless, it is proven that submerged dredging has potential and can replace conventional dredgers in the future. The simulation model is structured in such a way that environmental disturbances can be included, and the remaining uncontrolled DoF such as the roll motion can easily be included and controlled.

7

Sensitivity Analysis

In this chapter, Monte Carlo Simulations are performed, using both the PID and MPC controller. With the Monte Carlo Simulations, uncertainty in the mathematical modelling of an underwater vehicle is implemented into the simulation model. The Monte Carlo simulation is used to assess the effects of uncertainties on the model inputs on the outcomes of the simulation model, and to assess the performance of the controllers. A comparison is made between the two different motion control methods, based on their performance, and based on the outcomes of the simulation model, taking into account the modelling uncertainties.

7.1. Uncertainty in Modelling Parameters

In the simulation model, the ALERD is modelled as an underwater vehicle using multiple assumptions, such as the ellipsoidal hull form when calculating the added mass, or the scaled linear damping coefficients. Therefore, there is a certain level of uncertainty around the used coefficients, which can possibly affect the outcomes, both in terms of controller performance, and the energy requirements.

Monte Carlo simulations can be used to give a certain level of confidence for the outcomes of the simulation model, taking into account the uncertainty around the used coefficients. Furthermore, the controller performance can be checked, looking at different controller KPIs such as the overshoot, settling time, and maximum error.

The coefficients which will be random distributed are listed below. The four coefficients are chosen based on their contribution to the equations of motion and their uncertainty. The two main control objectives are pitch and depth control, and the chosen coefficients are within the equations of motion in these two DoF. Changing added mass or damping coefficients will affect the resulting motions in these directions, and are therefore useful to show the performance and robustness of the controller. Furthermore, since the ALERD is modelled as ellipsoid, the calculated values of the moment of inertia are not corresponding to the moment of inertia of the real hull-form.

- Z_w; Linear damping coefficient in heave (z).
- M_q; Linear damping coefficient in pitch (θ).
- $Z_{\dot{w}}$; Added mass coefficient in heave (z).
- I_{yy}; Mass moment of inertia in y-direction.

Two other coefficients, listed below, will also be randomly distributed based on their direct influence on the outcomes of the calculation for the energy requirement. These coefficients are chosen because there is uncertainty in their real value. For (conventional) ships, the value for η_{pump} is in the range of 0.6 - 0.9, and the value of ζ is in the range of 10 - 100. There is no detailed information available for the pumps that will be used, or how the complete lay-out of the pipeline system onboard the ALERD will look like. Therefore, those two parameters will be normally distributed and randomly picked, to see how this will affect the outcomes of the simulation model.

- η_{pump}; Centrifugal pump efficiency.
- ζ; Resistance factor.

7.2. Normal Distribution

In Section 7.1, the different coefficients that will be normal distributed are listed. A random variable X is normally distributed with a mean μ, and standard deviation σ. This is also shown in Equation 7.1.

$$X \sim \mathcal{N}\left(\mu, \sigma^2\right) \tag{7.1}$$

The random variables are the chosen coefficients, and it is assumed that the mean μ is equal to the actual calculated value. To determine the standard deviation of the normal distributions, it is assumed that the maximum deviation is 20% of the actual calculated value, which in fact is the assumed uncertainty in the calculated value for all the used coefficients. Using this assumption and the characteristics of the normal distribution, the standard deviation can be calculated. Three standard deviations away from the mean account for 99.73% of the dataset, and with using the maximum deviation, the standard deviation can be calculated. This is also shown in Figure 7.1. If for each coefficient the standard deviation and mean are known, the normal distributions can be constructed.

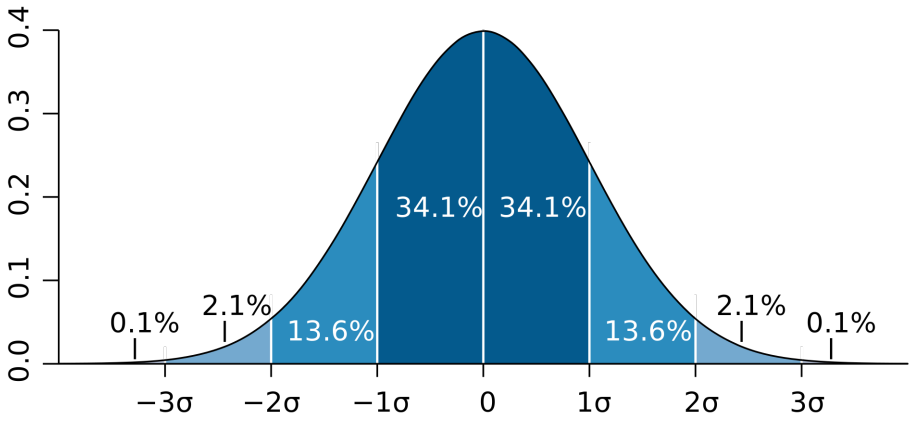

Figure 7.1: Standard Deviation Diagram of a Normal Distribution [26]

7.2.1. Random Normal Distribution for the Chosen Coefficients

The Matlab function *normrnd* is used to generate random numbers from a normal distribution with the known parameters μ and σ. If a large amount of random numbers is generated, a normal distribution can be created. The values for the mean μ and standard deviation σ, for the chosen six coefficients, can be found in Table 7.1. As mentioned above, the standard deviation is calculated using the maximum deviation of 20%, and the original calculated value for the different coefficients is used as the mean value. μ and σ are used to create random normal distributions for the six coefficients using Matlab. 10000 random samples are generated using the function *normrnd*, leading to the distributions shown in Figures 7.2, 7.3, 7.4, 7.5, 7.6 and 7.7. When comparing Figure 7.1 with these, it can be concluded that the amount of 10000 random generated values are sufficient to create a normal distribution for each coefficient.

Table 7.1: Mean and standard deviation of the chosen coefficients

	Z_w [N/(m/s)]	M_q [Nm/(rad/s)]	$Z_{\dot{w}}$ [kg]	I_{yy} [kgm^2]	η_{pump} [-]	ζ [-]
Mean μ	$2.54 \cdot 10^5$	$1.35 \cdot 10^8$	$9.7 \cdot 10^6$	$3.6 \cdot 10^9$	0.725	70
Standard Deviation σ	$1.69 \cdot 10^4$	$9.02 \cdot 10^6$	$6.46 \cdot 10^5$	$2.4 \cdot 10^8$	0.048	4.67

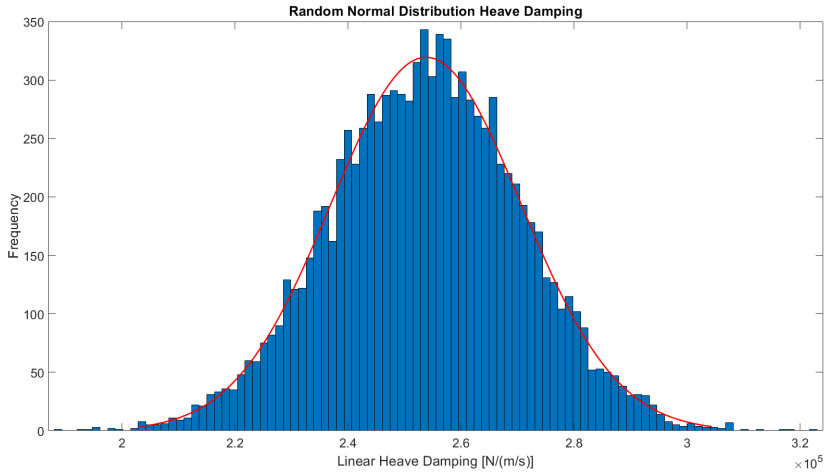

Figure 7.2: Random normal distributed heave damping Z_w

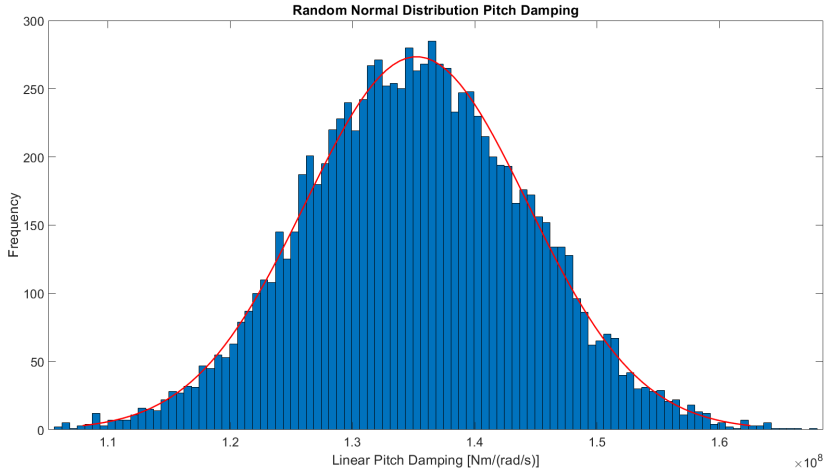

Figure 7.3: Random normal distributed pitch damping M_q

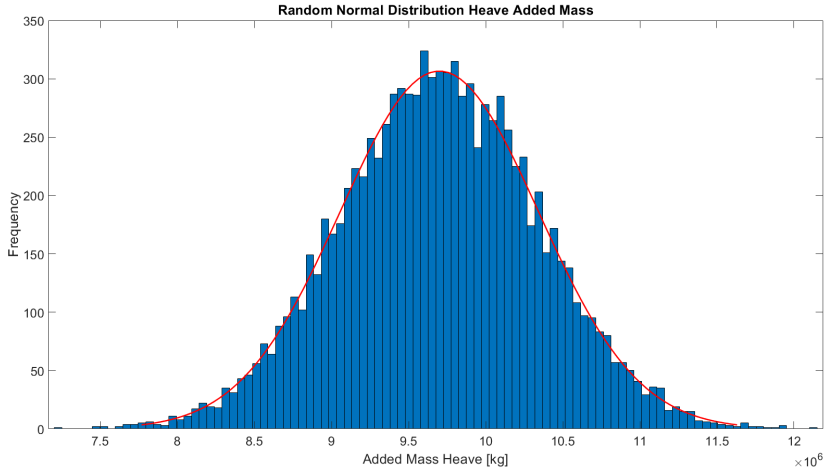

Figure 7.4: Random normal distributed added mass in heave $Z_{\dot{w}}$

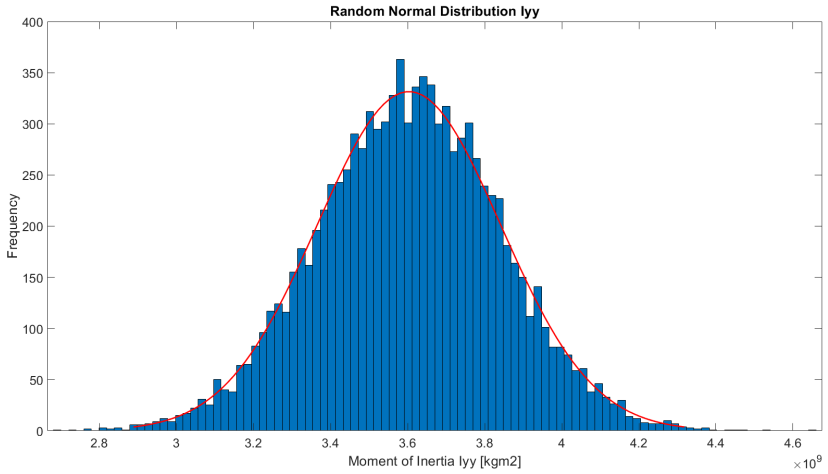

Figure 7.5: Random normal distributed moment of inertia I_{yy}

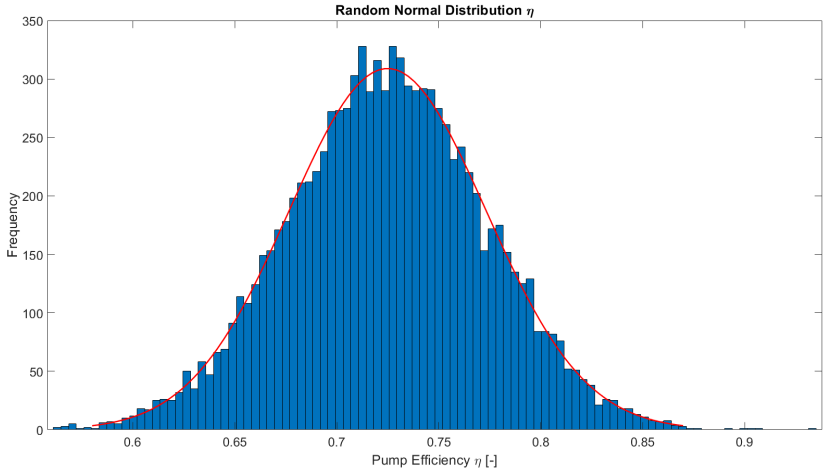

Figure 7.6: Random normal distributed pump efficiency η_{pump}

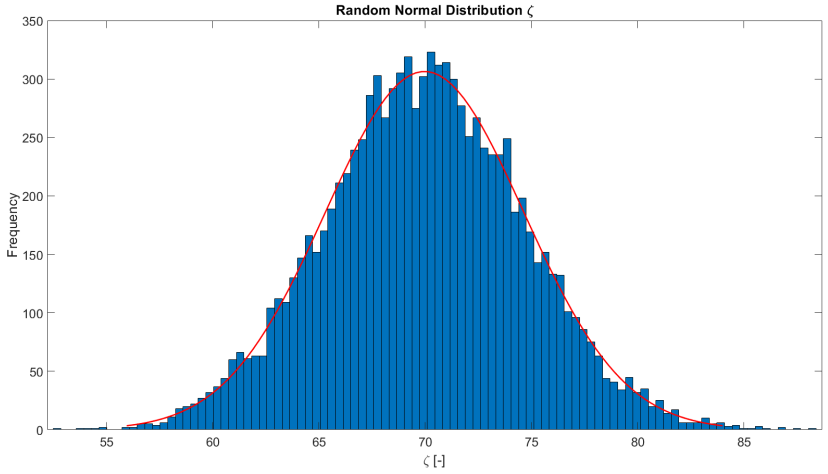

Figure 7.7: Random Normal Distributed ζ

The generated random normal distributions will be used to pick a smaller sample size from, which is used as input for the simulations. It is chosen to use a sample size of 1000, meaning that from the distributions in Figures 7.2 to 7.7, 1000 random values will be picked for each coefficient. The number of simulations for the Monte Carlo Simulation is equal to the sample size, i.e. 1000. By picking 1000 random samples of the generated random normal distributions, a set of 1000 unique combinations of the six coefficients is generated, which serves as input for the simulation model. If the sample size is large enough, the results of the 1000 simulations will also be normally distributed [5].

7.3. Confidence Intervals for the Mean

For each simulation done with a unique combination of random generated coefficients, the outcomes of the model will be different. Since 1000 simulations will be carried out, the outcomes will also have a probability density function. The real values of the solution of the simulation model are unknown, i.e. it cannot be said that the outcome from the simulation model of the energy requirements for the DCT is the true value.

To be able to say something about the solutions, confidence intervals can be created. A confidence interval is a range of values for an unknown parameter, which can be used to show that the true value of the parameter falls within this range with a certain level of confidence. This confidence level is something that can be chosen, and the most common and accepted confidence level is 95% [5].

For the random sample, the standard deviation σ and mean μ are unknown parameters. To construct the confidence interval, the Student's t-distribution can be used. The corresponding confidence interval of the Student's t-distribution can be seen in Equation 7.2, with confidence level $100(1-\alpha)\%$. If the confidence interval is 95%, $\alpha = 0.05$.

$$\left(\bar{x}_n - t_{n-1,\alpha/2}\frac{s_n}{\sqrt{n}}, \bar{x}_n + t_{n-1,\alpha/2}\frac{s_n}{\sqrt{n}}\right) \tag{7.2}$$

In this equation, $\bar{x_s}$ is the sample mean, s_n^2 is the sample variance, and n is the sample size. $t_{n-1,\alpha/2}$ can be determined using the t-distribution and the sample size n. The sample mean and variance can easily be determined using the sample data. With Equation 7.2, it can be said that the true value of the sample mean falls within the specified range with a certain level of confidence.

7.4. Analysis of the Results

The results of the Monte Carlo Simulation will be used to construct confidence intervals for the solutions of the simulation model, which are the energy requirements for the different tank systems. It is chosen to evaluate the systems that are directly linked with the output of the motion controllers, which are the trim tank system, and the depth control system. The outcomes for the required power and the energy consumption for the TT and DCT are a direct result of the controller performance, and are directly affected by the six random and normal distributed coefficients. Furthermore, the performance of the controller will be assessed taking into account the modelling uncertainty.

7.4.1. Monte Carlo Simulation Using PID Control

In Figure 7.8, the results of the 1000 simulations, for the DCT and TT energy, can be found. It is clear to see that they are both normally distributed. Using the data from Figure 7.8, a confidence interval for the mean value of the energy requirements for both the DCT and TT can be constructed, using Equation 7.2.

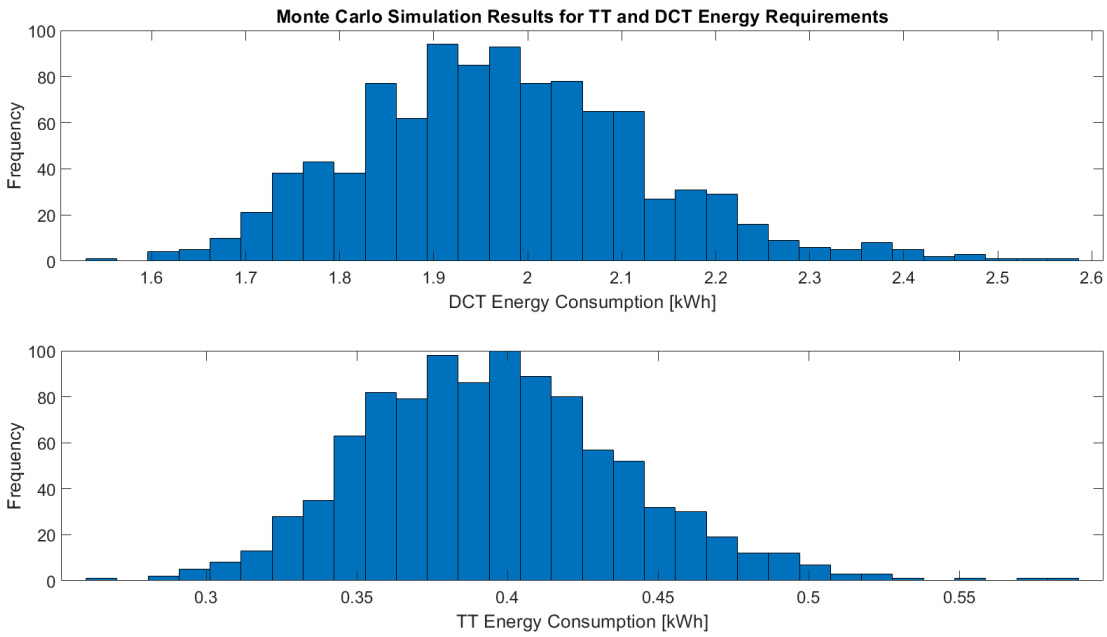

Figure 7.8: Monte Carlo Simulation results for DCT and TT energy requirements using PID

The value of $t_{n-1,\alpha.2} = 1.9623$, and is obtained by using the build in Matlab function for the Student t-distribution. The sample mean and sample standard deviation can be calculated using the sample data, plotted in Figure 7.8, and are listed in Table 7.2. The resulting confidence intervals for the mean value of the DCT energy consumption and TT energy consumption can also be found in Table 7.2

Table 7.2: Statistics of the energy requirements and controller performance using PID control

	DCT Energy [kWh]	**TT Energy [kWh]**	**Overshoot [m]**
Sample Mean $\bar{x_n}$	1.9742	0.3960	0.7935
Sample Standard Deviation s_n	0.1550	0.0435	0.0403
$\pm t_{n-1,\alpha.2} \cdot \frac{s_n}{\sqrt{n}}$	0.0096	0.0027	0.0025
95% Confidence Interval	1.9742 ±0.0096	0.3960 ±0.0027	0.7935 ±0.0025
95% Confidence Interval Range	[1.9645, 1.9838]	[0.3933, 0.3987]	[0.7910, 0.7960]

The confidence intervals for the mean value of both the DCT energy requirement, and for the TT energy requirement, are relatively small. With these two intervals it can be said that, with 95% confidence, every simulation using coefficients randomly picked from the normal distributions from Figures 7.2 to 7.7, has an outcome for the energy requirements for the DCT and TT, within the given confidence intervals from Table 7.2.

PID Controller Performance

In Figure 7.9, the overshoot of the actual depth, with respect to the desired depth of 15 meters, is plotted. The results for the overshoot statistics can be found in Table 7.2, where it can be seen that the sample mean of the overshoot is 0.79 meters. The range of values of the overshoot is between $[0.711, 1.0272]$, where in general the modelled uncertainty will lead to more overshoot, since the values are not completely symmetrical distributed around the mean value, as there can be some divergent points observed in Figure 7.9.

From the range of overshoot values, in combination with Figure 7.9, it can be concluded that the controller performance in terms of the depth overshoot is not sufficient. Although the confidence interval for the overshoot is relatively small, the majority of data points indicate an overshoot bigger than 0.8 meters, which in the case of the ALERD is too large. A comparison between the performance of the PID controller and MPC will be made in Section 7.5.

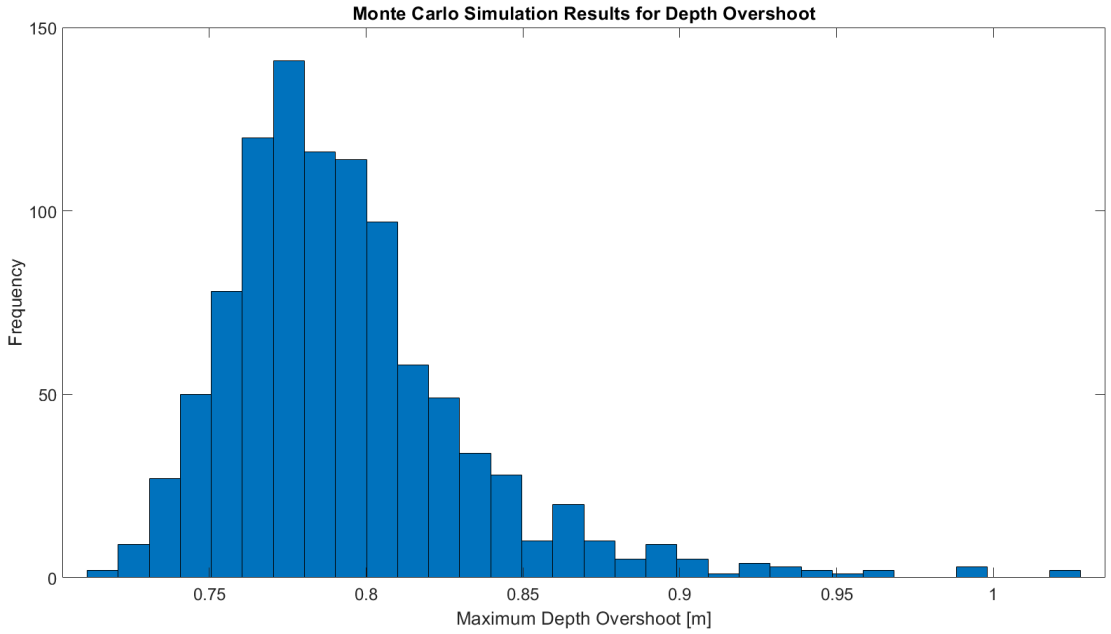

Figure 7.9: Monte Carlo Simulation results for depth overshoot using PID

7.4.2. Monte Carlo Simulation Using Model Predictive Control

95 % Confidence Intervals for the Energy Consumption

In Figure 7.10, the results from the Monte Carlo Simulation using MPC can be found, for both the energy requirements for the DCT and TT. Similar as done in the previous section, 95% confidence intervals are constructed for the mean value of the outcomes of the simulation model, which are the required energy for the DCT and TT respectively, and for the controller KPIs. The results of these calculations can be found in Table 7.3 and 7.4.

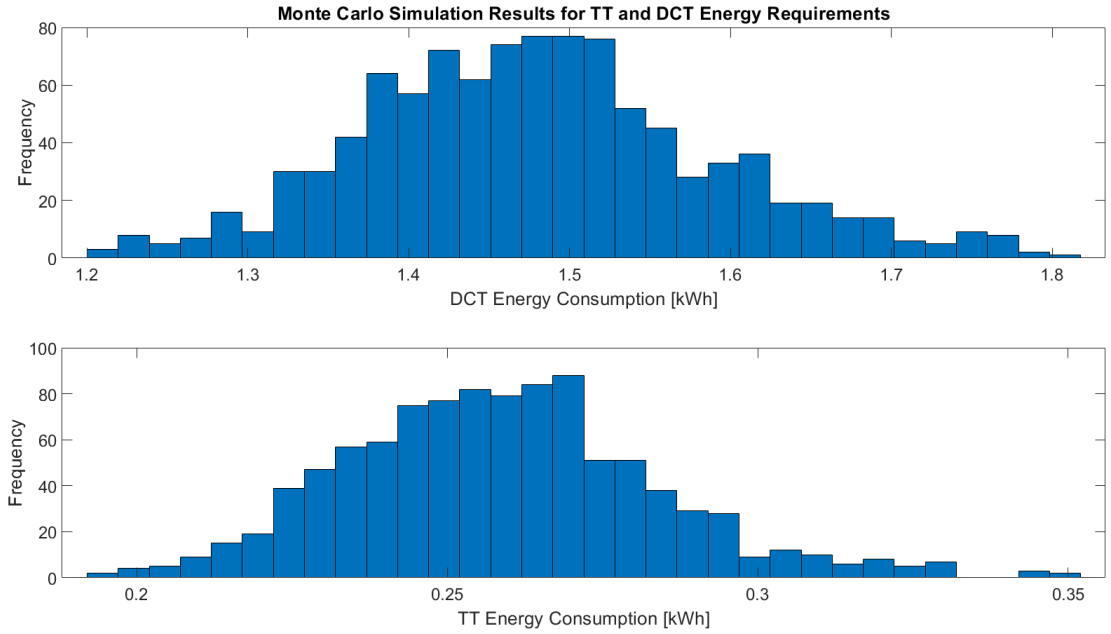

Figure 7.10: Monte Carlo Simulation results for DCT and TT energy requirements using MPC

Table 7.3: Statistics of Energy Requirements MPC

	DCT Energy [kWh]	**TT Energy [kWh]**
Sample Mean $\bar{x_n}$	1.4802	0.2586
Sample Standard Deviation s_n	0.1082	0.0250
$\pm t_{n-1,\alpha.2} \cdot \frac{s_n}{\sqrt{n}}$	0.0067	0.0016
95% Confidence Interval	1.4802 ±0.0067	0.2586 ±0.0016
95% Confidence Interval Range	[1.4735, 1.4869]	[0.2571, 0.2602]

In Table 7.3, the statistics of the 1000 simulations and the corresponding 95% confidence intervals for the sample mean of the DCT and TT energy are shown. Both intervals are relatively small, which is similar as for the confidence intervals using the PID controllers. The standard deviation for both the DCT and TT energy are smaller compared to the results from the PID controllers in Table 7.2. This results in smaller confidence intervals, since the values from the complete set of data are closer to the mean. The reason for the smaller standard deviation for the energy requirements is the cost function from the MPC controller, which tries to minimize the controller effort to track the desired reference signal. Based on the confidence interval for the energy requirements, it can be concluded that MPC is more capable of handling modelling uncertainties while trying to minimize the energy requirements. The corresponding controller performance and the most important KPIs will be covered in the next section.

MPC Controller Performance

In Figure 7.11, the overshoot and undershoot of the MPC controller is plotted. It is clear to see that the data has a normal distribution around zero, meaning that there is overshoot, as well as undershoot. The over- and undershoot is measured with respect to the desired depth of 15 meters, at time step $t = 3725$ seconds. This value is chosen since at this time step, the maximum overshoot was measured for the MPC simulation results which are discussed in Chapter 6 in Section 6.2.2. Therefore, it must be noted that the overshoot and undershoot from Figure 7.11 are not necessarily the maximum values, since the time step at which the maximum (or minimum) overshoot occurs can vary slightly. Some other time steps, around $t = 3725$, are used as well to measure the over-and undershoot, but the results has shown that the over-and undershoot were smaller at those time steps. For the PID controller, this problem does not exist, since there is no undershoot observed. The comparison between PID control and MPC control will be made in Section 7.5.

The calculated confidence intervals for the chosen controller KPIs, which are the overshoot of the depth, and the overshoot of the pitch angle, can be found in Table 7.4. The data and distributions used for these calculations can be found in Figure 7.11 and 7.12.

Table 7.4: Statistics MPC Performance

	Depth Over- and Undershoot [m]	**Pitch Angle Overshoot [deg]**
Sample Mean $\bar{x_n}$	0.0186	0.2715
Sample Standard Deviation s_n	0.2858	0.0070
$\pm t_{n-1,\alpha.2} \cdot \frac{s_n}{\sqrt{n}}$	0.0177	$4.3286 \cdot 10^{-4}$
95% Confidence Interval	0.0186 ±0.0177	0.2715 $\pm 4.3286 \cdot 10^{-4}$
95% Confidence Interval Range	$[9.1695 \cdot 10^{-4}, 0.0364]$	[0.2710, 0.2719]

In Figure 7.11, the over-and undershoot of the desired reference depth of 15 meters is plotted. It can be seen that it has a normal distribution around a mean value of approximately zero, which can also be concluded from Table 7.4. The difference compared to the PID controller is the increased standard deviation, and corresponding larger confidence intervals. This indicates that the optimized solution of the MPC controller, taking into account the cost function and constraints, does not necessarily prioritize reference tracking in case of the depth controller. This results in the large range, taking into account the minimum and maximum values from the sample in Figure 7.11. It must however be noted that the confidence interval of the mean value for the overshoot is still small, as can be seen in Table 6.8. In this interval, the minimum value is approximately zero, indicating that the probability of an undershoot

is small. The maximum value of the confidence interval is much smaller compared to the maximum value for the overshoot when using the PID controllers.

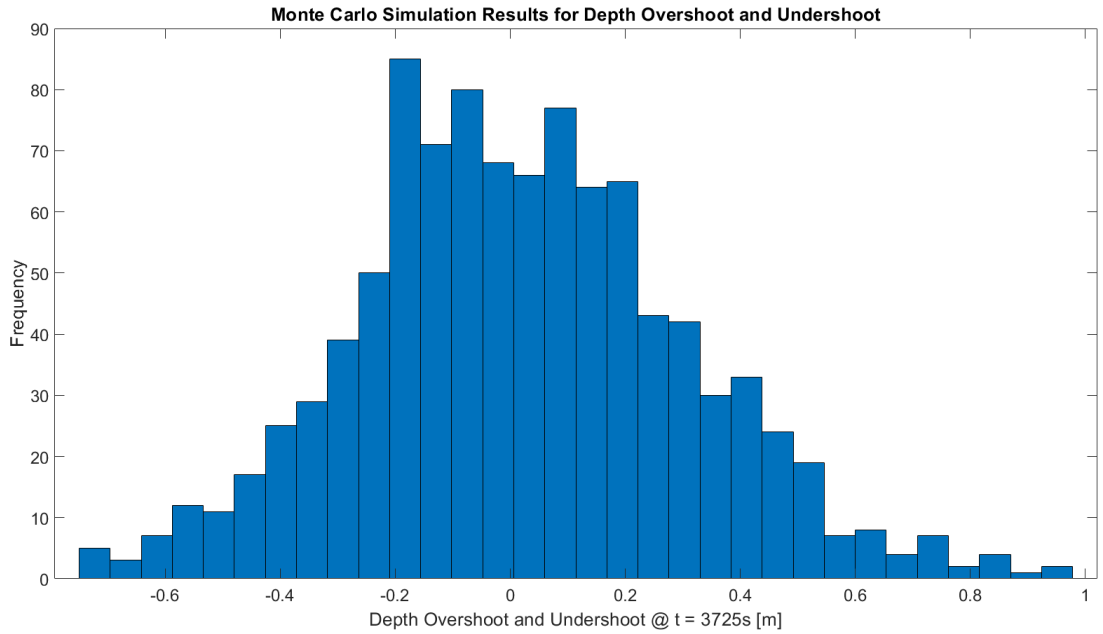

Figure 7.11: Monte Carlo Simulation results for depth overshoot and undershoot @t=3725 seconds using MPC

In Figure 7.12, the overshoot of the desired pitch angle is plotted. It can be seen that the complete range is reasonably small, considering the pitch angle plotted in this figure is given in degrees and the calculated standard deviation in Table 6.8. Comparing the pitch overshoot with the depth overshoot, it can be concluded that MPC prioritizes minimizing the control effort over perfect reference tracking, also when taking into account uncertainties. This conclusion was already drawn for the pitch controller in the previous chapter. As mentioned before, this can be explained by looking at the tuning weights for the change in manipulated variable and the reference tracking from Table 3.11 from Chapter 3. The weight factor for reference tracking for the pitch angle is 10 compared to 1 for the depth reference tracking. With this weight, deviation from the reference signal is penalized. The chosen values for controlling the depth seemed to be sufficient, but using the results of the Monte Carlo Simulation, it can be concluded that the reference tracking when taking into account uncertainties is not completely sufficient with the chosen tuning weights, looking at the relatively large range of values and corresponding standard deviation. However, it must be noted that the values within the confidence interval are still significantly smaller compared to the PID controller. The chosen values for the pitch reference tracking are sufficient, considering the small confidence intervals for the TT energy requirements and overshoot of the desired trim angle.

Therefore, it can be concluded that the MPC controller is performing well for controlling the depth and pitch angle, taking into account modelling uncertainties. For the depth controller, the output reference tracking performance can be more optimized by tuning the weights.

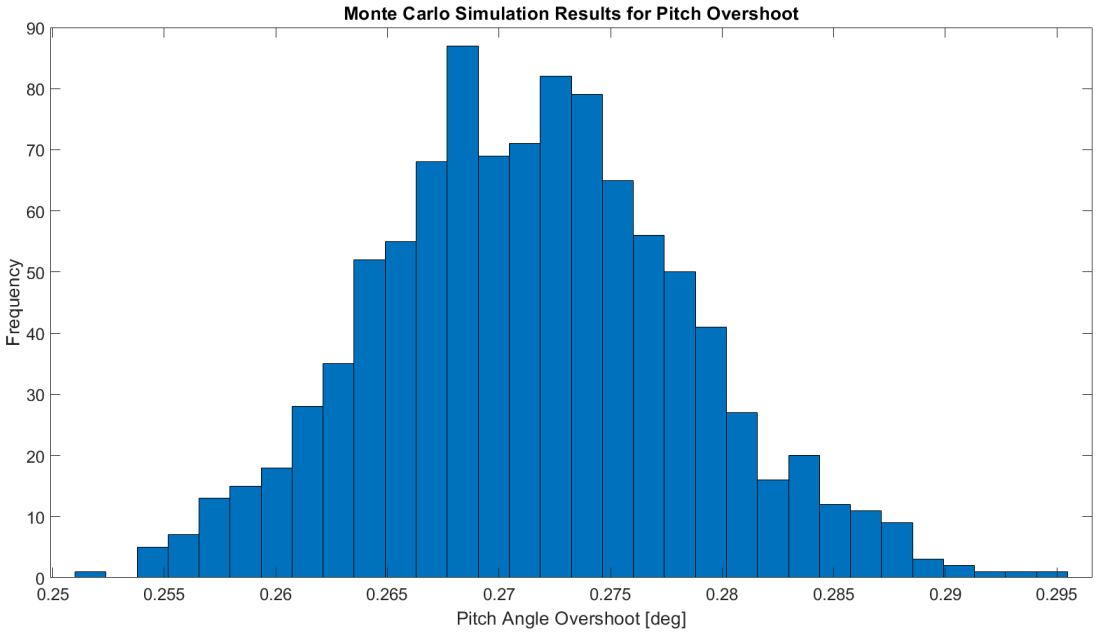

Figure 7.12: Monte Carlo Simulation results for pitch overshoot using MPC

7.5. Conclusion

In Chapter 2, the modelling approach of the ALERD is described. As can be concluded, there are multiple assumptions in this modelling approach, which lead to uncertainty in the calculated value for the used coefficients. Therefore, a sensitivity analysis is done, in order to assess the influence of modelling uncertainties on the outcomes of the simulation model. Monte Carlo simulations are done, for both MPC and the PID controllers, to show the effect of uncertainties on the outcomes, and on the controller performance.

Using the results from the Monte Carlo simulations, 95% confidence intervals for the outcomes of the energy requirements, and for the controller KPIs, are calculated. Important outcomes from the simulation model are the energy requirements for controlling the depth and pitch angle, since they are directly influenced by the performance of the motion controller, and by the six chosen coefficients with the applied uncertainty of 20%.

The confidence intervals for the energy requirements of the depth control tank and trim tanks are small, for both MPC and the PID controllers. Small confidence intervals indicate that the influence of uncertainty is small on the output of the simulation model. From this it can be concluded that, if there is uncertainty around the hydrodynamic coefficients, the final outcomes are not strongly affected. With the constructed confidence intervals, it can be said with 95% confidence, that if simulations are carried out with random coefficients from the distributions, the value of the results will fall within the confidence interval. For both the DCT and TT, MPC has smaller confidence intervals with smaller mean values, from which it can be concluded that MPC with the defined cost-function from Chapter 3 is better in handling uncertainties while minimizing the control effort, and thus the corresponding energy requirements, compared to PID control.

For the controllers, a difference can be distinguished in their performance. The PID controller, used to create a benchmark, is affected by the modelling uncertainties, which results in a higher overshoot in general. A majority of the data points for the overshoot is higher than the mean value of the overshoot. The controller performance therefore decreases, taking into account uncertainties in the modelling approach. As mentioned earlier, for an underwater vehicle such as the ALERD, large overshoots are undesirable. Since the mean value of the overshoot is already 0.78 meters, using the best possible tuned PID controller, it can be concluded that PID control is insufficient for controlling underwater vehicles such as the ALERD.

For the MPC controller, both overshoot and undershoot for the depth reference tracking can be observed, which is distributed around the mean value of 0.0186 meters. Although the standard deviation

is larger compared to the one from the PID controller, the maximum values of confidence interval of the mean value are still considerably smaller.

Due to the chosen tuning weights, reference tracking is not necessarily prioritized by the controller for the depth reference tracking, resulting in a larger standard deviation and confidence interval around the mean value, and the larger maximum values for the over-and undershoot from the data sample. The pitch reference tracking shows robust behavior taking into account the uncertainties, since both the confidence intervals for the energy requirements and for the overshoot are smaller compared with the results from the PID controller.

Overall, it can be concluded that MPC outperforms the PID controllers on most of the KPIs, which corresponds to the conclusions made in Chapter 6.

8

Conclusions, Discussion and Recommendations

In this chapter, the overall conclusion will be given, based on the Chapters from this report. It will be shown that the research aim is achieved, and the research questions from Chapter 1 are answered. Recommendations for future work will be made as well.

8.1. Conclusions

The research, described in this report, is done to achieve the research aim stated below and defined in the introduction in Chapter 1.

"The development of a time-domain simulation model, in which the hydrodynamics of an autonomous submerged dredger are modelled, and which is able to perform trajectory-tracking using a motion controller, while optimizing the required energy consumption for motion control."

The research questions defined in the introduction are used to achieve the research aim. Each chapter in this report answers one of the research questions, and the conclusions will be given here, for each question.

1. *"How can the hydrodynamics of underwater vehicles such as the ALERD be mathematically modelled and implemented in a time-domain simulation model?"*

In Chapter 2, the first research question is answered. Based on the literature review done in preparation of this research, it is chosen to model the ALERD assuming an ellipsoidal hull form, with two planes of symmetry. The hydrodynamic coefficients need to be estimated mathematically, since no data is available from CFD-analysis or scale-model tests. Furthermore, a parametric model of the ALERD makes it possible to change main parameters, such as the length or displacement of the hull, to check different designs. Assuming two symmetry planes significantly reduces the number of coefficients in the equations of motion in 6 DoF. The diagonal terms of the added mass matrix are estimated using Lamb's k-factors, and the diagonal terms of the linear damping matrix are scaled using data from a small AUV. For the equations of motion, the method from Fossen, described in [7] is used. This methodology is seen as the state-of-the art in modelling and control of ships and underwater vehicles, and is widely used in the literature. The ALERD is modelled as an underwater vehicle with equations of motion in 6 DoF, which are solved in Simulink using a state-space representation for a certain time-period.

The modelling approach used makes it possible to control the ALERD in all 6 DoF, using motion controllers during a time-domain simulation. Furthermore, multiple designs can be checked and compared with each other, which is seen as an advantage due to the current concept phase of the ALERD, for which the main dimensions are not yet fixed.

2. *"What is the operational profile of one complete dredging cycle of the ALERD?"*

In Chapter 3, the second research question is answered. The ALERD is a unique underwater vehicle, and therefore a corresponding operational profile is defined and used as control objective for the motion controllers. The operational profile is based on an operational profile analysis using data from conventional dredgers performing coastal replenishment along the Dutch coastline.

It is chosen to create reference signals in three DoF, which are the forward speed u, the depth z, and the pitch angle θ. Controlling the two DoF z and θ contribute to the energy requirements for stability and buoyancy control, and the forward speed u is controlled since the speed is used in the equations of motion.

Two disturbances are defined, which are the trimming moment due to the draghead, and the change of mass in the hopper during dredging and discharging. The signals of the disturbances, in combination with the reference signals for the three DoF, are used as input for the motion controllers.

3. *"Which motion control methods are the best suitable of trajectory-tracking and controlling the different DoFs of the ALERD?"*

Two motion control methods are used in the simulation model and described in Chapter 3, which are PID control and MPC. PID control is used as starting point to create a benchmark, due to its ease of implementation in the simulation model. Each DoF has its own PID controller, which can be tuned by adjusting the PID gains. It can be concluded that the PID controllers are not suitable for controlling a complex system such as the ALERD, taking into account the disturbances and the physical constraints of the actuators. When constraints are applied on the controller, the automatic tuning function for the depth controller shows insufficient performance. Manual tuning is done to improve the controller, leading to a trade-off in controller performance and energy requirements for tracking the reference trajectory.

MPC is used as more advanced control method, and compared to the results of the PID controllers. From the simulation results, it can be concluded that MPC outperforms the PID controllers with tracking the reference trajectory for the depth, while optimizing the control output and taking into account the physical constraints. Optimizing the control output leads to lower energy requirements compared to the PID controllers, for both controlling the depth and pitch angle.

It is shown that for motion control of a complex system, such as an underwater vehicle with time-varying disturbances, MPC shows better performance. MPC optimizes the control output, which is directly coupled with the energy calculations for the actuators used to produce the control forces and moments. The energy requirements can be minimized using MPC, while ensuring the reference trajectory is closely followed. The physical constraints of the systems can be easily implemented, and are used in the cost-function and by the solver to obtain the best solution. Controlling the ALERD with MPC contributes to making it a cost-effective solution for coastal replenishment along the Dutch coastline.

4. *"How can the physical systems, needed for stability and buoyancy control, be implemented in the simulation model and used to calculate the energy requirements?"*

The outputs of the motion controllers are directly coupled with the physical systems that are used to produce the required control forces and moments. In Chapter 4, a description is given of the used physical systems, and their implementation. It is chosen to model a ballast water pump system and a compressed air system, and compare the results. The maximum power and energy consumption are calculated for the complete time-domain simulation. The pump requires the least amount of energy, and is used to control both the depth and pitch angle. Furthermore, the change of weight in the hopper is compensated using a pump system in combination with the main ballast tank.

Using the MPC controller results in an optimal controller output, and since this is directly coupled with the energy calculations, it results in the least amount of energy consumption compared to the results from the PID controllers. For the ALERD this is seen as important, since in the end, the total amount of required energy determines if submerged dredging is advantageous compared to conventional dredging.

5. *"How does uncertainty in the modelling of underwater vehicles such as the ALERD affect the performance of the motion controllers and therefore the outcome of the simulation model?"*

Since the ALERD is mathematically modelled as an underwater vehicle using multiple assumptions, there is uncertainty around the calculated values of the hydrodynamic coefficients, and other used parameters. A sensitivity analysis is done in Chapter 7 using the Monte Carlo simulation, to show the effect of uncertainty around six coefficients on the outcomes of the simulation model, and the controller performance. From the equations of motion 4 coefficients are chosen, which are linear damping coefficients in heave and pitch (Z_w and M_q), the added mass in heave ($Z_{\dot{w}}$), the mass moment of inertia I_{yy}. Furthermore, two coefficients used for the energy calculations are chosen, which are the pump efficiency η_{pump} and the resistance factor ζ. For each coefficient, it is assumed that the uncertainty is 20%.

The results from the Monte Carlo simulations have shown that uncertainty on these six coefficients does not heavily affect the outcomes of the simulation model. 95% confidence intervals are constructed for the energy requirements for the depth control tank (DCT) and trim tank (TT), which are a direct result of the output of the controllers for the depth and pitch angle. MPC shows better performance taking into account modelling uncertainties. The resulting energy requirements from MPC have a smaller confidence interval compared to the results from the PID controller, with a smaller mean value. It can be concluded that applied uncertainties in general result in a higher overshoot for the PID controller, taking into account depth control. Since the mean value of the overshoot for the PID controller is already significant (0.78 meters), it can be concluded that PID control is not suitable for controlling the ALERD. MPC is better in handling uncertainties, while still minimizing the control effort and ensuring good reference tracking for both the depth and pitch angle.

6. *"Using the outcomes of the time-domain simulations, what is the contribution of the energy requirements for stability and buoyancy control to the complete energy consumption for submerged dredging?"*

In Chapter 6, a comparison is made between the total energy requirements per cubic meter of soil for the ALERD and a conventional dredger. The contribution of the energy requirements for buoyancy and stability control is one of the outcomes of this research. The other energy requirements, for instance for propulsion and dredging, are already calculated in previous studies done by C-Job.

It is shown that the contribution of the energy requirements for stability and buoyancy are around 16% of the total amount of required energy. Using the results from this research, it is shown that submerged dredging reduces the required amount of energy with more than 66% for the specific operational profile defined in this research. It is however important to note that the calculations in this research are done using perfect conditions, assuming no environmental disturbances and symmetrical loading and unloading of the hopper.

The overall conclusion is that the research aim, defined in the introduction in Chapter 1, is achieved. The end product of this research is a time-domain simulation model, built in Simulink, in which the ALERD is modelled using equations of motion in 6 DoF. The modelling approach enables the user of the model to change important input parameters, such as the main dimensions or pump characteristics, in order to compare different designs. It is shown that MPC is the best control strategy for the ALERD, and that MPC ensure close reference tracking while optimizing the control effort. The output of the controllers is used to calculate the energy consumption and required power, and minimizing the control effort minimizes the required power and energy consumption. The simulation model is built in such a way that the remaining DoF sway, roll and yaw, can be added to the controller, to obtain a complete 6 DoF controlled simulation model. It is shown that uncertainty in the calculated input parameters does not heavily affect the outcomes of the simulation model, especially when using MPC. It is shown that in perfect conditions, the contribution of the energy requirements for stability and buoyancy control to the total amount of consumed energy is 16% for the specific operational profile defined in this research. This value shows the potential of submerged dredging and the need for future research on this topic.

8.2. Discussion and Recommendations

In this section, a discussion on the simulation model and the results is given. Furthermore, to improve the simulation model, and to get more accurate and realistic results, recommendations for future work are made.

Hydrodynamic Coefficients
To get more accurate results and outcomes of the simulation model, the off-diagonal hydrodynamic coefficients must be known for a realistic hull form. If these coefficients are known and used, all the motions in 6 DoF are coupled, which makes the simulations more realistic. If the motions are coupled, diving maneuvers can be simulated, which is the coupled motion between heave and pitch. For diving maneuvers, stern planes can be used instead of ballast water tanks, which possibly leads to reducing the energy requirements.

Environmental Disturbances
Environmental disturbances can be added to the model, in order to get more accurate and realistic results. As mentioned in the literature review, many disturbances from the environment can disturb the operations of underwater vehicles, such as surface waves, currents, near-bottom and near-surface effects, and changes in the salinity level of the seawater. Those disturbances will also affect the energy requirements for stability and buoyancy control, and are therefore important to take into account.

Furthermore, at greater depths, hull compression can play a role for the ALERD as well, disturbing the balance between the weight and buoyancy. All the above-mentioned effects are affecting the energy requirements, which are expected to increase taking into account these disturbances.

Free Surface Effect in the Hopper
In this research, perfect conditions for loading and unloading the hopper are assumed. Often, the dredged soil is not perfectly symmetrical distributed in the hopper, which can lead to additional trimming and also rolling moments. By disregarding the perfect loading assumption, there is the need to control the possible generated rolling moments, as well as the trimming moments, and heave forces generated due to the loading and unloading of the hopper. Controlling the rolling moments leads to an additional DoF that must be taken into account using motion controllers.

Furthermore, the dredged soil, which is a mixture of sand and water, can have a free surface effect, leading to possible stability issues, requiring additional active measures. By adding more realistic scenarios, the outcome of the energy requirement for stability and buoyancy control will become more realistic as well.

Main Ballast Tank and Hopper Dynamics
In the present research, it is assumed that there is a perfect matching between the main ballast tank (MBT) and the hopper, in terms of mass flow rate, meaning that the hopper is filled with the same rate and at the same time, as the MBT is being emptied with, and vice versa. This assumption leads to the fact that no additional heave forces are created, since the total mass of the MBT and the hopper are always constant.

This assumption is not valid in reality, taking into account the dynamics of the dredged soil in the pump and the pipe-flow system, and the large capacity of the hopper. The increase in weight of the hopper during dredging is approximately 25% of the total displacement, which can be considered very high for underwater vehicles. In reality, it is expected that during the dredging and discharging operations, the mass of the main ballast tank and the hopper are not perfectly balanced, leading to a weight difference of the ALERD. This weight difference must be actively compensated, if the depth and pitch angle are controlled to ensure a sufficient hull-bottom clearance, during the dredging and discharging operations.

By taking into account the physical processes of the pumps, the dynamics of both the seawater and the dredged material in the hopper, the simulations can be made more realistic and therefore more accurate.

Depth Control- and Trim Tank System
The depth control tank and trim tank system are used in combination with the motion controllers to provide the control forces and moments, required for achieving the control objectives. In the simulation model, it is assumed that the required mass, and thus the required mass flow rate, can be delivered instantaneously, without taking into account the dynamics of the seawater in the pumps and pipe-flow system, and the characteristics of the physical systems needed to drive the ballast pumps, such as the electric motors.

For the trim tank system, the required additional mass in either the forward or aft trim tank can be delivered instantaneously, only taking into account the constrained mass flow rate. In reality, it takes a

certain amount of time for the ballast water to travel 60 meters, from the forward tank to the aft tank, or vice versa. Similar as for the MBT and the hopper, the fluid dynamics and the characteristics of the physical systems used to drive the pumps can be added in order to make the simulations more realistic.

Results and Comparison with a Conventional Dredger
In this research, a comparison is made between the ALERD and a conventional dredger. It is concluded that, using the defined operational profile for both the ALERD and the conventional dredger, the ALERD is more energy efficient, reducing the total energy consumption with more than 66%.

However, this conclusion can be made only for this specific operational profile. To get insight in the potential advantages of submerged dredging, different operational profiles can be implemented in the simulation model, to show what the energy requirements are. For instance, the required power for the pumps is dependent on the depth of the ALERD, since there is atmospheric pressure inside the tanks. The required power for the pumps is therefore increasing with the depth. To make a complete comparison and conclusion, more simulations with different operational profiles can be carried out.

Model Validation
The simulation model must be validated using either results from scale-model tests or CFD-analysis to compare the outcomes. Furthermore, the simulation model itself can be validated using input data and output results from experiments carried out with underwater vehicles, available in the literature. Validating the simulation model with existing data can show whether the outcomes are accurate and realistic. Taking into account the uncertainties in the hydrodynamic coefficients used to model the ALERD, it is already shown with the sensitivity analysis that they do not heavily affect the outcomes of the simulation model.

A

General Arrangement and Dimensions Conventional Hopper

Confidential.

Bibliography

[1] *Aandeel Beschermde Natuurgebieden in Nederland*. URL: https://www.clo.nl/indicatoren/nl1425-begrenzing-van-het-natuurnetwerk-en-natura-2000-gebieden.

[2] Charlie Bellekom. *Operational Stability of the Autonomous Underwater Maintenance Dredger*. 2020.

[3] *Choose a Control Design Approach*. URL: https://nl.mathworks.com/help/slcontrol/ug/choosing-a-compensator-design-approach.html.

[4] *Cost Function and Optimization Problem*. URL: https://nl.mathworks.com/help/mpc/ug/optimization-problem.html.

[5] Frederik Michel Dekking et al. *A Modern Introduction to Probability and Statistics*. Springer, 2005.

[6] T.I. Fossen and T Perez. *Marine Systems Simulator (MSS)*. 2004. URL: https://github.com/cybergalactic/MSS.

[7] Thor I. Fossen. *Handbook of marine craft hydrodynamics and motion control*. Wiley, 2011, p. 596. ISBN: 9781119991496.

[8] S Van Der Harst and R Hijdra. *Autonomous Underwater Maintenance Dredger*. 2018.

[9] Stein Haugen et al. *Safety and reliability : safe societies in a changing world : proceedings of the 28th international European Safety and Reliability Conference (ESREL 2018), Trondheim, Norway, 17-21 June 2018*. 2018. ISBN: 9780815386827.

[10] R Hijdra. *AUTONOMOUS LOW ENERGY REPLENISHMENT DREDGER (ALERD) Eindrapport Verkenningsfase*. 2021.

[11] R Hijdra. *AUTONOMOUS LOW ENERGY REPLENISHMENT DREDGER (ALERD) Operationeel Profiel Analyse*. 2021.

[12] Gustav Holm. *Optimal Control Model for an Autonomous Underwater Vehicle*. 2020.

[13] F. H. Imlay. *The Complete Expressions for Added Mass of a Rigid Body Moving in an Ideal Fluid*. 1961.

[14] *Innovaties in De Kustlijnzorg*. Oct. 2021. URL: https://www.rijkswaterstaat.nl/zakelijk/innovatie/waterinnovaties/innovaties-in-de-kustlijnzorg#nieuws.

[15] Arie De Jager and Klaas Kooiker. *TRAILING SUCTION HOPPER DREDGER (84.95M); SPEED POWER PREDICTION AND CALCULATION OF RESISTANCE OF TWO SUCTION TUBES IN TRAILING MODE*. 2018.

[16] Nassim Khaled and Bibin Pattel. *Practical Design and Application of Model Predictive Control MPC for MATLAB ® and Simulink ® Users*. 2018.

[17] N Kroonenberg. *Choosing a sustainable, economical energy supply system, considering all operational variables of an autonomous submarine dredger*. 2021.

[18] Jonathan Lesage and Raul G Longoria. *Modeling and Synthesis Methods for Retrofit Design of Submarine Actuation Systems. Energy Storage for Electric Actuators*. 2011. URL: https://www.researchgate.net/publication/258511539.

[19] Chengqi Long et al. "Trajectory tracking control of ROVs considering external disturbances and measurement noises using ESKF-based MPC". In: *Ocean Engineering* 241 (Dec. 2021), p. 109991. ISSN: 00298018. DOI: 10.1016/j.oceaneng.2021.109991. URL: https://linkinghub.elsevier.com/retrieve/pii/S0029801821013317.

[20] Steven C. Mallam, Salman Nazir, and Amit Sharma. "The human element in future Maritime Operations–perceived impact of autonomous shipping". In: *Ergonomics* 63 (3 Mar. 2020), pp. 334–345. ISSN: 13665847. DOI: 10.1080/00140139.2019.1659995.

[21] Mohammad Moonesun et al. *Evaluation of submarine model test in towing tank and comparison with CFD and experimental formulas for fully submerged resistance*. 2013, pp. 1049–1056.

[22] Mohammad Moonesun et al. “Practical scaling method for underwater hydrodynamic model test of submarine”. In: *Journal of the Korean Society of Marine Engineering* 38 (10 Dec. 2014), pp. 1217–1224. ISSN: 2234-7925. DOI: 10.5916/jkosme.2014.38.10.1217.

[23] Martin Renilson. *SPRINGER BRIEFS IN APPLIED SCIENCES AND TECHNOLOGY Submarine Hydrodynamics*. 2015. URL: http://www.springer.com/series/8884.

[24] Max Schwenzer et al. *Review on model predictive control: an engineering perspective*. Nov. 2021. DOI: 10.1007/s00170-021-07682-3.

[25] V Sencila and G Kalvaitiene. *Industry 4.0: Autonomous Shipping and New Challenges for Maritime Education and Training*. 2019. URL: https://www.researchgate.net/publication/340965814.

[26] *Standard deviation*. June 2022. URL: https://en.wikipedia.org/wiki/Standard_deviation.

[27] Kantapon Tanakitkorn et al. “Depth control for an over-actuated, hover-capable autonomous underwater vehicle with experimental verification”. In: *Mechatronics* 41 (Feb. 2017), pp. 67–81. ISSN: 09574158. DOI: 10.1016/j.mechatronics.2016.11.006.

[28] Y. Valeriano-Medina et al. “Dynamic model for an autonomous underwater vehicle based on experimental data”. In: *Mathematical and Computer Modelling of Dynamical Systems* 19 (2 Apr. 2013), pp. 175–200. ISSN: 13873954. DOI: 10.1080/13873954.2012.717226.

[29] *Vooroeversuppleties Door Boskalis en Rijkswaterstaat bij Texel Gaan laatste fase in*. Sept. 2021. URL: https://www.schuttevaer.nl/nieuws/offshore/2021/09/08/vooroeversuppleties-bij-texel-gaan-laatste-fase-in/?gdpr=accept.

[30] Jiri de Vos, Robert G. Hekkenberg, and Osiris A. Valdez Banda. “The Impact of Autonomous Ships on Safety at Sea – A Statistical Analysis”. In: *Reliability Engineering and System Safety* 210 (June 2021). ISSN: 09518320. DOI: 10.1016/j.ress.2021.107558.

[31] Liuping Wang. *Model Predictive Control System and Implementation Using MATLAB*. 2009.

[32] Hans Klein Woud and Douwe Stapersma. *Design of Auxiliary Systems, Shafting and Flexible Mounting*. 2016.

[33] Zheping Yan et al. “Model predictive control of autonomous underwater vehicles for trajectory tracking with external disturbances”. In: *Ocean Engineering* 217 (Dec. 2020). ISSN: 00298018. DOI: 10.1016/j.oceaneng.2020.107884.